Plasmon-Enhanced Fluorescent Protein Emission: A New Paradigm for Improved Single-Molecule Bio-Imaging

By
Jessica Erin Donehue

A dissertation submitted in partial fulfillment
of the requirements for the degree of
Doctor of Philosophy
(Chemistry)
in the University of Michigan
2014

Doctoral Committee:

Assistant Professor Julie S. Biteen, Chair
Professor Raoul Kopelman
Associate Professor Stephen Maldonado
Associate Professor Jennifer P. Ogilvie

Dedication

For my family,

who always believed in me.

Acknowledgements

It was a strange decision for me to attend the University of Michigan for graduate school. I was a graduating from THE Ohio State University, bled Scarlet and Grey, and was so damn proud to be a Buckeye it hurt a little bit. But, for some reason, my gut (and my older brother) told me "Michigan is the place to be!" and so, I went.

It was a difficult transition to Michigan; I was cold from October to March that first year and grad school was far more difficult than I had ever expected. But looking back now, I know I made the right decision to disappoint my fellow Buckeyes and make the move "Up North". While at Michigan, I have had the opportunity to work with many amazing and brilliant people, and I have several of them to thank.

I would like to start by thanking my advisor Julie Biteen. Thank you for your mentoring and guidance over the past three years. Thank you for allowing me to join a lab that provided an environment where it was safe to learn and share ideas, and that allowed me to rebuild my confidence after a bumpy start to graduate school. Thank you for your kindness, for your patience, and for your pushing. I am truly honored to have been part of your lab and to be a Biteen Lab Alum.

Thank you to my committee members, Jennifer Ogilvie, Stephen Maldonado, Raoul Kopelman, and Julie Biteen. I am so grateful to have had such a supportive and brilliant dissertation committee. Thank you for listening to my ideas and for offering your wisdom and scientific insight. With your guidance, I have grown to be the scientist I am today.

I am forever indebted to my Biteen labmates and would like to thank them all for their help and support. I am so grateful for the many late evenings spent in 2306 laughing (and of course diligently working), and I want to thank all of you for being an incredibly fun group of people to work with. Thank you, Esther Wertz, for your guidance and collaboration over the past three years. I am a better scientist today because you pushed me, and it was fun to laugh with you along the way. Thank you, Beth Haas, for teaching

me the ways of *Vibrio*, for the hours (and hours) of Matlab help, and for being a great friend and source of support throughout grad school. Thank you, Hannah Tuson, for answering all of my bio questions, for your friendship, and for helping find joy in running. Thank you, Bing Fu, for being the best mentee a graduate student could get, for being a great desk buddy, and always getting my "Friends" references. Thank you, Yi Liao and David Rowland, for the countless hours of Matlab help (I would have far less analyzed data without you both) and for being officemates who always made the work day more enjoyable. Thank you, Ben Isaacoff, for the many figures and for science discussions that pushed me think. Thank you, Chanrith Siv, for being you and bringing joy to the office. Thank you, Mou-Chi Cheng, for being a constant source of knowledge and being able to get me nearly any odd reagent or instrument I needed to get a project done. Thank you, Courtney Talicska, for being a fantastic undergraduate who genuinely loved chemistry. Thank you, Justin Lenhart, Yilai Li, Krishanthi Karunatilaka, and the rest of the Biteen rotating crew, for being part of my graduate experience and for all the fun along the way.

Thank you to the Department of Chemistry at the University of Michigan for providing such a wonderful program where I could learn and develop as a scientist. Thank you to all the fantastic scientists and engineers at the Lurie Nanofabrication Facility who were always so helpful, patient, and kind. Thank you to the entire Maldonado Lab for putting up with me tromping through your lab space for the last three years and teaching me many tricks for preparing substrates.

Thank you to the Department of Chemistry at The Ohio State University and the absolutely extraordinary people I met there. Thank you, Terry Gustafson, for being the first person to introduce me to this idea of chemistry "research", and with that, changing my life forever. Thank you, Ted Clark and Chris Callam, for letting me explore the world of research in your labs and for showing me what it meant to passionately pursue a field you love. Thank you, Nicole (Dickson) Karn, for being my first science role model; your brilliance, mentorship, and friendship made me want to be just like you and led me to where I am today. Thank you, Jennifer Scherer, for being my first chemistry friend and

for loving office supplies as much as me. I couldn't have made it through grad school without your constant support and love.

Thank you to the friends I have made here in Ann Arbor who made the crazy life of grad school a little more colorful and far more fun. In particular, thank you, Sabrina Peczonczyk and Laura Thoma, for not bailing on our first night out and for sticking beside me all these years.

Thank you to my family for being the best cheerleaders a girl could ask for. Thank you for telling me I could do this when I was quite certain I could not. Thank you for patiently understanding why I missed so many birthday parties and cookouts, and for learning to use FaceTime so I could feel like I was there. Thank for all your love and support and for inspiring me to chase my dreams. I love you all more than I could ever express in words.

Finally, thank you to my amazing husband, Dan Flynn, for all of your love and support. Thank you for being a friend to laugh with when I needed a break, thank you for being a shoulder to cry on when I hated it all, and thank you for being a brilliant mind to turn to when I needed help. I am so very happy the world is weird and that we both ended up here in Ann Arbor, and I am so excited for all our future adventures together. I love you.

Table of Contents

List of Figures

List of Tables

Abstract

Single-molecule fluorescence (SMF) microscopy is a powerful technique that provides high sensitivity and nanometer-scale resolution for biological imaging. The emission profile of an isolated fluorescent molecule allows the emitter position to be determined on a scale far smaller than the standard diffraction limit of light with a precision that improves with the number of detected photons. While *in vitro* implementations of SMF have achieved 1.5-nm localization precisions, an outstanding problem in the field is to improve the resolution of SMF imaging in live cells; this has been generally limited to 10 – 40 nm. This limitation reduces the amount of information we can learn about subcellular molecular motions through direct, biophysical methods. The main problem is technological: fluorescent proteins (FPs), the genetically encodable labels widely used for biological imaging, are dimmer and shorter lived than the organic dyes employed *in vitro*. Increasing FP brightness and photostability will significantly improve the precision with which these fluorescent probes are localized *in vivo* down to a few nanometers, as well as increase average trajectory length for single-particle tracking, and these advances will enable studies of intracellular processes on the molecular scale.

In this Thesis, we use SMF microscopy to characterize fluorescence and attain super-resolution images, and we demonstrate that nanoparticle plasmonics can improve both the brightness and photostability of FPs. The localized surface plasmon mode, or collective oscillation of free electrons, produces a highly enhanced field in the near field of a metal nanostructure. Here, by positioning FPs in the near field of gold nanorods via adsorption

or immobilization, we use this coupling to more than double the emission rate of the red FP mCherry, and determine that coupled molecules of the photo-activatable FP PAmCherry emit three times more photons prior to photobleaching. This is the first reported demonstration of plasmon-enhanced fluorescence brightness and stability in intrinsically fluorescent proteins. We then extend our methods to *in vivo* experiments, in which gold nanotriangle arrays serve as extracellular imaging substrates to enhance the emission from membrane-bound proteins in live bacterial cells. We detect a plasmon-enhanced emission rate from FP-labeled proteins in the membrane of single cells of *Vibrio cholerae*, agent of the human cholera disease, and show that these nontoxic plasmonic substrates have promise for directly increasing the power of live-cell SMF. Finally, we demonstrate selective excitation of the longitudinal mode of gold nanorods using polarization, and consequently tune the amount of plasmon-enhanced emission observed. This achievement increases our control over enhanced fluorescent emission.

The work in this Thesis demonstrates the power of plasmon-enhanced single-molecule fluorescence to strongly impact the bio-imaging field, with implications for human health and disease. Ultimately, increased brightness and photostability will allow faster imaging speeds, improved localization precisions, and increased trajectory lengths for *in vivo* imaging. Furthermore, the preferential excitation of certain plasmon modes will enable nanoscale selectivity in living systems. By exploring plasmon-enhanced FP emission, applying this understanding to *in vivo* systems, and demonstrating increased selectivity for addressing nanostructures on the nanometer scale, we have developed a new paradigm for improving super-resolution microscopy in living cells.

Chapter 1 Introduction

1.1 Pushing the Scale of Discovery

Our eyes are very sensitive detectors for observing macroscopic systems, but for the microscopic, and even the nanoscopic, we turn to the tools of the trade to peer into a fantastic molecular world. Microscopes have been used for centuries, and in the 1600s, Anton von Leeuwenhoek was the first to use a single-lens microscope to view large bacterium,[1] making visible the previously unseen, and opening up a new scale of discovery. Today, the inverted fluorescence microscope is the preferred tool for observing microscopic biological systems as it allows the observer to view the bottom of a sample, like cells in a petri dish, in a relatively stable and non-invasive manner. New microscopy techniques have recently pushed the scale of discovery from micrometers (10^{-6} meters) to the nanometers (10^{-9} meters),[2,3] but ultimately the scientific process strives to push the limits of possibility and improve the current state of the art.

This Thesis describes the development of plasmon-enhanced fluorescence for applications in single-molecule nanoscopy in order to optically image live bacteria cells with spatial resolution significantly better than half the wavelength of imaging light. With this technique, we have extended the imaging capabilities of single-molecule fluorescence techniques by increasing emission from fluorescent proteins, as well as improving sensitivity for single fluorescent proteins detection in live bacteria cells. Furthermore, we have used polarization techniques to better understand the coupling of

single fluorescent molecules and plasmonic nanoparticles, with the goal of expanding the utility of plasmonic substrates for application in live-cell biological imaging.

1.2 Fluorescence microscopy

Fluorescence microscopy is a preferred method of observation for biologists because it uses visible light to non-invasively image cellular systems with minimal perturbation to the sample, and because the fluorescence microscope allows the observer to watch dynamics inside living systems on biologically relevant timescales (Figure 1-1). A problem arises, however, when the goal is to image subcellular structures, like proteins inside cells. The resolution of a fluorescence microscope is fundamentally limited by the diffraction of light, therefore, causing even an isolated, infinitesimally small emitter to appear as a finite-sized spot.[4] The three-dimensional intensity distribution of this spot is called the point spread function (PSF) of the microscope. If two point source emitters are closer than the PSF full width at half-maximum (FWHM), these emission patterns, which are a two-dimensional projection of the three-dimensional PSF, cannot be individually resolved by the microscope.[5] The FWHM of the PSF in the lateral (*x*-*y*) direction is approximately $\Delta x \sim \frac{0.61\lambda}{NA}$, where λ is the wavelength of light and NA is the numerical aperture of the objective, which is a measure of the microscope collection power and is defined as $\mathrm{NA} = n \sin \alpha$.[2] In this equation, n is the refractive index of the medium and α is the half-cone angle of light focused by the objective. The axial (*z*) width of the PSF is 2-3 times as large as the lateral width for most high-NA objectives. For a typical fluorescence microscope equipped with a high-NA oil-immersion objective (NA = 1.4), like the objectives used in this thesis, imaging with visible light (λ ~ 500 nm) would result in a PSF with a lateral size of ~200 nm and an axial size of ~500 nm.[2] The scale of

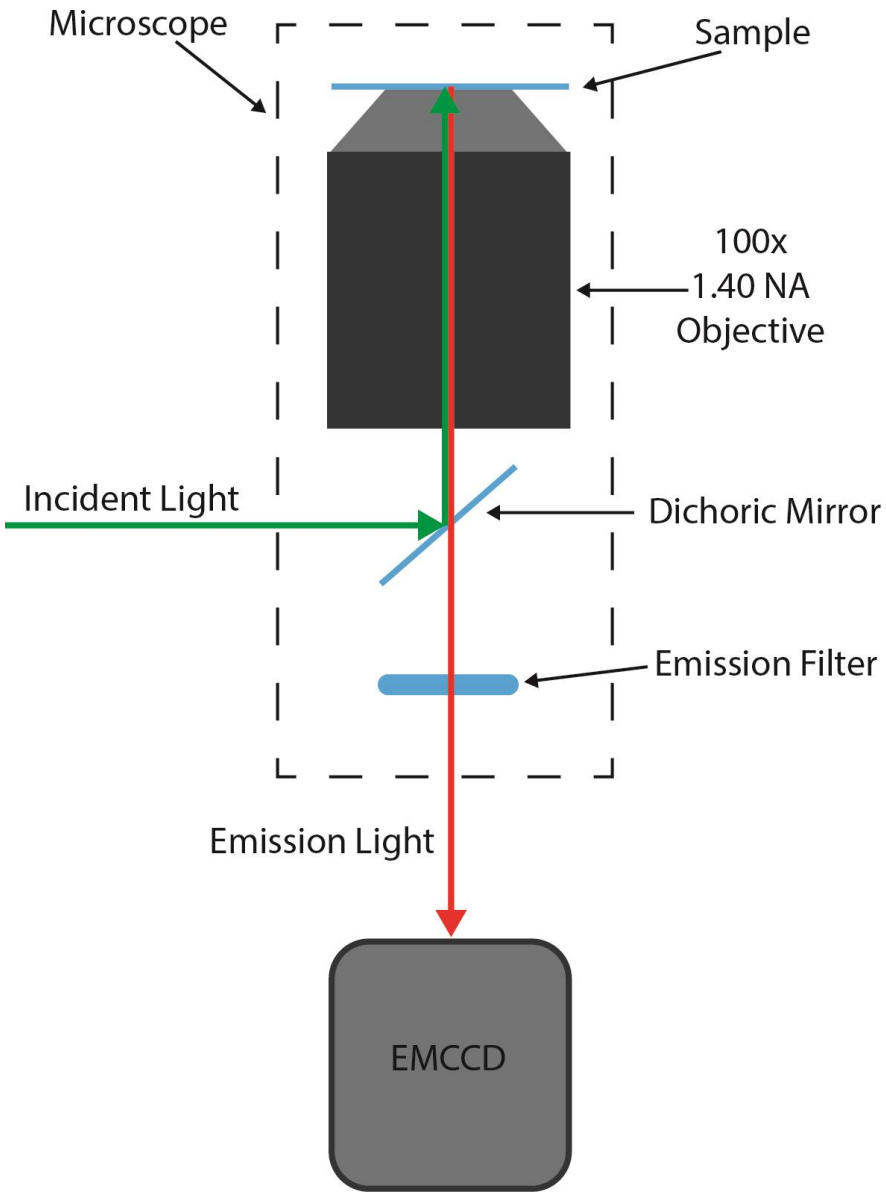

Figure 1-1. Schematic of epi-fluorescence inverted microscope showing excitation and emission pathways, as well as sample placement.

a visible light PSF can therefore be used to image larger biological structures, like whole bacteria cells or red blood cells, but most subcellular components, like proteins or DNA, cannot be resolved.[6] Other microscopy techniques, such as electron microscopy, routinely achieve nanometer-scale resolution and provide the structural details blurred in light microscopy by diffraction, but their high-energy excitation source (an electron beam) can be destructive, and their vacuum chamber operation requires that biological specimens be frozen or fixed. Ultimately, this sample preparation freezes all dynamics and thus limits the amount of useful biological information gained. Additionally, labeling schemes for electron microscopy are often limited and identifying specific proteins is often difficult.[7] Figure 1-2 shows a comparison of the size scales of various cellular structures and microscopy technique corresponding to those ranges.[6]

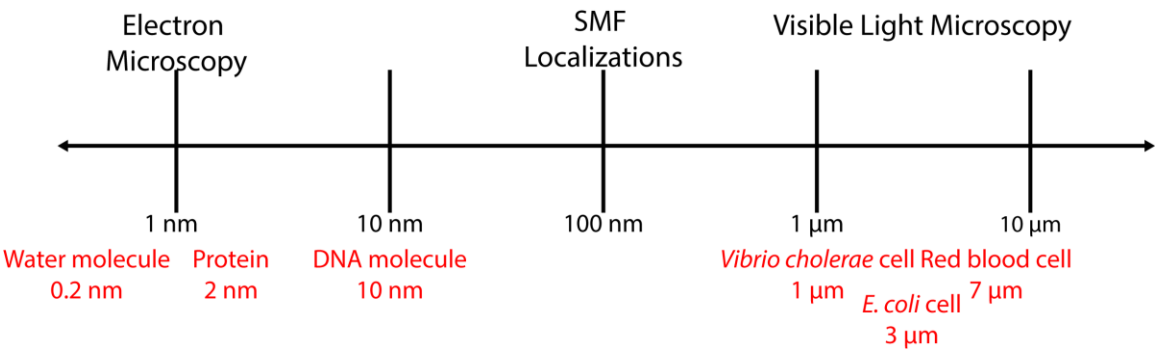

Figure 1-2. Comparison of size scales for various cellular structures and microscopy techniques.

1.3 Single-molecule fluorescence and super-resolution microscopy

Fluorescence microscopy remains an important tool for studying living biological systems, as it is non-invasive, minimally perturbative, compatible with live cells, relatively inexpensive, and takes advantage of a wide-range of available labels. For these reasons, over the last three decades, much work has been dedicated to improving the resolution of this imaging method.[2,3,7-9] Single-molecule fluorescence (SMF) microscopy is one technique that can improve the achievable resolution of a standard fluorescence microscope. With this technique, individual fluorescent molecules are imaged one by one and used as reporters of their unique molecular environment, with no need for ensemble averaging. When applied to biology, SMF provides nanometer-scale resolution that can reveal the secret internal workings of a living cell in its natural environment. This super-resolution technique breaks the standard diffraction limit by fitting the detected PSF of each isolated fluorophore to identify the fluorophore position with a localization precision that can be far better than the standard diffraction limit of light.[10] Generally, a molecule of interest is labeled with a fluorescent tag that serves as an isolated point source. The emission profile of this essentially infinitesimal tag approximates the microscope PSF and can be fit with a model function, most often a two-dimensional Gaussian function; the PSF center position indicates the precise location of the isolated emitter (Figure 1-3). The emitter fluorescence is then collected using an electron multiplying charge-coupled device (EMCCD).

The emitter localization precision (Δx) is determined by several factors, including the size of the detector pixels (a), the background noise per pixel (b), the standard deviation of the

model PSF (s), and the number of photons detected (N), as described by Thompson et al.[4]:

$$\Delta x = \sqrt{\frac{s^2 + \frac{a^2}{12}}{N} + \frac{8\pi s^4 b^2}{a^2 N^2}}$$

In the limit of low background noise, the localization precision of for a given pixel size and PSF is:

$$\Delta x \propto \frac{1}{\sqrt{N}}$$

Therefore, only the number of detected photons limits the precision of this technique, and *in vitro* implementations of SMF by Yildiz *et al.* have achieved 1.5-nm localization precisions.[11,12]

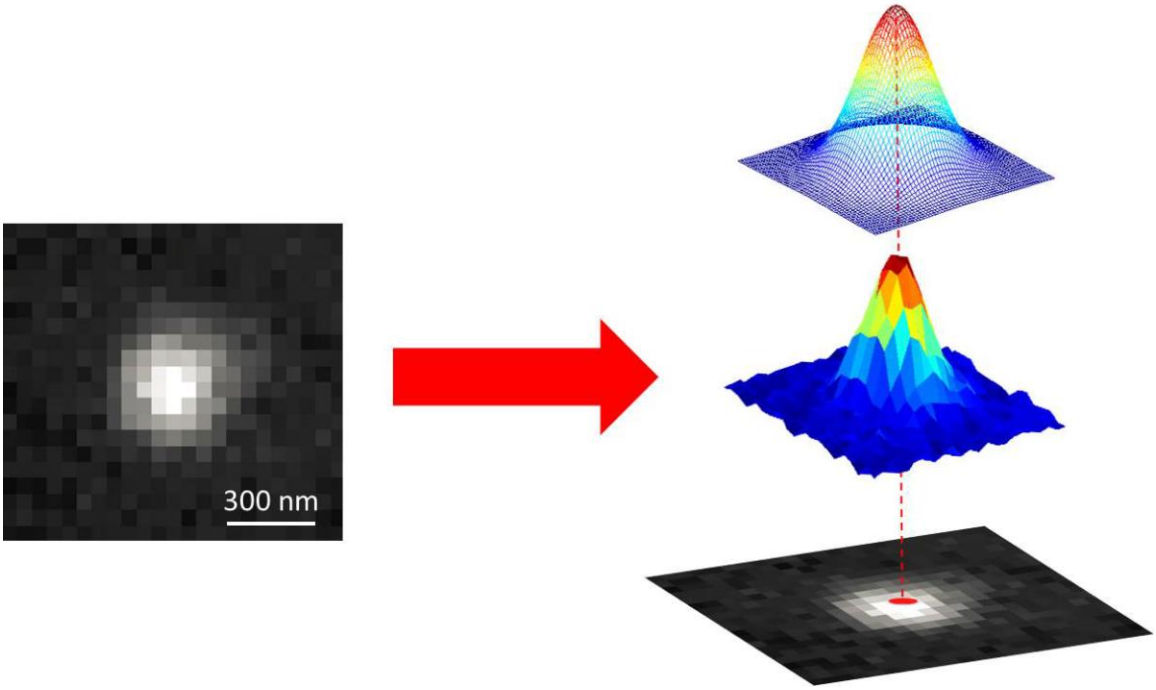

Figure 1-3. Left: The diffraction-limited image of an isolated emitter. Right: The intensity profile of the isolated emitter is fit to a 2D Gaussian function to precisely localize the center of the emission pattern. Figure by Yi Liao.

1.4 Single-molecule probes

The discovery of the green fluorescent protein (GFP)[13] in 1962 and the ability to tune its variants across the visible spectrum[14-16] dramatically expanded the field of bioimaging and has made an incredible impact on what can be observed inside living systems. The ease with which FPs can be genetically encoded and covalently bound to a protein of interest, with high labeling specificity and without need for trans-membrane introduction of any cofactors besides oxygen, makes them a primary choice for *in vivo* fluorescent tags.[17] Though FPs are routinely used in single-molecule imaging,[18-21] FPs are far from perfect single-molecule probes. In particular, FPs have limited brightness and poor photostability when compared to their organic dye counterparts.[22,23] The brightness and photostability of a fluorophore are ultimately functions of the radiative decay rate of that molecule, and so this rate must be considered when evaluating the utility of a fluorophore as a SM probe. For example, Rhodamine 6G, a common small organic molecule, has a radiative decay rate of 0.22 ns^{-1} and is often used for single molecule studies,[23] while mCherry, a typical red FP, is less bright, with a 0.15 ns^{-1} radiative decay rate.[22] Deficiencies in FP radiative decay rates ultimately influence the quantum yield (QY) and photostability of these fluorescent probes. Again, Rhodamine 6G makes a superior SM probe with a QY of 95%,[14] while mCherry has a QY of a mere 22%.[22] In terms of photostability, Rhodamine 6G will typically emit 10^6 photons prior to photobleaching[23] (the photochemical destruction of a fluorophore causing it to no longer emit light), while GFP, another common FP tag, will typically emit only 10^5 photons prior to photobleaching,[24] making it a substantially less stable fluorophore.

As discussed in Section 1.3, the spatial precision of single-molecule localization depends on the total number of photons detected.[10] Poor FP radiative decay rates (and ultimately low quantum yields and photostabilities), therefore, contribute significantly to the fact that the resolution of SMF microscopy is currently limited to 10-40 nm in live cells.[25,26] Due to the many benefits of FPs as *in vivo* imaging tags, though, much interest lies in increasing the emission and photostability of FPs to ultimately increase the number of photons detected from these probes and improve SMF imaging in live cells.

1.5 Fluorescence

Single molecules are detected in SMF imaging experiments when the molecule emits a photon. Each detected photon is the result of the radiative decay of an excited-state electron that was promoted by photon absorption. Molecular absorption (*A*) is governed by Beer's Law, $\mathrm{A} = -\log \mathrm{T} = \log\left(\frac{\mathrm{P}_o}{\mathrm{P}}\right) = \varepsilon bc$ where *T* is transmission, P_o is the incident radiant power, *P* is transmitted radiant power, ε is the molar extinction coefficient, *b* is the path length, and *c* is the absorber concentration. Though UV-vis absorption spectroscopy can be used quantitatively, its sensitivity is generally three orders of magnitude less than that of fluorescence spectroscopy,[27] making fluorescence more suitable for single-molecule techniques. Once absorption has taken place, a molecule can relax back to the ground state by either radiative (fluorescence or phosphorescence) or non-radiative (internal conversion, intersystem crossing, etc.) transitions, as illustrated in in Figure 1-4. In this figure, bold lines represent the lowest vibrational state of the ground electronic state (S_0), as well as of the first (S_1) singlet excited state. Higher lying vibronic states are represented as thin lines above each electronic state. Generally, a molecule will be excited both electronically and vibronically after photon absorption (*A*; green arrow).

The most likely process to initially take place after absorption is vibrational relaxation (*VR*; gray curved arrow). This process is very fast (~10^{-11}-10^{-9} s) and is caused by a loss of vibrational energy due to collisions with other molecules, as well as sample heating. Next, a molecule can relax electronically through internal conversion (*IC*; black dashed arrows), a non-radiative transition in which a molecule relaxes to a lower excited state or the ground state of the same spin (singlet-to-singlet) without emitting a photon, or intersystem crossing (*ISC*; gray dashed arrow), another non-radiative transition where a molecule undergoes a spin conversion (singlet-to-triplet). Alternatively, the molecule can relax to the ground state through fluorescence (*F*; yellow and orange arrows), a radiative transition where a photon is emitted from a molecule in a spin-allowed singlet-singlet transition, or through phosphorescence (*P*; red and dark arrows), a slower radiative transition where a molecule emits a photon in a spin-forbidden singlet-triplet transition. Additionally, if a molecule enters the triplet state after *ISC*, it can photobleach (curved black arrow) from this state and enter a permanent dark state from which the molecule can no longer emit a photon. The timescales of these processes are summarized in Table 1.1 and are all generally faster than the time resolution of a typical SMF experiment, with the exception of some phosphorescence.[28,29] Nonetheless, these rates must be considered because the time-averaged quantities collected in SMF experiments, like brightness and photostability, are all functions of these rates.

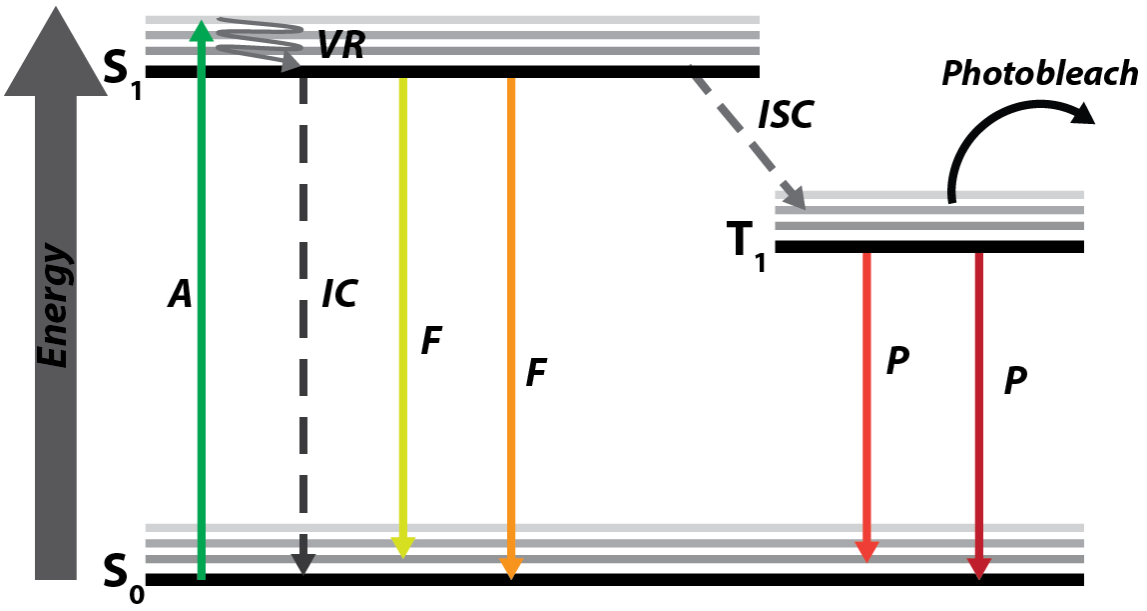

Figure 1-4. Energy diagram showing the possible transitions of an electron.

Table 1.1 Timescales of molecular electronic transitions

Transition	*Abbreviation*	*Timescale (s)*	*Radiative?*
Vibrational Relaxation	*VR*	10^{-14} - 10^{-11}	No
Internal Conversion	*IC*	10^{-14} - 10^{-11}	No
Intersystem Crossing	*ISC*	10^{-8} - 10^{-3}	No
Fluorescence	*F*	10^{-9} - 10^{-7}	Yes
Phosphorescence	*P*	10^{-4} - 10^{-1}	Yes

1.6 Using nanoparticle plasmonics for single-molecule imaging

Since ancient times, the beautiful colors of metal nanoparticles (NPs) have been used to color clothing, as well as to stain glass and ceramics.[30] Though the physics was not understood until centuries later, the vibrant colors of NP solutions come from the strong scattering properties of NPs in the visible range of the electromagnetic spectrum, making them ideal substrates for coupling to common SM probes (Figure 1-5).[30] These scattering properties arise from the resonant excitation of a localized surface plasmon (LSPR), the collective oscillation of the metal NP conduction band electrons.[31] For metal nanoparticles with a diameter, $d << \lambda$, where λ is the wavelength of incident light, the conduction band electrons are confined to the small particle volume and will move collectively in-phase upon resonant plane-wave excitation. This collective oscillation results in a buildup of polarized charges on the particle surface; these charges act as an effective restoring force and lead to for a resonant mode to occur at a specific frequency, the particle plasmon frequency.[32] The resonant charge oscillations associated with the excitation of an LSPR, in turn, give rise to a large local electric field enhancement near the nanoparticle surface.[32-34] Molecules placed in the nanoparticle near field can couple to this enhanced electric field, yielding several important effects.[30,31] First, the NP can act as an optical antenna, efficiently concentrating incident radiation in its near-field, and causing an increased excitation rate of the molecule due to enhanced local power.[35] These highly confined fields are generally referred to as “hot spots” and have been used in several near-field spectroscopies and imaging techniques, such as near-field scanning optical microscopy (NSOM) and surfaced-enhanced Raman spectroscopy (SERS).[34] Second, there will be an increased density of photonic states accessible to the nearby

molecule, and therefore, it will have an enhanced radiative decay rate according to Fermi's Golden Rule, which affirms that the spontaneous emission rate depends on the local density of states.[36] With an enhanced radiative decay rate, the quantum yield of the molecule will increase, and the photostability of the molecule will also increase.[35] Increased photostability is the result of a decreased lifetime; as the molecule spends less time in the excited state, it will have a decreased probability of undergoing *ISC* and thus a decreased probability of photobleaching (Figure 1-4) from a long-lived triplet state. [37]

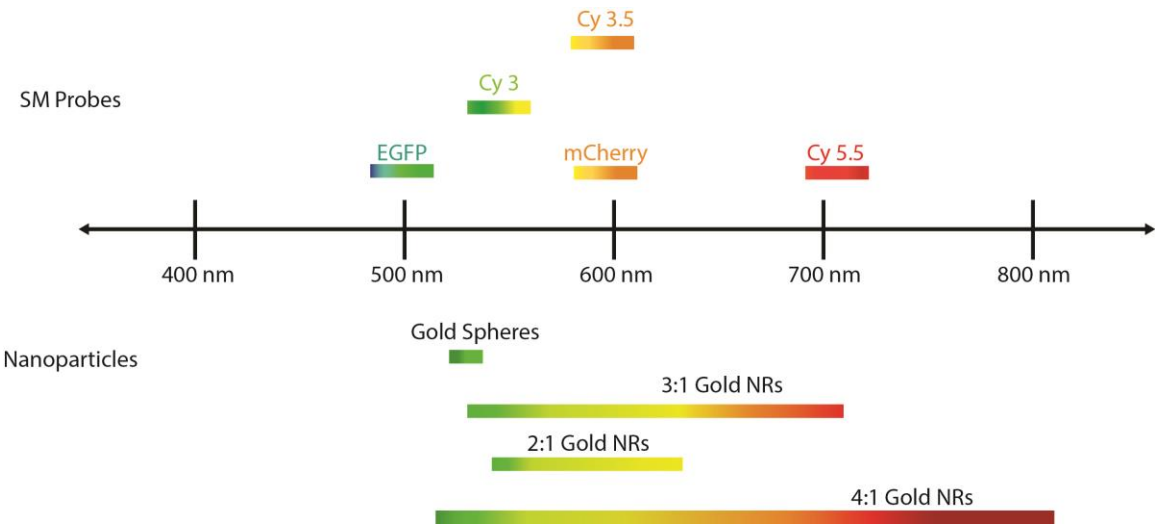

Figure 1-5. Wavelength ranges for common SM probes (dyes and FPs) and various Au nanospheres and nanorods (NRs).

Collectively, the effects of coupling a molecule to a resonantly excited plasmonic NP will lead to altered molecular optical properties. Under proper experimental conditions, increased fluorescence intensity and an increased photon yield, or the number of total photons emitted before irreversible photobleaching of the fluorophore, can be

observed.[33,35] The influence of these effects on the molecular fluorescence intensity, I_{em}, is proportional to both the excitation rate of the fluorophore in the NP near field at the excitation frequency, $\gamma_{ex}(\omega_{ex})$, and the quantum yield for the fluorophore at the emission frequency, $\Phi_{em}(\omega_{em})$. The factors $\gamma_{ex}(\omega_{ex})$ and $\Phi_{em}(\omega_{em})$ are extremely sensitive to excitation and emission frequencies, respectively, as well as to the NP shape and size, and to the distance between the NP and fluorophore.[35,38] Thus, a comprehensive understanding these parameters of the specific NP-fluorophore system being studied is of vital importance for optimizing fluorescence enhancement.

1.7 Thesis outline

In **Chapter 2** of this Thesis, we develop protocols for coupling fluorescent proteins (FPs) to plasmonic gold substrates and design *in vitro* experiments to demonstrate enhanced emission, as well as increased photostability, from single FPs coupled to gold NRs. We then show that coupling an FP to a single NR leads to a shift in the apparent emission position toward the NR center due to re-radiation through the NR plasmon mode. In **Chapter 3**, we show that plasmon-enhanced emission from single FPs can increase the fluorescence signal for *in vivo* imaging of membrane-bound proteins inside live *Vibrio cholerae* bacteria cells. In these experiments, we resolve a re-radiation pattern that is localized near the edges of gold nanotriangles and not shifted to the nanoparticle center, like what was observed in experiments done with NRs. Finally, in **Chapter 4**, we demonstrate that selective polarization-dependent excitation of anisotropic gold NRs yields polarization-dependent emission from coupled Cy5.5 dye molecules, providing a new avenue of selectivity in single-molecule experiments. In **Chapter 5**, we summarize our findings and suggest several experiments that could expand the work described in this

Thesis. Collectively, the work in this Thesis develops a new approach for improving super-resolution microscopy in living cells through exploring plasmon-enhanced FP emission, applying this understanding to *in vivo* systems, and demonstrating increased selectivity for addressing nanostructures on the nanometer scale.

References

1. Porter, J. R. Antony van Leeuwenhoek: tercentenary of his discovery of bacteria. *Bacteriol. Rev.* **1976**.

2. Huang, B.; Bates, M.; Zhuang, X. W. Super-Resolution Fluorescence Microscopy. *Annu. Rev. Biochem.* **2009**, *78*, 993-1016.

3. Henriques, R.; Griffiths, C.; Hesper Rego, E.; Mhlanga, M. M. PALM and STORM: Unlocking Live-Cell Super-Resolution. *Biopolymers* **2011**, *95*, 322-331.

4. Thompson, R. E.; Larson, D. R.; Webb, W. W. Precise nanometer localization analysis for individual fluorescent probes. *Biophys. J.* **2002**, *82*, 2775-2783.

5. Abbe, E. Contributions to the theory of the microscope and microscopic detection (Translated from German). *Arch. Mikroskop. Anat.* **1873**, *9*, 413-468.

6. Milo, R.; Jorgensen, P.; Moran, U.; Weber, G.; Springer, M. BioNumbers--the database of key numbers in molecular and cell biology. *Nucleic Acids Res.* **2009**, *38*, D750-D753.

7. Biteen, J. S.; Moerner, W. E. Single-Molecule and Superresolution Imaging in Live Bacteria Cells. *Cold Spring Harb. Perspect. Biol.* **2010**, *2*, a000448.

8. Sharonov, A.; Hochstrasser, R. M. Wide-field subdiffraction imaging by accumulated binding of diffusing probes. *Proc. Natl. Acad. Sci. U. S. A.* **2006**, *103*, 18911-18916.

9. Joo, C.; Balci, H.; Ishitsuka, Y.; Buranachai, C.; Ha, T. Advances in Single-Molecule Fluorescence Methods for Molecular Biology. *Annu. Rev. Biochem.* **2008**, *77*, 51-76.

10. Moerner, W. E.; Fromm, D. P. Methods of Single-Molecule Fluorescence Spectroscopy and Microscopy. *Rev. Sci. Instrum.* **2003**, *74*, 3597-3619.

11. Yildiz, A.; Forkey, J. N.; McKinner, S. A.; Ha, T.; Goldman, Y. E.; Selvin, P. R. Myosin V walks hand-over-hand: Single fluorophore imaging with 1.5-nm localization. *Science* **2003**, *300*, 2061-2065.

12. Churchman, L. S.; Flyvbjerg, H.; Spudich, J. A. A Non-Gaussian Distribution Quantifies Distances Measured with Fluorescence Localization Techniques. *Biophys. J.* **2006**, *90*, 668-671.

13. Shimomura, O.; Johnson, F. H.; Saiga, Y. Extraction, Purification and Properties of Aequorin, a Bioluminescent Protein from the Luminous Hydromedusan, Aequorea. *J. Cell. Comp. Physio.* **1962**, *59*, 223-239.

14. Heim, R.; Tsien, R. Y. Engineering green fluorescent protein for improved brightness, longer wavelengths and fluorescence resonance energy transfer. *Curr. Biol.* **1996**, *6*, 178-182.

15. Shaner, N. C.; Campbell, R. E.; Steinbach, P. A.; Giepmans, B. N. G.; Palmer, A. E.; Tsien, R. Y. Improved monomeric red, orange and yellow fluorescent proteins derived from *Discosoma sp.* red fluorescent protein. *Nat. Biotechnol.* **2004**, *22*, 1567-1572.

16. Tsien, R. Y. The Green Fluorescent Protein. *Annu. Rev. Biochem.* **1998**, *67*, 509-544.

17. Giepmans, B. N. G.; Adams, S. R.; Ellisman, M. H.; Tsien, R. Y. The fluorescent toolbox for assessing protein location and function. *Science* **2006**, *312*, 217-224.

18. Dickson, R. M.; Cubitt, A. B.; Tsien, R. Y.; Moerner, W. E. On/Off Blinking and Switching Behavior of Single Green Fluorescent Protein Molecules. *Nature* **1997**, *388*, 355-358.

19. Peterman, E. J. G.; Brasselet, S.; Moerner, W. E. The Fluorescence Dynamics of Single Molecules of Green Fluorescent Protein. *J Phys Chem A* **1999**, *103*, 10553-10560.

20. Ha, T.; Tinnefeld, P. Photophysics of fluorescent probes for single-molecule biophysics and super-resolution imaging. *Annu. Rev. Phys. Chem.* **2012**, *63*, 595-617.

21. Durisic, N.; Laparra-Cuervo, L.; Sandoval-Álvarez, Á; Borbely, J. S.; Lakadamyali, M. Single-molecule evaluation of fluorescent protein photoactivation efficiency using an*in vivo*nanotemplate. *Nat. Methods* **2014**, *11*, 156-162.

22. Drobizhev, M.; Makarov, N. S.; Tillo, S. E.; Hughes, T. E.; Rebane, A. Two-photon absorption properties of fluorescent proteins. *Nat. Methods* **2011**, *8*, 393-399.

23. Willets, K. A.; Nishimura, S. Y.; Schuck, P. J.; Twieg, R. J.; Moerner, W. E. Nonlinear Optical Chromophores as Nanoscale Emitters for Single-Molecule Spectroscopy. *Acc. Chem. Res.* **2005**, *38*, 549-556.

24. Kubitscheck, U.; Kueckmann, O.; Kues, T.; Peters, R. Imaging and tracking of single GFP molecules in solution. *Biophys. J.* **2000**, *78*, 2170-2179.

25. Bates, M.; Huang, B.; Dempsey, G. T.; Zhuang, X. Multicolor super-resolution imaging with photo-switchable fluorescent probes. *Science* **2007**, *317*, 1749-1753.

26. Biteen, J. S.; Thompson, M. A.; Tselentis, N. K.; Bowman, G. R.; Shapiro, L.; Moerner, W. E. Super-Resolution Imaging in Live *Caulobacter crescentus* cells Using Photoswitchable EYFP. *Nat. Methods* **2008**, *5,* 947-949.

27. Skoog, D. A.; Holler, F. J.; Crouch, S. R. In *Molecular Luminescence Spectrometry;* Principles of Instrumental Analysis; David Harris: 2007; Vol. 6, pp 399-429.

28. Harris, D. C.; Bertolucci, M. D. *Symmetry and Spectroscopy: An Introduction to Vibrational and Electronic Spectroscopy;* Dover: New York, 1978.

29. Jaffe, H. H.; Miller, A. L. The fates of electronic excitation energy. *J. Chem. Educ.* **1966**.

30. Giannini, V.; Fernandez-Dominguez, A. I.; Heck, S. C.; Maier, S. A. Plasmonic Nanoantennas: Fundamentals and Their Use in Controlling the Radiative Properties of Nanoemitters. *Chem. Rev.* **2011**, *111*, 3888-3912.

31. Willets, K. A.; Van Duyne, R. P. Localized Surface Plasmon Resonance Spectroscopy and Sensing. *Annu. Rev. Phys. Chem.* **2007**, *58*, 267-297.

32. Maier, S. A.; Atwater, H. A. Plasmonics: Localization and guiding of electromagnetic energy in metal/dielectric structures. *J. Appl. Phys.* **2005**, *98*, 011101.

33. Maier, S. *Plasmonics: Fundamentals and Applications;* Springer: New York, NY, 2007.

34. Willets, K. A.; Van Duyne, R. P. Localized surface plasmon resonance spectroscopy and sensing. *Annu. Rev. Phys. Chem.* **2007**, *58*, 267-297.

35. Anger, P.; Bharadwaj, P.; Novotny, L. Enhancement and Quenching of Single-Molecule Fluorescence. *Phys. Rev. Lett.* **2006**, *96*, 113002.

36. Barnes, W. L. Fluorescence near interfaces: The role of photonic mode density. *J. Mod. Opt.* **1998**, *45*, 661-699.

37. Lakowicz, J. R.; Fu, Y. Modification of single molecule fluorescence near metallic nanostructures. *Laser Photon. Rev.* **2009**, *3*, 221-232.

38. Chen, Y.; Munechika, K.; Ginger, D. S. Bioenabled nanophotonics. *MRS Bull* **2008**, *33*, 536-542.

Chapter 2 Plasmon-Enhanced Brightness and Photostability from Single Fluorescent Proteins Coupled to Gold Nanorods

The work presented in this chapter was published in the following paper:

J. E. Donehue, E. Wertz, C. N. Talicska, J. S. Biteen, "*Plasmon-enhanced brightness and photostability from single fluorescent proteins coupled to gold nanorods*," Journal of Physical Chemistry C, **118**, *2014*, 15027-15035.

2.1 Abstract

Single-molecule imaging pushes fluorescence microscopy beyond the diffraction limit of traditional microscopy. Such super-resolution imaging, which relies on the detection of bright, stable fluorescent probes to achieve nanometer-scale resolution, is often hindered in biological systems by dim, blinking fluorescent proteins (FPs). Here, we use gold nanorods and single-molecule fluorescence detection to achieve plasmon-enhanced emission from intrinsically fluorescent proteins. We measure a doubled photon emission rate from the red FP mCherry, and detect three times more photons before photobleaching from the photo-activatable FP PAmCherry. We further explore the effect of near-field nanorod interactions on the yellow FP mCitrine, for which the observed emission enhancements cannot overcome measurable quenching. Overall, our work indicates that plasmonic particles improve both the brightness and photostability of FPs,

and extends the applications of plasmon-enhanced fluorescence to the arena of biological imaging. Furthermore, because gold nanorods are non-toxic, they are promising extracellular imaging substrates for enhancing emission from FP-labeled membrane-bound proteins in live cells.

2.2 Introduction

In recent years, super-resolution imaging has revolutionized the study of biological systems and structures, providing high sensitivity and nanometer-scale resolution. In a typical super-resolution microscopy experiment, a biological molecule of interest is conjugated to a fluorescent label. Single, spatially isolated, labeled molecules serve as point light sources with emission profiles that approximate the point-spread function (PSF) of the microscope. By fitting the diffraction-limited emission profile of the label, the position of the emitter can be determined on the nanometer scale—far better than the standard diffraction limit of light.[1] In fact, the precision of this technique is mostly limited mainly by the number of detected photons,[2] and *in vitro* implementations of single-molecule fluorescence (SMF) imaging have determined the position of Cy3-labeled motor proteins with 1.5-nm localization precision.[3] Though intense single-molecule signals and accordingly excellent localization precisions are achieved with such bright organic dyes, the most common method for labeling proteins of interest *in vivo* is with genetically encoded fusions to fluorescent proteins (FPs). The main advantage of this approach is that the FP is covalently bound to the protein of interest and can be expressed with high specificity inside the cell, without need for trans-membrane introduction of dyes or cofactors.[4] Advances via genetic mutations have led to a library of monomeric FPs spanning the visible spectrum in excitation and emission frequencies.

Furthermore, photo-activatable FPs, which can be switched from an initial dark state to a fluorescent state by irradiation with violet light,[5] increase the utility of these fluorescent probes for super-resolution microscopy techniques such as photoactivatable localization microscopy (PALM),[6] fluorescence photoactivated localization microscopy (FPALM),[7] and stochastic reconstruction microscopy (STORM).[8]

Fluorescent proteins are therefore an important tool with many advantages for bio-imaging. However, FPs have slower radiative decay rates than bright, organic dyes conventionally used for single-molecule imaging, making FPs less photostable and reducing their quantum yield.[9] Indeed, prior to photobleaching, typical FPs emit an order of magnitude fewer photons than small-molecule dyes.[10,11] Thus, while single molecules of Cy3-labeled myosin have been observed walking *in vitro* for minutes,[3] cellular single-FP tracking experiments are often limited to short trajectories of only a few seconds. The poor photophysical properties of FPs reduce the accuracy with which diffusive and directional motion can be characterized and make single-FP tracking inadequate for longer timescale processes.[12] Additionally, the time resolution of live-cell single-molecule imaging depends on the FP fluorescence brightness. By enabling imaging at faster camera frame rates, high fluorescence quantum yields allow observations of fast dynamics. However, while GFP is relatively efficient with a quantum yield of 77%,[13] redder FPs, which are preferred in bio-imaging due to a weaker cellular autofluorescence background at longer wavelengths, have significantly lower quantum yields. For example, the red FP mCherry has a 22% quantum yield,[14] making fast dynamics of this probe difficult to capture. Overall, because the single-molecule localization precision depends on the total number of photons detected, deficiencies in FP radiative rates (and

therefore photostabilities and quantum yields) generally limit the resolution of SMF imaging in cells to 10–40 nm.[15,16] This tens-of-nanometers localization precision precludes the use of SMF to directly visualize molecular-scale interactions of small biomolecules like proteins, which are 1–2 nm in size. Therefore, improving the radiative rate of FPs and creating brighter, longer-lived probes will yield improved trajectory lengths, imaging rates, and localization precisions to overcome current limitations.

In this chapter, we use plasmon-enhanced fluorescence to improve the emissive properties of FPs. Noble metal nanoparticles support local surface plasmon resonances (LSPRs), the collective oscillations of conduction-band electrons.[17] These LSPR excitations produce a large electric field concentration in the nanoparticle near field, which will amplify the excitation rate of a fluorescent molecule due to enhanced local incident power, and will enhance the molecular radiative decay rate by increasing the density of accessible photonic states.[18] Indeed, coupling to an enhanced field leads to brighter molecules by enhancing the rates of both excitation and decay. Since the fluorescence decay rate, Γ_{em}, is the product of the excitation rate, Γ_{exc}, and the quantum yield, Φ_{QY},[18] the fluorescence decay rate is the experimental observable most significantly affected by plasmonic coupling. Additionally, increasing the radiative decay rate leads to more photostable fluorophores, as the molecules spend less time in the excited state, decreasing the probability of intersystem crossing, and thus the rate of photobleaching from the long-lived triplet state.[19] Collectively, these effects can increase both the total number of photons emitted before photobleaching and the number of photons detected in each imaging frame. Very close coupling ($\lesssim$ 3 nm) does lead to

additional non-radiative decay pathways, Γ_{nrad}, but this quenching effect is small for larger distances, and the smallest separation distances can be avoided.[20,21]

Extensive research on plasmon-enhanced fluorescence (also referred to as metal-enhanced fluorescence) of dyes and quantum dots suggests that this technique is also ideally suited for solving problems inherent in FP-based fluorescence imaging.[22-35] Here, we couple the FPs mCherry, PAmCherry, and mCitrine to the biocompatible plasmonic substrate gold nanorods (NRs). The gold NR asymmetry produces two plasmon modes corresponding to electron oscillations along the longitudinal (long) axis and the transverse (short) axis of the rod. These two plasmon modes can therefore couple to the red (mCherry and PAmCherry) and yellow (mCitrine) emitting FPs, respectively. Like all other commonly used FPs, mCherry, PAmCherry and mCitrine are composed of a small chromophore encapsulated in a ß-barrel scaffold. FP chromophores are very sensitive to their environment, and indeed, they are very poor emitters when removed from the ß-barrels that surround them,[36-39] a property distinguishing them from typical organic dyes. In this work, we find that plasmonic interactions are not degraded by these unique environmental sensitivities, and we can therefore indeed produce brighter and more photostable FPs for single-molecule imaging by coupling to the enhanced field about plasmonic nanoparticles.

2.3 Experimental Methods

2.3.1 Fluorescent proteins

Solutions of mCherry were made from reconstituted purified proteins (BioVision, Inc.). Solutions of mCitrine and PAmCherry were prepared from purified proteins harvested from *E. coli* cells, as described below in *Biological Methods.*

2.3.2 Biological methods

Solutions of mCherry were made from reconstituted purified proteins (BioVision, Inc.), and mCitrine and PAmCherry solutions were prepared from purified proteins harvested from Escherichia coli cells.

His-tagged mCitrine FPs were purified from cultures of BL21(DE3) competent *E. coli* cells transformed with pET-mCitrine (Addgene #29771).[5] BL21(DE3) cells were grown overnight in LB with 50 μg/mL ampicillin at 37°C with shaking, then diluted 100-fold into fresh media. Cells were grown to an optical density of 0.6 at 600 nm, at which point protein expression was induced by the addition of Isopropyl β-D-1-thiogalactopyranoside (IPTG) to a final concentration of 1 mM. Cells were harvested by centrifugation (10 min, 3000 ×g) 2.5 hours after induction, and lysed with B-PER^{TM} solution (ThermoScientific). His-tagged PAmCherry FPs were purified from cultures of DH5α competent *E. coli* cells transformed with pBAD/HisB-PAmCherry1 (Addgene #31931).[58] DH5α cells were grown overnight in LB with 50 μg/mL ampicillin at 37°C with shaking, then diluted 100-fold into fresh media. Cells were grown to an optical density of 0.6 at 600 nm, at which point protein expression was induced by the addition of arabinose to a final concentration

of 0.2%. Cells were harvested by centrifugation (10 mins, 3000 ×g) 20 hours after induction and lysed with B-PER solution (ThermoScientific).

Both of the His-tagged FPs were purified using a spin column (HisPur^{TM} Ni-NTA, ThermoScientific). mCitrine was further purified in a Zeba Spin Desalting Column (ThermoScientific) with a 7-kDa molecular weight cut-off. Protein purity was assayed using polyacrylamide gel electrophoresis, and final protein concentration was determined from absorption at 280 nm (NanoDrop 2000 UV-Vis).

2.3.3 Gold nanorod substrates

Glass microscope coverslips were coated with 100 nm ITO by sputter deposition (Kurt J. Lesker, Lab 18-1), cleaned using an O_2-plasma etch (200 mTorr, 10 mins, PE-50, Plasma Etch Inc.), then lithographically patterned with 2 μm × 2 μm gold crosses for aligning optical and SEM images. Gold nanorod substrates were prepared using a spin-assisted layer-by-layer technique,[40] where polyelectrolyte films of positively charged poly(diallyldimethyl ammonium chloride) solution (PDADMAC, Sigma Aldrich) and negatively charged poly(sodium 4-styrene) solution (PSS, Sigma Aldrich) were used to immobilize gold nanorods (NRs) to the surface of the ITO-coated coverslips. NRs were purchased from Nanopartz Inc. (Loveland, CO) and used as received. Polyelectrolyte solutions (20% by weight in water) were diluted in DDI water to 20 mM (calculated using monomeric weights). Dilute PDADMAC was spun onto the cleaned coverslips (300 μL, 15 s, 4000 rpm), then washed 3 times with DDI water. A mixture of NRs and dilute PSS was then spun onto the coated coverslip (100 μL NRs, 200 μL PSS, 15 s, 4000 rpm), followed by 3 DDI water washes. NR substrates were characterized by single molecule localizations (Figure 2-1) and by high-resolution scanning electron microscopy

(FEI NOVA 200 Nanolab SEM/FIB, 10-kV accelerating voltage), showing a density of 2 – 3 NRs/625 μm^2, where 625 μm^2 corresponds to the imaging area of the epifluorescence experiments.

2.3.4 Immobilized PAmCherry fluorescent proteins on nanorods

Concentrated NR films were prepared on ITO-coated glass coverslips that had been cleaned 10 min in an O_2 plasma. 4 mL of 112 nm × 53 nm NRs was centrifuged 3 min in Eppendorf tubes at 2500 ×g to concentrate. The supernatant was removed and the concentrated fraction (400 μL) was used to prepare a more dense NR substrate. 20 mM PDADMAC was spun onto the cleaned ITO-coated coverslips (300 μL, 15 s, 4000 rpm), then washed 3 times with DDI water. A mixture of 100 μL concentrated NRs and 200 μL 20 mM PSS was then spun onto the coated coverslip (15 s, 4000 rpm), followed by 3 washes with DDI water. NR substrates were characterized by high-resolution scanning electron microscopy (FEI NOVA 200 Nanolab SEM/FIB, 10-kV accelerating voltage), revealing a greater density of NRs on sample (15-20 NRs/625 μm^2), as compared to previous dilute samples. To immobilize PAmCherry above the NR substrate, a thin layer of PDADMAC (20 mM, 300 μL, 15 s, 4000 rpm) was spun on to the substrate surface, followed by 3 washes with DDI water, and then the final layer of 16 μL 45-μM PAmCherry in 284 μL 20-mM PSS was spun on top (15 s, 4000 rpm).

2.3.5 Epifluorescence microscopy

Wide-field epifluorescence microscopy was performed with a 1.40-NA oil-immersion objective in an Olympus IX71 inverted microscope. Single mCitrine molecules were excited with circularly polarized 488-nm laser light (Coherent Sapphire 488-50 and Tower Optical .250-488 quarter waveplate) or circularly polarized 514-nm laser light

(Spectra-Physics 514 and Tower Optical .250-515 quarter waveplate), and single mCherry and PAmCherry molecules were excited with circularly polarized 561-nm laser light (Coherent Sapphire 561-50 and Tower Optical .250-556 quarter waveplate). Excitation intensities were 23 – 24 W/mm^2 for PAINT experiments, and 15 W/mm^2 for immobilized-FP experiments. Photo-activation of PAmCherry was achieved using short pulses (200 ms, 15 W/mm^2) of circularly polarized 406-nm laser light (Coherent Cube 406 and Tower Optical .250-405 quarter waveplate). Fluorescent emission was filtered appropriately (Semrock Di01-R488/ BLP01-488, Di01-R488/BLP01-514, or Di01-R561/BLP01-561R) to maximize signal and minimize scattered laser light, then imaged on a 512×512 pixel Andor iXon EMCCD at 40 ms/frame (for PAINT experiments) or on a 512×512 pixel Photometrics Evolve EMCCD at 100 ms/frame (for immobilized experiments) for 0.5 – 2 minutes. Emission intensities, molecular positions and total emitted photons were extracted from the data by least-squares fitting molecules to a 2D Gaussian function with the MATLAB routine *nlinfit*.

2.3.6 Dark field scattering spectroscopy

NR substrates for dark-field experiments were prepared on O_2-plasma cleaned glass coverslips as described above. A broadband halogen light source (400 – 1000 nm) was used to excite the sample through a dark-field condenser and scattered light was collected using an Olympus IX71 inverted microscope equipped with a dark-field oil-immersion objective (NA = 0.6). NR substrates were immersed in water and covered by a microscope slide. The diffraction-limited image of a single NR was aligned to the entrance slit of an imaging spectrograph (Acton 2300, Princeton Instruments) and spectral data was collected with an EMCCD (Andor iXon). Background spectra

(collected from nearby positions with no NR image on entrance slit) were subtracted from measured spectra and all data were divided by the broadband spectrum of the halogen light source to correct for the system spectral efficiency.

2.3.7 PAINT imaging of fluorescent proteins on nanorods

In PAINT experiments, 75 μL – 100 μL of 175 nM FP in PBS was placed on top of the NR substrates and contained by a small rubber O-ring that had been previously cleaned by sonication in acetone.

2.3.8 Background subtraction methods

Gold NRs are known to efficiently scatter light and fluoresce under the proper conditions. However, as this signal is constant over time during all of our experiments, we subtract this background before image processing. The fluorescence images in Figure 2-6b and Figure 2-10c are examples of such background-subtracted images. A raw data movie from a PAINT experiment, as well as the same movie after background subtraction demonstrate that no NR scatter or fluorescence appears in the movies we fit.

2.4 Results and Discussion

2.4.1 Spectral properties of fluorescent proteins and gold nanorods

Gold nanorods (Nanopartz Inc.) were used as received and immobilized (Figure 2-1) in polyelectrolyte films on the surface of glass coverslips[40] that were coated via sputter deposition with indium tin oxide (ITO). This ITO coating provided a conductive substrate for scanning electron microscopy (SEM). A UV-visible absorbance spectrum of a nanorod (NR) solution indicated a monodisperse sample (Figure 2-2). To characterize relevant NR optical properties in actual experimental conditions and

geometry, however, the dark-field scattering of isolated gold NRs immobilized on ITO-coated microscope coverslips and immersed in water was measured, and the scattering spectrum from a representative NR is shown in Figure 2-4, dotted lines. Additional representative scattering spectra are plotted in Figure 2-3. The transverse plasmon mode peak at 541 nm scatters much less than the longitudinal plasmon mode peak at 620 nm, indicating that the transverse mode is the weaker mode. The mCherry and mCitrine FPs were chosen for their spectral overlap with these two measured NR plasmon modes; the solid lines in Figures 2-4a and 2-4b show the fluorescence excitation and emission spectra of mCherry and mCitrine, respectively, measured in solution at 175 nM – 350 nM concentrations. The emission maximum of mCitrine (529 nm) overlaps well with the NR transverse mode, while the emission maximum of mCherry (610 nm) overlaps well with the NR longitudinal mode

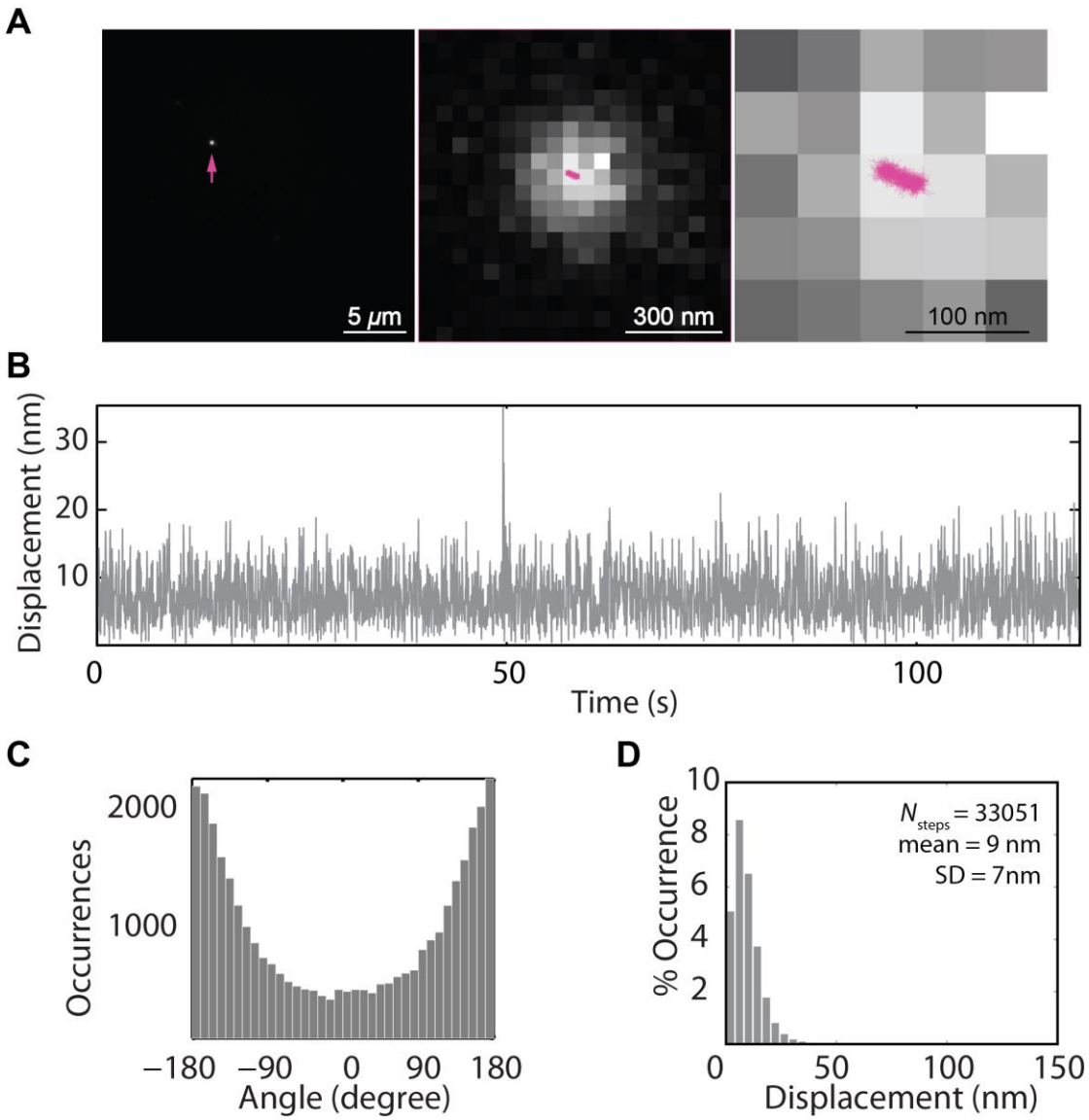

Figure 2-1. (A) Single-molecule localizations of a representative gold NR immobilized in poly(sodium 4-styrene) and immersed in PBS buffer (pH = 7.4) over the course of 120 s. The super-resolved trajectory of the NR (pink) is superimposed on a diffraction-limited fluorescence image of the NR. Three successively zoomed in views demonstrate that the NR apparent position is confined to an area of roughly 200 nm^2 over the course of the experimental timescale. (B) Apparent step sizes of the NR in (A). (C) Histogram of the angles between each set of two consecutive NR steps for 11 immobilized gold NRs. The distinctive U-shaped distribution is expected for immobile molecules localized in the presence of Gaussian fitting noise.[59] (D) Histogram of all apparent displacements for the 11 gold NRs in (C). These measured displacements are due to nanometer-scale localization errors and stage drift; these small displacements indicate that the NRs are well immobilized in the aqueous environment on the timescale of the PAINT experiments.

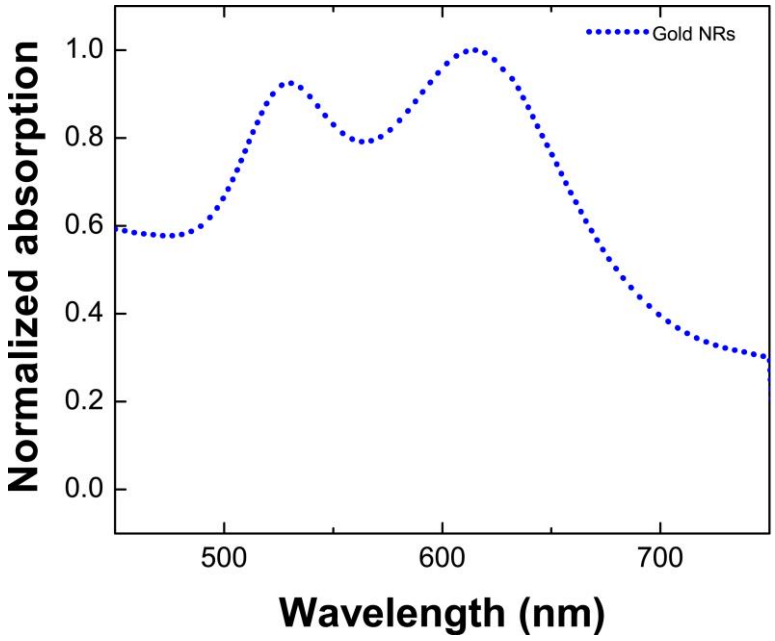

Figure 2-2. Absorption spectrum of gold NRs (112 nm x 53 nm) in aqueous solution (measure at 1.5×10^{10} NRs/mL).

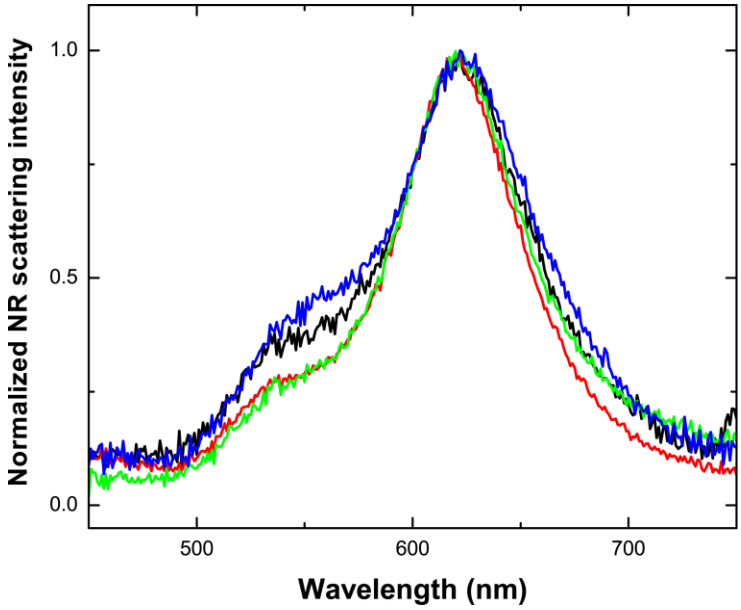

Figure 2-3. Comparison of four representative single-NR scattering spectra measured by dark-field microscopy. The transverse mode consistently appears at 541 nm ± 2 nm and the longitudinal mode appears at 622 nm ± 1 nm. The intensities of each peak represent the relative strengths of the two plasmon modes

.

2.4.2 PAINT detection of mCherry coupling to the nanorod longitudinal mode

The PAINT super-resolution method (Points Accumulation for Imaging in Nanoscale Topography)[41] was used to study the coupling of FPs and NRs. In these PAINT experiments, the NR substrate was immersed in a FP solution, from which FP molecules stochastically adsorbed on and desorbed from the surface over time (Figure 2-5). FPs that adsorbed to the substrate surface were visualized on the EMCCD detector as discrete punctate spots, whereas free FPs in solution (those molecules not adsorbed onto the substrate surface) were invisible because their motion was too fast to be resolved by the EMCCD (at a 25-Hz frame rate). Maintaining a low concentration (175 nM) of FPs in solution ensured spatially isolated single-molecule adsorption events, and each detected burst of light was fit using a super-resolution algorithm to determine the position and intensity of emission. A 6 × 6 pixel (294 × 294 nm) region of interest (ROI) centered about the NR was identified from a fit to the diffraction-limited NR scattering image, and we compare the emission of FPs adsorbing to this "on-NR" region, which encompasses the NR near-field where FPs are strongly coupled to the resonantly enhanced local field, to the emission of FPs adsorbing outside of the NR-proximal ROI ("off-NR").

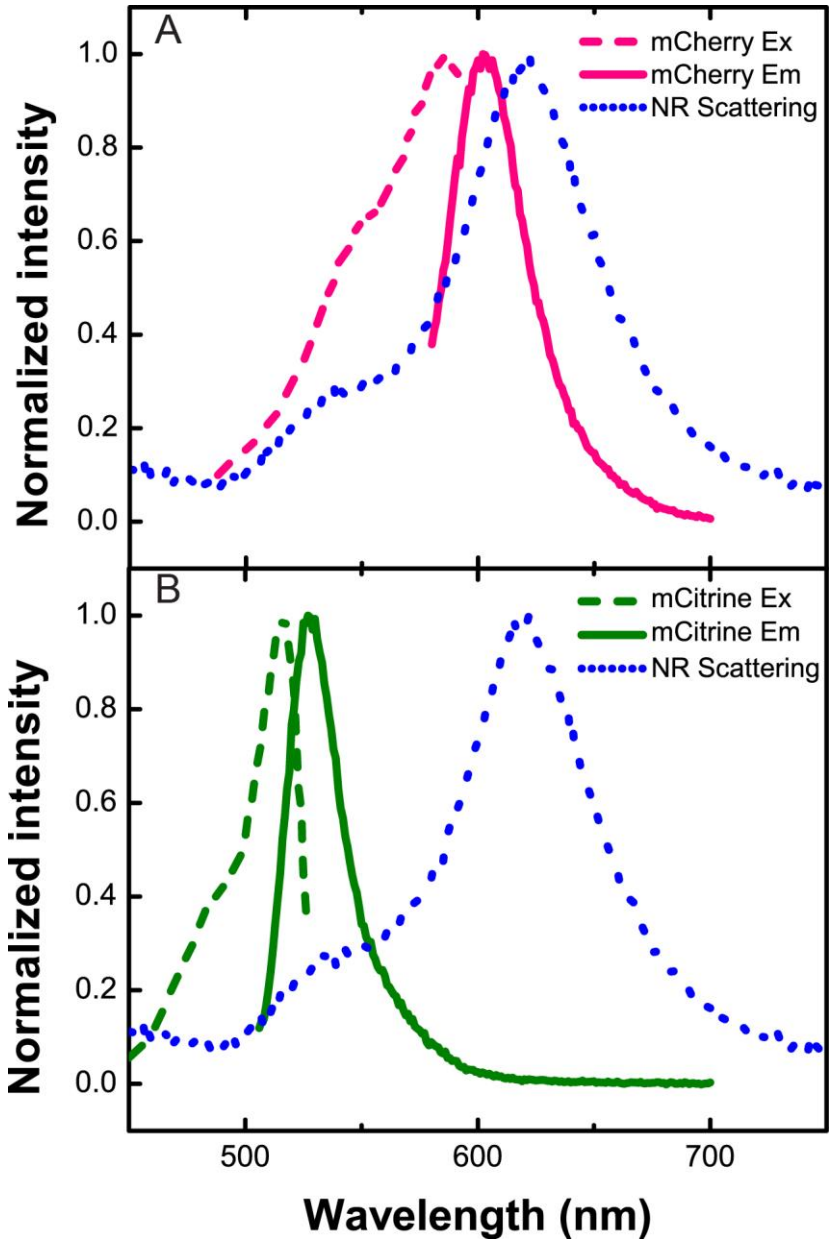

Figure 2-4. Dark-field scattering spectra of 112 nm × 53 nm gold NRs (blue dotted lines) and fluorescence excitation (dashed lines) and fluorescence emission (solid lines) spectra of (a) mCherry and (b) mCitrine. The mCherry spectra are also representative of PAmCherry. NR scattering spectra were collected in water. FP spectra were collected in PBS buffer (pH = 7.4).

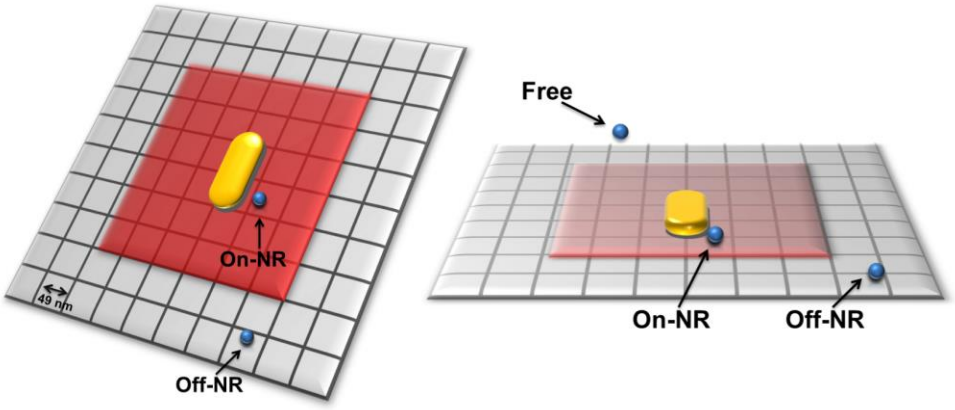

Figure 2-5. Schematic of PAINT experiments. Due to rapid Brownian motion, FPs (blue spheres) are invisible when free in solution and detected only when they adsorb on the substrate surface. The image is acquired on a region of the pixelated EMCCD detector centered about the midpoint of the gold NR scattering image. The 6 × 6 pixel on-NR area is shown in red, while everything outside this region is consider the off-NR area. Each box in grid represents a 49 × 49 nm imaging pixel.

Based on spectral overlap of mCherry emission and NR scattering (Figure 2-4a), mCherry FPs are predicted to couple to the NR longitudinal mode. In Figures 2-6a-d, the brightness of mCherry FPs adsorbing on a gold NR substrate under 561-nm excitation (pump intensity = 23 W/mm^2) is examined. In these experiments, the NR scattering and photoluminescence,[42,43] which is constant in time and intensity, appears as a diffraction-limited spot. This background scattering signal was recorded during a imaging frame in which no FP adsorption occurred, and subsequently subtracted from all imaging frames prior to further analysis (Section 2.3.8). Analyzed movies show that no NR scattering from the raw data (top) is present in the background-subtracted data (bottom). Figures 2-6a and 2-6b show representative background-subtracted epifluorescence images of single mCherry FPs adsorbing on and off gold, respectively, on the same grayscale. Figure 2-6c shows the intensity profiles across the centers of each of these molecules in pink and black, respectively. The intensity of the on-NR molecule is more than 2- fold higher than

that of the off-NR molecule, showing an example where coupling leads to a brighter molecule.

Single-molecule images of 4533 adsorbed mCherry FPs were analyzed from background-subtracted movies using a super-resolution algorithm based on Gaussian fitting.[15] The resulting localizations were divided into on-NR and off-NR as described above (Figure 2-5), and the fits from the two populations were binned according to number of photons detected per second (Figure 2-6d). Figure 2-6d shows a significantly broader and brighter distribution for mCherry FPs coupled to NRs (on-NR population) relative to off-NR mCherry. The average photon detection rate for the off-NR population is 20,800 photons/s, while the average photon detection rate for the on-NR population is 44,400 photons/s (Table 2.1). Though a substantial enhancement is observed, we note that this observed improvement is only a lower limit on the maximum experimentally achieved enhancement because the on-NR data is averaged over all possible FP dipole orientations, as well as over FP-NR separation distances up to 150 nm.

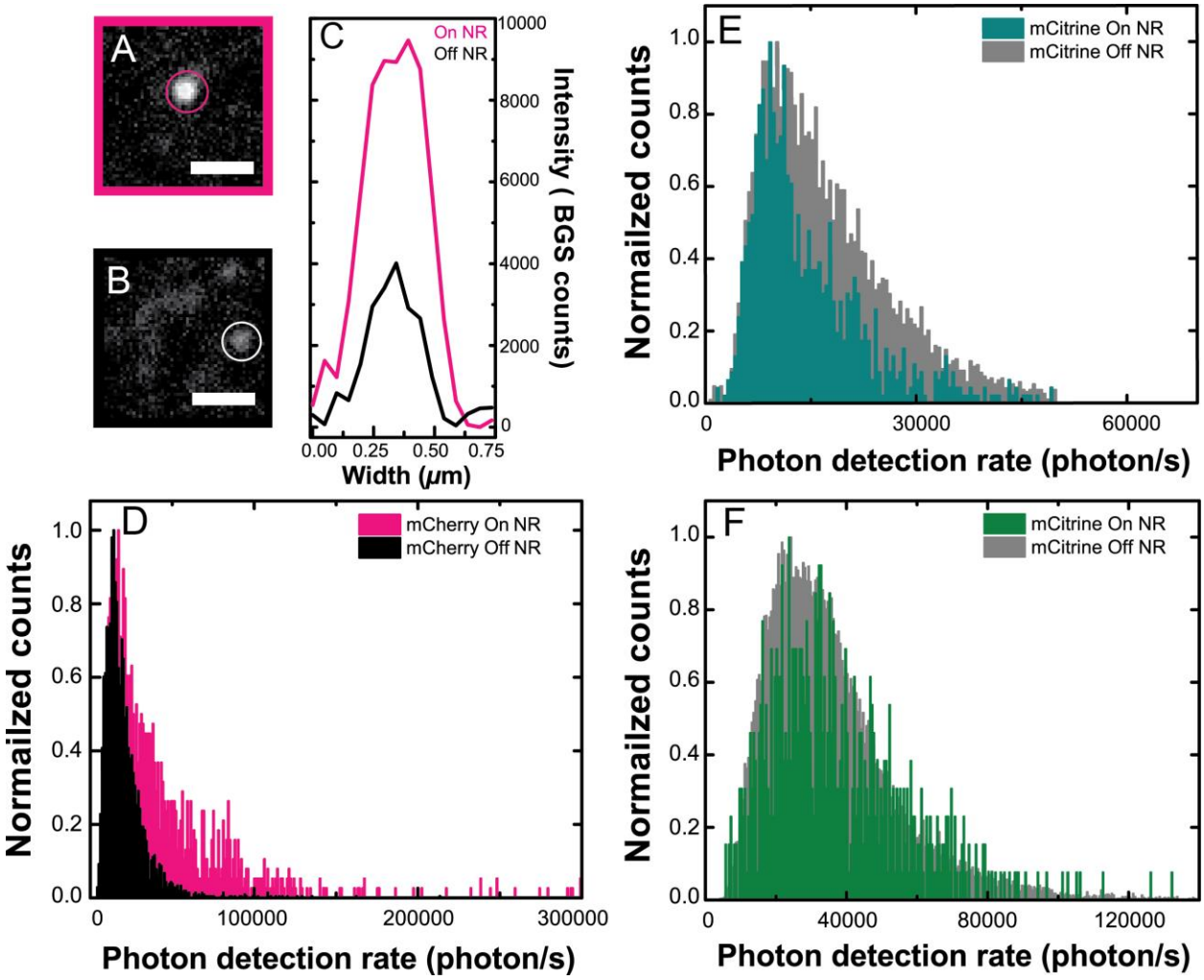

Figure 2-6. (a) and (b) Representative epifluorescence images of single mCherry FPs adsorbed on and off gold, respectively. Scale bars: 1 μm. (c) Intensity profiles across the centers of mCherry molecules in (a) and (b) (pink and black curves, respectively). (d) Comparison of single-molecule fluorescence photon detection rate for mCherry FPs on gold NRs (pink) and off NRs (black). Average rate of photon detection on gold NRs is 44,400 photons/s. Average rate of detection off gold NRs is 20,800 photons/s. 561-nm laser excitation intensity: 23 W/mm^2. (e) and (f) Comparison of single-molecule fluorescence photon detection rate on gold NRs (teal and green) and off gold NRs (gray) for mCitrine FP molecules excited at (e) 488 nm and (f) 514 nm. With 488-nm excitation, the on-NR population has an average detection rate of 14,600 photons/s, while the off-NR population has an average detection rate of 17,900 photons/s. With 514-nm excitation, on average 37,100 photons/s are detected from the on-NR population, and the off-NR population has an average rate of detection of 36,200 photons/s. 488-nm laser excitation intensity: 24 W/mm^2, 514 nm laser excitation intensity: 24 W/mm^2. Statistics for the total number of localizations per PAINT experiment available in Table 1.

Table 2.1 Summary of photon detection rate distribution parameters for mCherry and mCitrine PAINT experiments

FP/substrate	Pump intensity (W/mm^2)	Pump wavelength (nm)	Mean photon detection rate (photons/s)	Standard deviation	Median detection rate (photons/s)	Ratio of means (on-NR/off-NR)	Figure number
mCherry/on NR	23	561	44400	43000	31400	2.13	6d
mCherry/off NR	23	561	20800	13500	17400	-	6d
mCitrine/on NR	24	488	14600	8500	11900	0.82	6e
mCitrine/off NR	24	488	17900	11000	15200	-	6e
mCitrine/on NR	24	514	37100	19400	33000	1.03	6f
mCitrine/off NR	24	514	36200	20300	32000	-	6f

The observed enhancement of FP emission upon coupling to gold NRs is beneficial for super-resolution imaging for three reasons: (*1*) brighter FPs will increase the number of photons detected per imaging frame, improving the localization precision of each single-molecule fit, (*2*) more photons detected per second enables increased imaging speeds, and (*3*) faster radiative rates lead to an overall increase in photostability, thereby increasing the lengths of observable single-molecule trajectories. Additionally, as the precision of single-molecule localization is related to the number of detected photons, an improvement in experimental localization precision is expected. Average localization precisions were determined using the 95% confidence interval on the estimation of emitter position,[15] and indeed, for fits of the brighter on-NR population, we observe an average localization precision of 18 nm, while the average localization precision for the off-NR population fits was 31 nm. This improvement in experimental localization precision (1.7×) agrees well with the theoretical prediction that localization precision will

be inversely related to the square root of the number of photons detected,[2] since experimentally we observed a 2.1× increase in photons per second.

2.4.3 PAINT detection of mCitrine coupling to the nanorod transverse mode

To study coupling between FPs and the NR transverse mode, we examined the yellow FP mCitrine, which has an emission maximum that is resonant with the NR transverse mode. NR substrates were immersed in a solution of the yellow FP mCitrine for PAINT experiments. Due to the broad mCitrine excitation spectrum (Figure 2-4b), this FP can be excited by a 488-nm laser, which does not overlap with the NR scattering spectrum, or by 514-nm excitation, which overlaps well with the NR scattering spectrum. Under 488-nm excitation (Figure 2-6e), the on-NR mCitrine population (teal) has a substantially reduced average photon detection rate relative to off-NR mCitrine (gray): the mCitrine brightness is reduced from an average of 17,900 detected photons/s off gold to an average of 14,600 detected photons/s on gold. Here, the 488-nm excitation is off-resonance with the transverse plasmon mode, so no absorption enhancement can occur, and the decrease in the average photon detection rate for those molecules on gold may be due to quenching, as is typical for metal-fluorophore nonradiative energy transfer interactions.[44] However, absorption enhancement becomes possible when the same mCitrine/NR sample is excited at 514 nm, resulting in an enhanced photon detection rate that balances quenching and results in no observable net enhancement (Figure 2-6f).

These data reveal a clear difference in the ratio of quenching to enhancement for the mCitrine and mCherry FPs. This is consistent with the dark-field scattering spectra of isolated gold NRs (Figure 2-4), in which the transverse plasmon mode at 541 nm scatters light much less efficiently than the longitudinal plasmon mode at 620 nm, indicating that

the transverse mode is the weaker of the two modes. Indeed, Ming et al. demonstrated that fluorophores embedded in a silica shell around gold NRs are greatly enhanced by the NR longitudinal mode,[45] while Fu et al. showed strong enhancements of nanorod end-linked fluorophores.[46] Additionally, a theoretical investigation by Lu and coworkers highlighted that the longitudinal gold NR mode can act as a very efficient antenna at long distances (up to 50 nm),[47] while cathodoluminescence experiments and calculated scattering spectra from Knight et al. indicate the transverse mode of NRs is quite weak.[47,48]

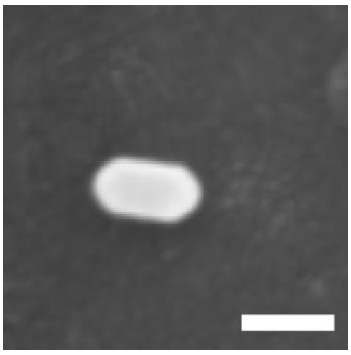

Figure 2-7. Scanning electron microscope image of representative gold NR used in PAINT experiments. Scale bar: 100 nm.

2.4.4 Single-molecule mapping detects the optical antenna effect

In addition to providing a measure of fluorescence intensity for each adsorbed FP, the PAINT experiments described above also indicate the apparent position of emission for each adsorption event. We assigned the center position of each sub-diffraction limit ellipsoidal NR by fitting the scattering intensity, and used alignment markers and SEM imaging to verify that diffraction-limited images were indeed isolated NRs (Figure 2-7). For every mCherry and mCitrine molecule detected in the vicinity of a representative,

isolated NR (greyscale diffraction-limited scattering image), we plot the apparent positions as a dot, in Figures 2-8a and 2-8b, respectively. Here, cyan dots represent FP localizations with photon detection rates equal to the average off-NR rate, red dots represent localizations with enhanced (greater than one standard deviation above the off-NR average) photon detection rates, and yellow dots represent localizations with diminished (more than one standard deviation below the off-NR average) photon detection rates.

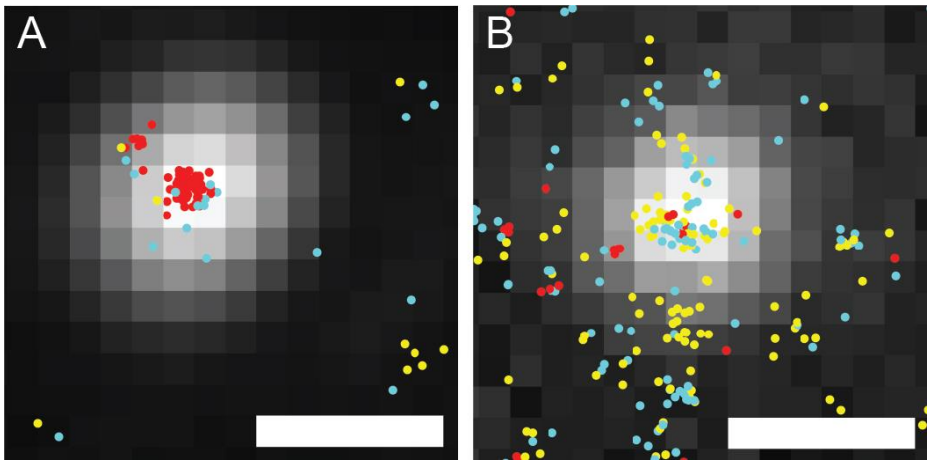

Figure 2-8. Single-molecule position maps of PAINT data (yellow, cyan and red dots) for mCherry (a) and mCitrine (b) overlaid on a diffraction-limited image of isolated gold NRs (grayscale). PAINT data and diffraction-limited image were registered using alignment markers. Each dot shows the center position of the emission detected from a single FP molecule adsorbing on or near the NR. Cyan dots indicate localizations with intensities near the off-NR average, while red dots indicate localizations with enhanced (greater than one standard deviation above the off-NR average) intensities and yellow dots indicate localizations with diminished (less than one standard deviation below the off-NR average) intensities. Scale bars: 300 nm.

In Figure 2-8a, the majority of red localizations occur for FPs very close to the NR, this supports our hypothesis that the enhanced photon detection rate is due to near-field FP-nanoparticle coupling. Strikingly, the very dense, enhanced mCherry population clustered at the NR center in Figure 2-8a shows that when NR-mCherry coupling occurs,

not only is the intensity of the FP emission is enhanced, but also the apparent position of emission is shifted to the NR location. Importantly, this observed clustering occurs despite the fact that the position at which FPs adsorb to the microscope coverslip will be random. Consistent with work by Taminiau et al.,[49] we observe that the NRs are acting as optical antennas. Furthermore, in Figure 2-8b, though little mCitrine enhancement is observed (i.e., few dots are red), the apparent emission from randomly distributed mCitrine molecules is still slightly clustered at the NR center. Interestingly, this shows that emission shifting occurs for NR-mCitrine interactions, even in the absence of strong enhancement, and we attribute the localization pattern to the more subtle coupling between mCitrine FPs and the transverse NR mode. Overall, the increased density of FP localizations near the NR centers in Figures 2-8a and 2-8b gives experimental evidence of the NRs behaving as optical antennas in the case of both strong and weak fluorescence enhancement.

2.4.5 PALM imaging of total photon yield

The PAINT experiments described above for mCherry and mCitrine detect the emission from FP molecules as they adsorb on a substrate to determine the photon detection rates. However, because the FP can desorb from the surface before photobleaching in this experimental geometry (Figure 2-5), PAINT experiments cannot measure the *total* number of photons emitted prior to photobleaching. To measure total detected photons, we immobilized a dense collection of FPs in a polyelectrolyte layer on top of a gold NR substrate (Figure 2-9a). Here, the FPs are packed closer together than the standard diffraction limit, and as a result, imaging all FPs simultaneously would prevent detection at the single-molecule level. We therefore used the photo-activatable red FP

PAmCherry[50] and PALM imaging to fulfill the low-density requirement of single-molecule imaging: PAmCherry is initially dark (non-absorbing) and can be switched into an emissive state by photo-activation with 406-nm illumination (Figure 2-9b). This photo-activated subset was imaged with 561-nm excitation (15 W/mm^2) until bleached (Figure 2-9c), and then the cycle of photo-activation and imaging was repeated (Figure 2-9d-e) until all the FPs were bleached. Background subtraction of the constant NR scattering signal was ensured as above.

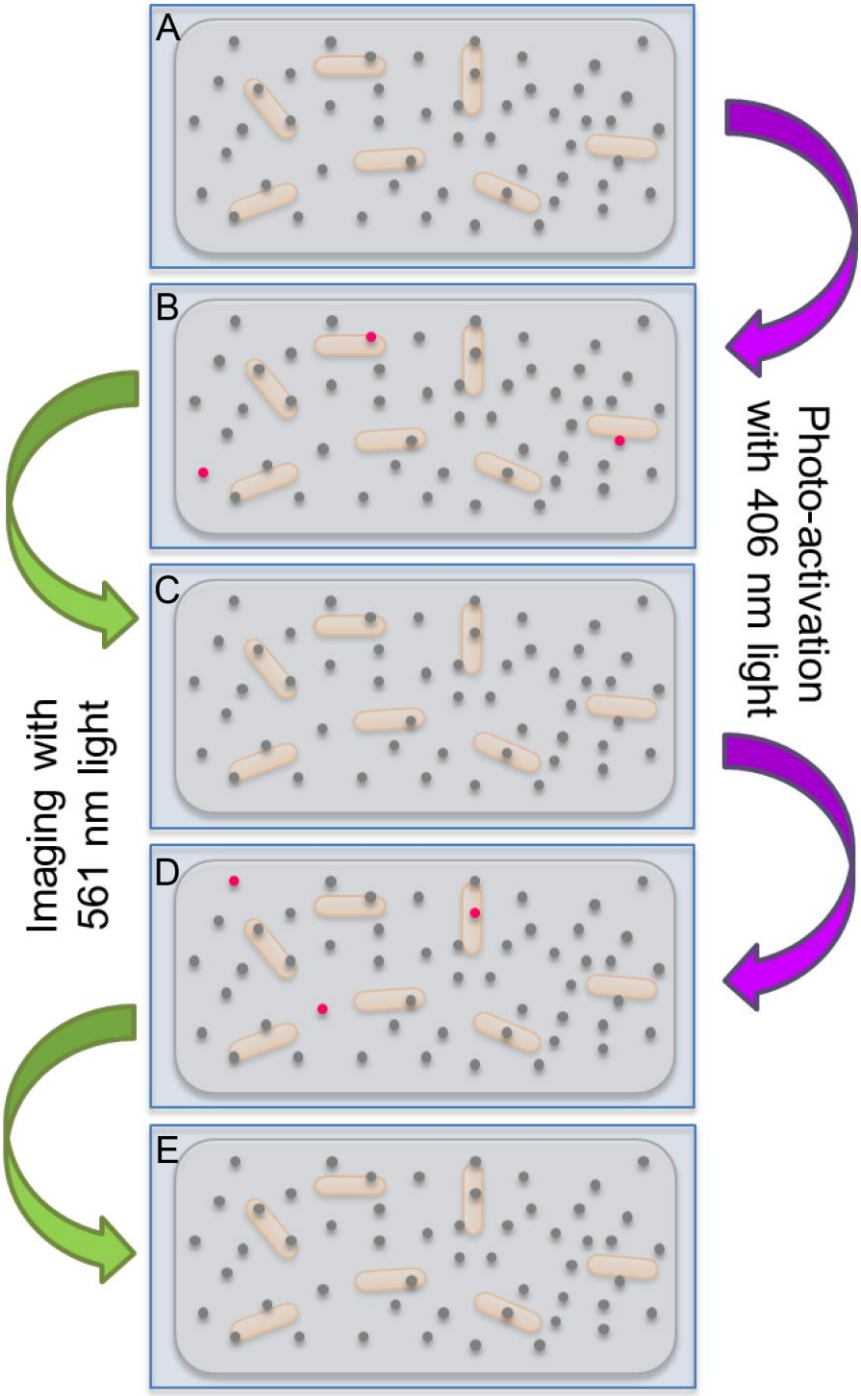

Figure 2-9. Schematic of PALM imaging detection of PAmCherry fluorescent proteins densely coated on gold NR substrates. (a) Initially all of the PAmCherry molecules are dark (gray dots). A 406-nm laser pulse photo-activates (b) a sparse subset of PAmCherry (pink dots). The photo-activated PAmCherry is imaged with 561-nm laser excitation until (c) all PAmCherry molecules bleach. (d-e) The photo-activation and imaging/photo-bleaching cycle is repeated until all PAmCherry molecules have been characterized.

PAmCherry was chosen here because its 564-nm excitation maximum and 595-nm emission maximum[5] are very similar to those of mCherry (Figure 2-4a). We therefore expect mCherry and PAmCherry to couple to gold NRs in a similar way.

The total number of photons detected from PAmCherry molecules near gold NRs and off gold NRs ("on-NR" and "off-NR", respectively) is compared in Figure 2-10a. Coupling to gold NRs increases the total number of photons detected from each PAmCherry molecule: on average, 2000 total counts are detected from immobilized PAmCherry FPs detected in the on-NR region, while an average of only 660 total counts are detected from PAmCherry FPs off-NR. In other words, FPs coupled to the gold NR near-field emit on average three times more photons prior to photobleaching than uncoupled FPs. Furthermore, the tail of the histogram (inset to Figure 1-10a) shows that there is an increase in the number of significantly enhanced PAmCherry molecules on gold. This is reflected in a broader distribution (standard deviation on-NR = 4233 vs. standard deviation off-NR = 1625). Figure 2-10b shows representative intensity time traces plotted for single PAmCherry FPs on-NR and off-NR (red and black curves, respectively); the raw epifluorescence images of these molecules are shown in Figure 2-10c. The intensity of this particular on-NR trace is nearly double that of the off-NR trace, and the emission lasts more than three times longer, yielding a significant enhancement in total detected photons: the integral of the on-NR curve in Figure 2-10b is 6.9 times larger than the off-NR integral. Clearly, through coupling, both the brightness and photostability of PAmCherry FPs is improved.

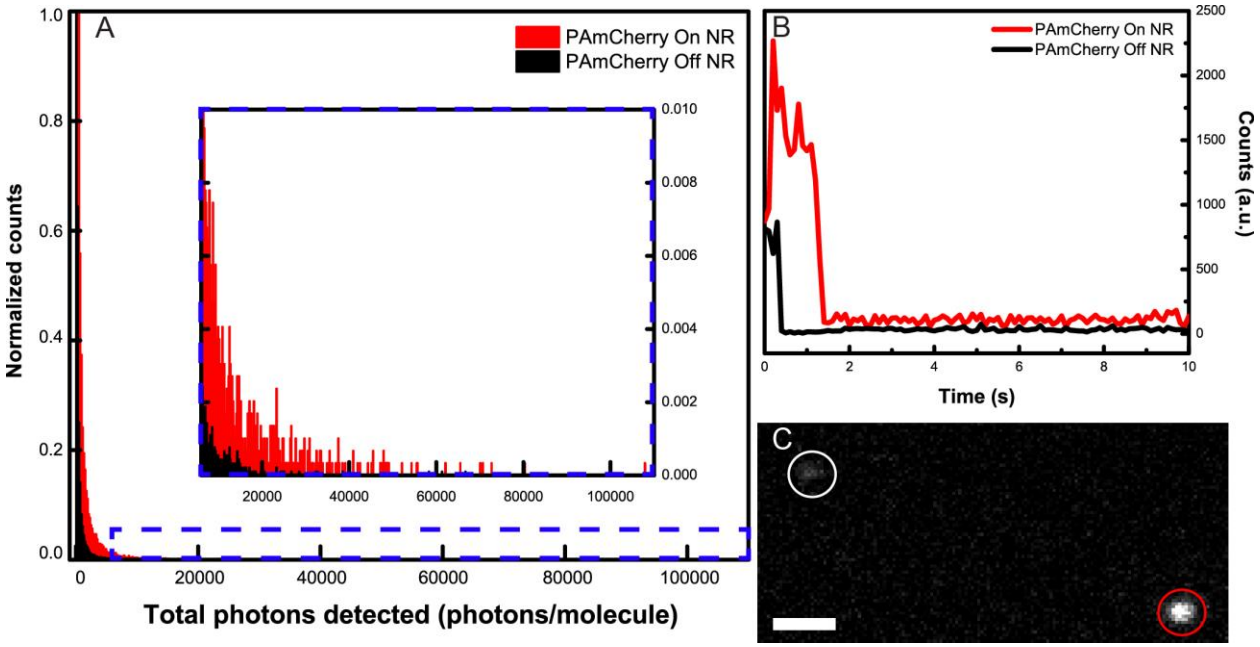

Figure 2-10. (a) Comparison of total photons detected for single, immobilized PAmCherry molecules on gold NRs (red) and off gold NRs (black). Inset: zoomed view of the tail region indicated by the blue dashed line. (b) Intensity time traces plotted for representative PAmCherry molecules on and off gold NRs (red and black curves, respectively). (c) Epifluorescence images off NR (white circle) and on NR (red circle) of the PAmCherry molecules in (b). Scale bar: 1 μm. Statistics for the total number of localizations per PALM experiment available in Table 1.2..

Table 2.2 Number of localizations for PAINT and PALM experiments

FP	Experiment type	Excitation λ (nm)	Total number of localizations
mCherry	PAINT	561	4533
mCitrine	PAINT	488	7285
mCitrine	PAINT	514	31043
PAmCherry	PALM	561	35514

2.5 Conclusions

In this chapter, we have demonstrated the enhancement of fluorescent protein (FP) emission upon coupling to the local surface plasmon resonance modes of gold NRs. Through single-molecule PAINT measurements, we have determined that the photon emission rate of mCherry FPs is more than doubled upon resonant coupling to the NR longitudinal mode. Furthermore, through super-resolution imaging (PALM), we have measured the emission of 1.5 times more total photons from immobilized PAmCherry FPs coupled to gold NRs due to increased brightness and photostability. Ultimately, the plasmon-enhancement of red FP emission improves the localization precisions of single-molecule fits to 18 nm. Interestingly, in our experiments, enhanced emission rates and improved localization precisions are not observed for mCitrine coupled to the weaker NR transverse mode, and indeed sometimes quenching is observed. These results show that the emissivity of coupled FP-NR systems is strongly dependent on plasmon mode strength and on the excitation wavelength, and therefore, careful tuning of experimental conditions is needed for future imaging applications.

Our work also highlights the utility of single-molecule super-resolution imaging for studying plasmonic coupling between FPs and NRs, as this experimental technique allows us to directly correlate enhanced emission with the NR position at the nanometer scale and observe the NRs behaving as optical antennas. Because this antenna effect shifts the apparent emission position of coupled FPs away from the real dye location, further investigation is needed to decouple the apparent emission position from the actual dye position. Our understanding of the near-field interaction of FPs and gold NRs in the context of single-molecule biological imaging would also be enhanced by measurements of single-molecule decay rates and spectra. Still, the present experiments show that longer single FP trajectories are immediately attainable, that gold NRs show great promise for improving single-molecule imaging of FPs, and that plasmon-enhanced fluorescence is sufficiently robust to be realized in situations where precise control over fluorophore position and orientation is impossible, such as in biological imaging.

2.6 Future directions

We anticipate that plasmon-enhanced FP emission will find important applications in live-cell imaging, where enhanced photostabilities will lead to longer trajectories, and that brighter probes will increase the sensitivity of single-molecule measurements, allowing, for example, photobleaching steps and stoichiometries to be counted *in vivo*. Furthermore, colloidal NRs can be assembled on a microscope coverslip as an extended array of nanoparticles,[51-55] creating an extracellular imaging substrate that could enhance emission from FP-labeled membrane-bound proteins inside live cells, as this geometry would naturally position membrane proteins in the plasmonic near-field (5-50 nm) where enhancement is possible. Other substrate geometries that integrate bio-imaging and

nanoplasmonics have also been studied,[56,57] highlighting the power of plasmonic substrates as external platforms for bio-imaging applications, and our observation of enhanced emission from plasmon-coupled FPs indicate that FPs can be improved in any of these achievable geometries. Ultimately, the results of this chapter indicate that plasmonic substrates are advantageous for super-resolution imaging, and that plasmon-enhanced fluorescence is a promising technique for improving resolution in live-cell single-molecule imaging.

References

1. Moerner, W. E.; Fromm, D. P. Methods of Single-Molecule Fluorescence Spectroscopy and Microscopy. *Rev. Sci. Instrum.* **2003**, *74*, 3597-3619.

2. Thompson, R. E.; Larson, D. R.; Webb, W. W. Precise Nanometer Localization Analysis for Individual Fluorescent Probes. *Biophys. J.* **2002**, *82*, 2775-2783.

3. Yildiz, A.; Forkey, J. N.; McKinner, S. A.; Ha, T.; Goldman, Y. E.; Selvin, P. R. Myosin V Walks Hand-over-hand: Single Fluorophore Imaging with 1.5-nm Localization. *Science* **2003**, *300*, 2061-2065.

4. Giepmans, B. N. G.; Adams, S. R.; Ellisman, M. H.; Tsien, R. Y. The Fluorescent Toolbox for Assessing Protein Location and Function. *Science* **2006**, *312*, 217-224.

5. Subach, F. V.; Patterson, G. H.; Manley, S.; Gillette, J. M.; Lippincott-Schwartz, J.; Verkhusha, V. V. Photoactivatable mCherry for High-Resolution Two-Color Fluorescence Microscopy. *Nat. Methods* **2009**, *6,* 153-159.

6. Betzig, E.; Patterson, G. H.; Sougrat, R.; Lindwasser, O. W.; Olenych, S.; Bonifacino, J. S.; Davidson, M. W.; Lippincott-Schwartz, J.; Hess, H. F. Imaging Intracellular Fluorescent Proteins at Nanometer Resolution. *Science* **2006**, *313,* 1642-1645.

7. Hess, S. T.; Girirajan, T. P. K.; Mason, M. D. Ultra-High Resolution Imaging by Fluorescence Photoactivation Localization Microscopy. *Biophys. J.* **2006**, *91*, 4258-4272.

8. Rust, M. J.; Bates, M.; Zhuang, X. Sub-Diffraction-Limit Imaging by Stochastic Optical Reconstruction Microscopy (STORM). *Nat. Methods* **2006**, *3*, 793-795.

9. Drobizhev, M.; Makarov, N. S.; Tillo, S. E.; Hughes, T. E.; Rebane, A. Two-Photon Absorption Properties of Fluorescent Proteins. *Nat. Methods* **2011**, *8,* 393-399.

10. Willets, K. A.; Nishimura, S. Y.; Schuck, P. J.; Twieg, R. J.; Moerner, W. E. Nonlinear Optical Chromophores as Nanoscale Emitters for Single-Molecule Spectroscopy. *Acc. Chem. Res.* **2005**, *38,* 549-556.

11. Kubitscheck, U.; Kueckmann, O.; Kues, T.; Peters, R. Imaging and Tracking of Single GFP Molecules in Solution. *Biophys. J.* **2000**, *78*, 2170-2179.

12. Qian, H.; Sheetz, M. P.; Elson, E. L. Single Particle Tracking. Analysis of Diffusion and Flow in Two-Dimensional Systems. *Biophys. J.* **1991**, *60,* 910-921.

13. Heim, R.; Tsien, R. Y. Engineering Green Fluorescent Protein for Improved Brightness, Longer Wavelengths and Fluorescence Resonance Energy Transfer. *Curr. Biol.* **1996**, *6,* 178-182.

14. Shaner, N. C.; Campbell, R. E.; Steinbach, P. A.; Giepmans, B. N. G.; Palmer, A. E.; Tsien, R. Y. Improved Monomeric Red, Orange and Yellow Fluorescent Proteins Derived from Discosoma sp. Red Fluorescent Protein. *Nat. Biotechnol.* **2004***, 22,* 1567-1572.

15. Biteen, J. S.; Thompson, M. A.; Tselentis, N. K.; Bowman, G. R.; Shapiro, L.; Moerner, W. E. Super-Resolution Imaging in Live *Caulobacter crescentus*cells Using Photoswitchable EYFP. *Nat. Methods* **2008***, 5,* 947-949.

16. Bates, M.; Huang, B.; Dempsey, G. T.; Zhuang, X. Multicolor Super-Resolution Imaging with Photo-switchable Fluorescent Probes. *Science* **2007**, *317*, 1749-1753.

17. Willets, K. A.; Van Duyne, R. P. Localized Surface Plasmon Resonance Spectroscopy and Sensing. *Annu. Rev. Phys. Chem.* **2007**, *58*, 267-297.

18. Anger, P.; Bharadwaj, P.; Novotny, L. Enhancement and Quenching of Single-Molecule Fluorescence. *Phys. Rev. Lett.* **2006**, *96*, 113002.

19. Lakowicz, J. R.; Fu, Y. Modification of Single Molecule Fluorescence Near Metallic Nanostructures. *Laser Photon. Rev.* **2009***, 96,* 221-232.

20. Biteen, J. S.; Pacifici, D.; Lewis, N. S.; Atwater, H. A. Enhanced Radiative Emission Rate and Quantum Efficiency in Coupled Silicon Nanocrystal-Nanostructured Gold Emitters. *Nano Lett.* **2005**, *5*, 1768-1773.

21. Tchebotareva, A. L.; de Dood, M. J. A.; Biteen, J. S.; Atwater, H. A.; Polman, A. Quenching of Si Nanocrystal Photoluminescence by Doping with Gold or Phosphorus. *J Lumin* **2005**, I, 137-144.

22. Aslan, K.; Gryczynski, I.; Malicka, J.; Matveeva, E.; Lakowicz, J. R.; Geddes, C. D. Metal-Enhanced Fluorescence: An Emerging Tool in Biotechnology. *Curr. Opin. Biotechnol.* **2005***, 16,* 55-62.

23. Giannini, V.; Fernandez-Dominguez, A. I.; Heck, S. C.; Maier, S. A. Plasmonic Nanoantennas: Fundamentals and Their Use in Controlling the Radiative Properties of Nanoemitters. *Chem. Rev.* **2011***, 11,* 3888-3912.

24. Lakowicz, J. Radiative Decay Engineering: Biophysical and Biomedical Applications. *Anal. Biochem.* **2001***, 11,* 1-24.

25. Lakowicz, J. R.; Malicka, J.; Gryczynski, I.; Gryczynski, Z.; Geddes, C. D. Radiative Decay Engineering: The Role of Photonic Mode Density in Biotechnology. *J. Phys. D Appl. Phys.* **2003**, *36*, R240-R249.

26. Lakowicz, J. Radiative decay engineering 3. Surface Plasmon-Coupled Directional Emission. *Anal. Biochem.* **2004***, 324,* 153-169.

27. Lakowicz, J. R. Radiative Decay Engineering 5: Metal-Enhanced Fluorescence and Plasmon Emission. *Anal. Biochem.* **2005***, 337,* 171-194.

28. Lakowicz, J. R. Plasmonics in Biology and Plasmon-Controlled Fluorescence. *Plasmonics* **2006***, 337,* 5-33.

29. Zhang, J.; Lakowicz, J. R. Metal-Enhanced Fluorescence of an Organic Fluorophore Using Gold Particles. *Opt. Express* **2007***, 15,* 2598-2606.

30. Lakowicz, J. R.; Fu, Y. Modification of Single Molecule Fluorescence Near Metallic Nanostructures. *Laser Photon. Rev.* **2009***, 3,* 221-232.

31. Tam, F.; Goodrich, G. P.; Johnson, B. R.; Halas, N. J. Plasmonic Enhancement of Molecular Fluorescence. *Nano Lett.* **2007**, *7*, 496-501.

32. Fort, E.; Gresillon, S. Surface Enhanced Fluorescence. *J. Phys. D Appl. Phys.* **2007***, 41,* 013001.

33. Bardhan, R.; Grady, N. K.; Cole, J. R.; Joshi, A.; Halas, N. J. Fluorescence Enhancement by Au Nanostructures: Nanoshells and Nanorods. *ACS Nano* **2009***, 3,* 744-752.

34. Schuller, J. A.; Barnard, E. S.; Cai, W.; Jun, Y. C.; White, J. S.; Brongersma, M. L. Plasmonics for Extreme Light Concentration and Manipulation. *Nature* **2010***, 9,* 193-204.

35. Langguth, L.; Punj, D.; Wenger, J.; Koenderink, A. F. Plasmonic Band Structure Controls Single Molecule Fluorescence. *ACS Nano* **2013**, *7*, 8840-8848.

36. Chattoraj, M.; King, B. A.; Bublitz, G. U.; Boxer, S. G. Ultra-Fast Excited State Dynamics in Green Fluorescent Protein: Multiple States and Proton Transfer. *Proc. Natl. Acad. Sci. U. S. A.* **1996**, *93*, 8362-8367.

37. Niwa, H.; Inouye, S.; Hirano, T.; Matsuno, T.; Kojima, S.; Kubota, M.; Ohashi, M.; Tsuji, F. I. Chemical Nature of the Light Emitter of the Aequorea Green Fluorescent Protein. *Proc. Natl. Acad. Sci. U. S. A.* **1996**, *93*, 13617-13622.

38. Weber, W.; Helms, V.; McCammon, J. A.; Langhoff, P. W. Shedding Light on the Dark and Weakly Fluorescent States of Green Fluorescent Protein. *Proc. Natl. Acad. Sci. U. S. A.* **1999**, *96*, 6177-6182.

39. Meech, S. R. Excited State Reactions in Fluorescent Proteins. *Chem. Soc. Rev.* **2009**, *38*, 2922-2934.

40. Chiarelli, P. A.; Johal, M. S.; Holmes, D. J.; Casson, J. L.; Robinson, J. M.; Wang, H. Polyelectrolyte Spin-Assembly. *Langmuir* **2002***, 18,* 168-173.

41. Sharonov, A.; Hochstrasser, R. M. Wide-Field Subdiffraction Imaging by Accumulated Binding of Diffusing Probes. *Proc. Natl. Acad. Sci. U. S. A.* **2006**, *103*, 18911-18916.

42. Tcherniak, A.; Dominguez-Medina, S.; Chang, W.; Swanglap, P.; Slaughter, L. S.; Landes, C. F.; Link, S. One-Photon Plasmon Luminescence and Its Application to Correlation Spectroscopy as a Probe for Rotational and Translational Dynamics of Gold Nanorods. *J. Phys. Chem. C* **2011***, 115,* 15938-15949.

43. Lu, G.; Hou, L.; Zhang, T.; Liu, J.; Shen, H.; Luo, C.; Gong, Q. Plasmonic Sensing via Photoluminescence of Individual Gold Nanorod. *J. Phys. Chem. C* **2012***, 116,* 25509-25516.

44. Chance, R. R.; Prock, A.; Silbey, R. J. Molecular Fluorescence and Energy Transfer Near Interfaces. *Adv. Chem. Phys.* **1978**, *37*, 1-65.

45. Ming, T.; Zhao, L.; Yang, Z.; Chen, H.; Sun, L.; Wang, J.; Yan, C. Strong Polarization Dependence of Plasmon-Enhanced Fluorescence on Single Gold Nanorods. *Nano Lett.* **2009***, 11,* 3896-3903.

46. Fu, Y.; Zhang, J.; Lakowicz, J. R. Plasmon-Enhanced Fluorescence from Single Fluorophores End-Linked to Gold Nanorods. *J. Am. Chem. Soc.* **2010***, 132,* 5540-5541.

47. Lu, G.; Zhang, T.; Li, W.; Hou, L.; Liu, J.; Gong, Q. Single-Molecule Spontaneous Emission in the Vicinity of an Individual Gold Nanorod. *J. Phys. Chem. C* **2011***, 115,* 15822-15828.

48. Knight, M. W.; Liu, L.; Wang, Y.; Brown, L.; Mukherjee, S.; King, N. S.; Everitt, H. O.; Nordlander, P.; Halas, N. J. Aluminum Plasmonic Nanoantennas. *J. Phys. Chem. B* **2012***, 11,* 6000-6004.

49. Taminiau, T. H.; Stefani, F. D.; Segerink, F. B.; van Hulst, N. Optical Antennas Direct Single-Molecule Emission. *Nat. Phot.* **2008**, *2*, 234-237.

50. Subach, F. V.; Malashkevich, V. N.; Zencheck, W. D.; Xiao, H.; Filonov, G. S.; Almo, S. C.; Verkhusha, V. V. Photoactivation Mechanism of PAmCherry Based on Crystal Structures of the Protein in the Dark and Fluorescent States. *Proc. Natl. Acad. Sci. U. S. A.* **2009***, 106,* 21097-21102.

51. Vial, S.; Pastoriza-Santos, I.; P'erez-Juste, J.; Liz-Marzan, L. M. Plasmon Coupling in Layer-by-Layer Assembled Gold Nanorod Films. *Langmuir* **2007***, 23,* 4606-4611.

52. Park, H.; Agarwal, A.; Kotov, N. A.; Lavrentovich, O. D. Controllable Side-by-Side and End-to-End Assembly of Au Nanorods by Lyotropic Chromonic Materials. *Langmuir* **2008***, 24,* 13833-13837.

53. Huang, H.; Tang, C.; Zeng, Y.; Yu, X.; Liao, B.; Xia, X.; Yi, P.; Chu, P. K. Label-Free Optical Biosensor Based on Localized Surface Plasmon Resonance of Immobilized Gold Nanorods. *Colloids Surf. B* **2009***, 71,* 96-101.

54. Alvarez-Puebla, R. A.; Agarwal, A.; Manna, P.; Khanal, B. P.; Aldeanueva-Potel, P.; Carbo-Argibay, E.; Pazos-Perez, N.; Vigderman, L.; Zubarev, E. R.; Kotov, N. A.; Liz-Marzan, L. M. Gold Nanorods 3D-Supercrystals as Surface Enhanced Raman Scattering Spectroscopy Substrates for the Rapid Detection of Scrambled Prions. *Proc. Natl. Acad. Sci. U. S. A.* **2011***, 108,* 8157-8161.

55. Donehue, J. E.; Haas, B. L.; Wertz, E.; Talicska, C. N.; Biteen, J. S. Plasmon-Enhanced Emission from Single Fluorescent Proteins. *SPIE Proc.* **2013**, *8597*, 85970J.

56. Levene, M. J.; Korlach, J.; Turner, S. W.; Foquet, M.; Craighead, H. G.; Webb, W. W. Zero-Mode Waveguides for Single-Molecule Analysis at High Concentrations. *Science* **2003**, *299*, 682-686.

57. Lohmüller, T.; Triffo, S.; O'Donoghue, G. P.; Xu, Q.; Coyle, M. P.; Groves, J. T. Supported Membranes Embedded with Fixed Arrays of Gold Nanoparticles. *Nano Lett.* **2011***, 11,* 4912-4918.

58. Scott Gradia Lab; University of California, Berkeley.

59. Liao, Y; Yang, S. K.; Koh, K.; Matzger, A. J.; Biteen, J. S. Heterogeneous Single-Molecule Diffusion in One-, Two-, and Three-Dimensional Microporous Coordination Polymers: Directional, Trapped, and Immobile Guests. *Nano Lett.* **2012**, *12*, 3080-3085.

Chapter 3 Imaging Plasmon-Enhanced Fluorescence from Single Membrane-Bound Proteins Inside *Vibrio cholerae* Cells[ǂ]

ǂ *This work was done in collaboration with Beth L. Haas, who developed cell growth protocols and who had previously characterized the TcpP virulence pathway for uncoupled cells.*

3.1 Introduction

Bacteria play important roles in everyday life, ranging from beneficial functions like yogurt production[1] and the support of human digestion[2] to harmful effects like infection. Nonetheless, until recently, the biophysics of the subcellular machinery of these small organisms was something of a mystery. Their lack of inner membrane-bound organelles caused many to believe bacteria also lacked internal organization or any high-order complexity.[3] Recent work, however, has revealed that bacteria have a very complex subcellular organization that exists in a controlled yet dynamic state, and that this organization is highly responsive to both internal and external perturbations.[3,4]

Unfortunately, studying the complex inner workings of bacteria is difficult because these cells are very small: intracellular dynamics generally take place on a scale of tens of nanometers. Fluorescence microscopy is known to be compatible with live-cell imaging,[5] but conventional methods are limited to a scale of ~300 nm,[6] and thus the small details of bacteria cells can be obscured by the diffraction of light. Electron microscopy offers higher resolution, but this high-vacuum technique requires invasive steps to prepare

samples for imaging, such as fixation, dehydration, and thin sectioning. These preparation steps are perturbative and can lead to sample artifacts, such as shrunken or altered structures.[7] Additionally, because electron microscopy must be performed under vacuum, it is not compatible with live cells.[7,8]

Beyond these difficulties localizing macromolecules on the cellular scale, the limited resolution of conventional fluorescence microscopy makes it difficult to accurately track single bacterial proteins or to observe pairs of proteins interacting. This limitation ultimately prevents accurate calculations of diffusion properties, and also precludes the accurate colocalization of proteins, both of which are important for characterizing the intracellular environment.[4,7,9]

Single-molecule fluorescence (SMF) microscopy was developed to extend conventional microscopy down to resolutions much better than 300 nm.[6] This technique takes advantage of the fact that a single emitter can be localized with a precision much better than the diffraction limit of light if a sufficient number of photons are collected. Indeed, *in vitro* implementations of SMF have yielded 1.5-nm localization precisions,[10] and theoretically, there is no limit to the achievable resolution, provided that enough photons are detected.[7,11] Therefore, to maximize resolution, the background noise must be minimized, while the photon output of the fluorophore must be maximized.[11] Additionally, to improve tracking, it is important to maximize the number of photons that can be collected per frame (i.e., per unit of time). In live bacteria, however, the number of detected photons is limited by higher background noise due to cellular autofluorescence, as well by as the fluorophores used for imaging—generally fluorescent proteins (FPs). FPs are widely used because they are genetically encodable, resulting in specific linkages

to cellular proteins, but they are also much dimmer and less photostable than organic dyes. Ultimately, fewer photons are detected from FP labels and the resolution for imaging single molecules inside live cells is currently limited to 10-40 nm.[12,13]

Plasmon-enhanced fluorescence is therefore uniquely suited to improving the localization precision and tracking capabilities of SMF imaging. Coupling to the enhanced fields of resonantly excited NPs leads to brighter and more photostable fluorescent proteins,[14] improving achievable *in vivo* localization precisions and increasing average trajectory lengths. Furthermore, brighter fluorophores allow samples to be imaged with faster frame rates without sacrificing signal to background noise.

The enhanced local field of a plasmonic nanoparticle decays rapidly as a function of distance from the nanoparticle surface, but strong enhancements have been observed for fluorophores within 50 nm of the nanoparticle.[15] At very small distances (< 3 nm), fluorescence quenching can occur due to an increased non-radiative decay rate and electron transfer to the metal, and so, for *in vitro* experiments, an insulating spacer layer is often used to prevent quenching.[16,17] In this Chapter, we have designed a plasmonic nanostructure-FP emitter sample geometry (Figure 3-1) where the bacterial cell envelope, which naturally houses the FP, serves as the insulating layer that separates an FP from direct contact with the gold nanoparticles. Here, bacterial cells containing FP-labeled membrane proteins[18] are mounted on top of a coverslip patterned with nanostructured gold via one of two large surface area routes: preparation of gold nanoislands using thermal evaporation and annealing[19] or patterning of a periodic nanotraingle array using nanosphere lithography (NSL).[20,21] We choose gold for its biocompatibility and resistance to oxidation, and we prepared samples in the geometry described in Figure 3-1

because this naturally positions fluorescently labeled membrane proteins within the enhanced field about the nanoparticle.

Specifically, we image proteins involved in regulating the human cholera disease inside the human pathogen *Vibrio cholerae* by preparing this bacterium on top of gold substrates. This Gram-negative bacterium has a cellular envelope that is approximately 50 nm thick,[22] and upon coupling *V. cholerae* cells to a plasmonic substrate, membrane-bound proteins inside the cell will naturally be positioned in the substrate near-field. We image the inner membrane protein TcpP, which regulates virulence via the downstream activation of cholera toxin production[23,24] and has been labeled with the photo-activatable protein PAmCherry, in live *V. cholerae* through super-resolution microscopy. After determining that the nanotriangle substrate is better suited to plasmon-enhanced single-molecule imaging than the thermally evaporated nanoisland film, we observe a 1.3× enhancement in the rate of emission for TcpP-PAmCherry molecules in cells coupled to gold nanotriangle arrays.

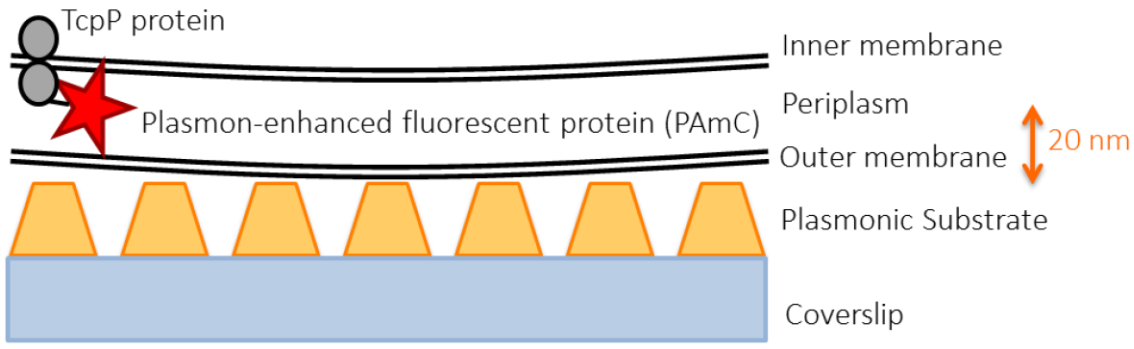

Figure 3-1. Cutaway view of *V. cholerae* cell on a plasmonic substrate. Because the cellular envelope is approximately 50 nm thick, the fluorescent protein label on the protein of interest, TcpP, can be enhanced by a nontoxic extracellular plasmonic substrate.

3.2 Experimental Methods

3.2.1 Plasmonic substrates

1.1.1.1 Gold nanoisland films

Gold nanoisland films were prepared under vacuum (5×10^{-6} Torr; Denton Vacumm SJ-20 evaporator) by thermal evaporation of 6 nm gold onto oxygen plasma-etched (10 min, 200 mTorr; PlasmaEtch PE-50) glass coverslips. The coverslips were then annealed at 400 ^{o}C for 10 min. Thin layers of gold (< 20 nm) deposited using evaporation are known to grow from nucleation points,[25] and if no wetting layer is deposited prior to the gold, annealed films form small clusters (nanoislands) on the surface of the glass.[19] After annealing, films exhibited a color change from blue to pink (Figure 3-2a), indicating the formation of nanoislands (Figure 3-2b). Gold nanoisland films were characterized by atomic force microscopy (AFM; Agilent PicoPlus 5500 Atomic Force Microscope). The AFM scans showed that the average nanoisland size was approximately 10-12 nm tall (Figure 3-2b).

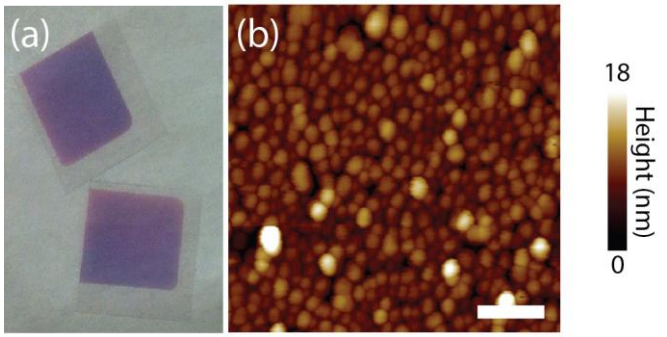

Figure 3-2. (a) Upon annealing gold films changed from blue (not shown) to pink, indicating the formation of nanoislands. (b) Tapping mode atomic force microscopy scan of annealed gold films revealed nanoislands 10-12 nm tall on average. Scale bar is 100 nm.

1.1.1.1 Gold nanotriangle arrays

Glass coverslips were coated with 100 nm ITO by sputter deposition (Kurt J Lesker Lab 18-1), then oxygen-plasma etched (10 min, 200 mTorr; PlasmaEtch PE-50). 750-nm polystyrene beads (Polyscience Polybead Microspheres) were centrifuged (10 min, 25^{o}C, 12,000×g) and resuspended in 1 mL of 95% ethanol after removal of the supernatant. The beads were again centrifuged and resuspended in fresh 95% ethanol. Beads were centrifuged one final time before the supernatant was removed and the beads were resuspended in a solution of 0.5 mL 95% ethanol and 0.5 mL 0.2mM sodium dodecyl sulfate (SDS). A 5-μL volume of the beads/SDS/ethanol mixture was pipetted onto the center of a clean, ITO-coated glass coverslip. The coverslip was held with forceps and gently shaken until the surface appeared opalescent, indicating that the beads had self-assembled into a monolayer, forming a nanosphere mask.[20,21] Coated coverslips were allowed to dry in air at room temperature overnight.

A 5-nm titanium wetting layer was evaporated (deposition rate of 1 nm/s) onto the nanosphere-coated coverslip, followed by 50 nm of gold (deposition rate of 1 nm/s) under vacuum (1×10^{-6} Torr; Denton Vacuum SJ-20 evaporator). Clear office tape was used to remove the nanosphere mask, leaving behind a periodic array of nanoscale gold triangles. Scanning electron microscopy (Hitachi SU800) was used to verify the formation of gold nanotriangles (NTs) on the coverslip surface in an ordered array approximately 150 nm on a side.

1.1.1.2 Plasmon resonance characterization

The plasmon resonance spectrum of the gold nanoisland film was characterized using UV-visible absorption spectroscopy (Hewlett Packard 8453). Dark-field scattering

spectroscopy was used to characterize the spectral response of the gold nanotriangle (NT) arrays. For this application, the NT array was excited through a dark-field oil immersion objective (NA = 0.6) by a broadband halogen light source (400-1000 nm). The sample was immersed in water, and the diffraction-limited spot of a row of NTs was aligned to the entrance slit of an imaging spectrograph (Princeton Instruments Acton SP-2300i) and dispersed on a 150 groove/mm grating. Scattering spectra were collected on a 512x512 pixel EMCCD (Andor iXon) detector. Background spectra taken from an area of the sample without the gold surface were subtracted from the measured NT scattering spectrum. The background-subtracted spectra were then divided by the detected spectrum of the halogen light source to correct for spectral efficiency of the system.

3.2.2 Bacterial samples

1.2.1.1 Bacterial cultures and sample preparation for live-cell imaging

V. cholerae O395 *ΔtcpP* TcpP-PAmCherry bacterial cultures[18] were grown overnight in LB media at 37 ^{o}C with shaking (180 rpm), then diluted into M9 minimal media with 0.4% glycerol and an amino acid supplement (asparagine, arginine, glutamic acid, and serine, 25 mM final concentration) and grown to turbidity (OD ~0.3) at 30 ^{o}C. Kanamycin (50 μg/mL final concentration) was used to select for the TcpP-PAmCherry plasmid. Arabinose (0.1% final concentration) was added cultures to induce expression of the TcpP-PAmCherry fusion protein, and cultures were incubated for an additional three hours. A 1-mL aliquot of culture was centrifuged for 30 s at 30,000×*g* to form a cell pellet. The cell pellet was washed in 1 mL of warm M9, then centrifuged once more before resuspended in ~40 μL of the supernatant. A 2-μL droplet of concentrated, washed cells was pipetted onto an agarose pad (2% agarose dissolved in M9 and spread on to a

plasma-etched coverslip) before being placed on top of the plasmonic substrate (either gold nanoisland film or NT array), with the patterned side of coverslip facing the cells (Figure 3-3). Plasmonic substrates were prepare such that each had a region where no gold was present, which served as an "off-Au" control where cells would experience imaging conditions identical to cells in "on-Au" regions.

Figure 3-3. Microscopy sample geometry. Side view is oriented for an inverted microscope setup (objective is below large, bottom coverslip).

1.1.1.3 Bacterial fixation and sample preparation

5-mL cultures of *V. cholerae* were centrifuged for 5 min at 4 ^{o}C and 4000 rpm to form a pellet. The supernatant was removed, and the cell pellet was resuspended in 5 mL of cold solution of 1% formaldehyde in M9. Cells were incubated at room temperature for 10 min, then placed on ice for either 30 min or 60 min. Samples were then centrifuged for 15 min at 4 ^{o}C and 7179×*g*. The supernatant was removed, and the pellet was resuspended in 5 mL cold M9. Centrifugation and resuspension were repeated two more times for a total of three washes. Fixed cells were kept at 4 ^{o}C for no more than two days until use, at which time a 1-mL aliquot of fixed cells was centrifuged for 5 min at 7830 rpm, then pelleted cells were resuspended in ~40 µL supernatant. A 2-µL droplet of concentrated cells was placed on to an agarose pad (2% agarose dissolved in M9 and spread onto a

plasma-etched coverslip) before being placed on top of a NT array in a manner similar to that described above in Section 3.2.2.1.

3.2.3 Super-resolution microscopy

Bacteria samples were imaged at room temperature using a wide-field epifluorescence inverted microscope (Olympus IX71) equipped with a 100× oil immersion phase-contrast objective (NA = 1.4) and a micrometer stage. A piezo objective positioner (PIFOC PD72Z1CAQ) was used for precision focusing (1-nm closed-loop resolution). Single TcpP-PAmCherry molecules were photo-activated using short pulses (50-70 ms) of circularly polarized 405-nm laser light (Coherent Cube 405 and Tower Optical .250-405 quarter waveplate, excitation power of 0.1025 W/mm^2), and subsequently excited and imaged using filtered, circularly polarized 561-nm laser light (Coherent Sapphire 561-50, Semrock LL01-561, and Tower Optical .250-556 quarter waveplate, excitation power of 2.68 W/mm^2). The activation and excitation lasers were coupled using a dichroic mirror (Semrock Di01-R405), and the fluorescence emission was filtered with appropriate dichroic and emission filters (Semrock Di01-R561 and BLP01-561, respectively). A pair of shutters (Uniblitz) was used to control the laser beams such that the sample was exposed to one laser beam at a time. To image all of the TcpP-PAmCherry molecules one at a time, cells were exposed to cycles of 50-70 ms 405-nm activation pulses and 60-70 s of 561-nm imaging light over the course of 7-10 min of data collection per movie. Emission was detected on a 512×512 pixel Photometrics Evolve EMCCD (each pixel 49×49 nm) using a 40-ms integration time (25 frames per second). Cellular positions were determined on gold nanoisland films using bright field imaging and phase-contrast imaging was used for determining cell positions on gold NT arrays. In bright-field

imaging, the sample is illuminated using white light and contrast in the sample is due to the absorbance of some of the transmitted light. In phase-contrast imaging, phase shifts in light passing through the sample are used to change brightness in the image and create contrast.

3.2.4 Background fluorescence subtraction

Background fluorescence due to gold scatter was subtracted from the raw data by subtracting the average of every 50-frame movie segment from each frame in the 50-frame segment. Background-subtracted data were used for all further analysis.

3.2.5 Data analysis

Emission intensities, molecular positions and counts detected per frame were extracted from the data by least-squares fitting of background-subtracted signal intensity to a 2D Gaussian function with the MATLAB routine *nlinfit*. When mapping molecular positions in PAINT experiments, each observed adsorption event is plotted as a colored spot at the center position of the emission pattern, as determined by average localization precisions that were determined using the 95% confidence interval.

3.3 Results and Discussion

3.3.1 Gold nanoisland films

UV-vis absorbance revealed that the gold nanoisland films have a plasmon resonance around 558 nm (Figure 3-4). Though the nanoisland films generally have a very broad plasmon resonance and good spectral overlap with the TcpP-PAmCherry excitation spectrum, which is similar in shape to mCherry with a peak wavelength at 564 nm,[26] several experimental issues made the films poor imaging substrates. First, under our 561-

nm excitation, the films exhibited a very high background scattering signal that fluctuated significantly during imaging. We attributed these fluctuations to charge transfer between closely spaced nanoislands. This background led to incomplete background subtraction and made it impossible to distinguish between background fluctuations and single-molecule fluorescence emission. Second, cells could not be observed in bright field on some films due to the density of nanoislands, making it impossible to confidently determine cell boundaries. Finally, because no wetting layer connected the gold nanoislands to the glass coverslip, gold easily flaked from the coverslip surface, making the samples very fragile and not reusable.

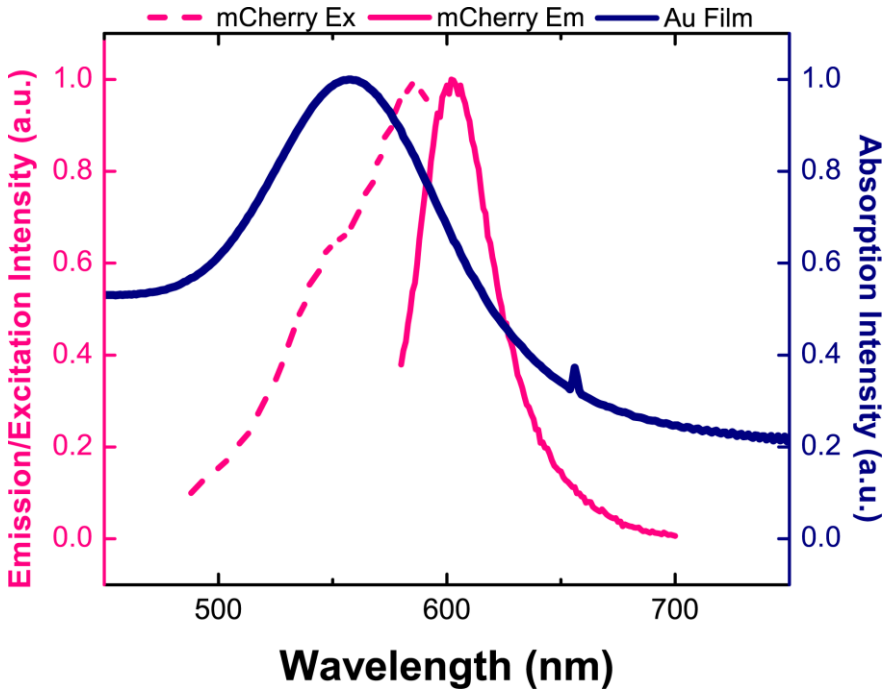

Figure 3-4. UV-visible absorption spectrum of annealed gold nanoisland film overlayed with excitation and emission spectra of mCherry, which is representative of PAmCherry. Nanoisland films generally had very broad shape and resonance maxima near 558 nm.

3.3.2 Gold nanotriangle arrays

SEM images verified the formation of gold NTs on the coverslip surface in an ordered array approximately 150 nm on a side (Figure 3-5). The periodic gold pattern was also visible using diffraction-limited phase-contrast microscopy (data not shown) and extended over the scale of several microns (Figure 3-6). Dark-field scattering measurements revealed a dominant plasmon resonance peak in the NT scattering spectrum around 600 nm, and additional resonances were observed at the red-edge of the spectrum (Figure 3-7). These modes are likely due to interactions between NTs in regions where imperfections in the polystyrene bead monolayer resulted in defects in the NT pattern.[20,21,27]

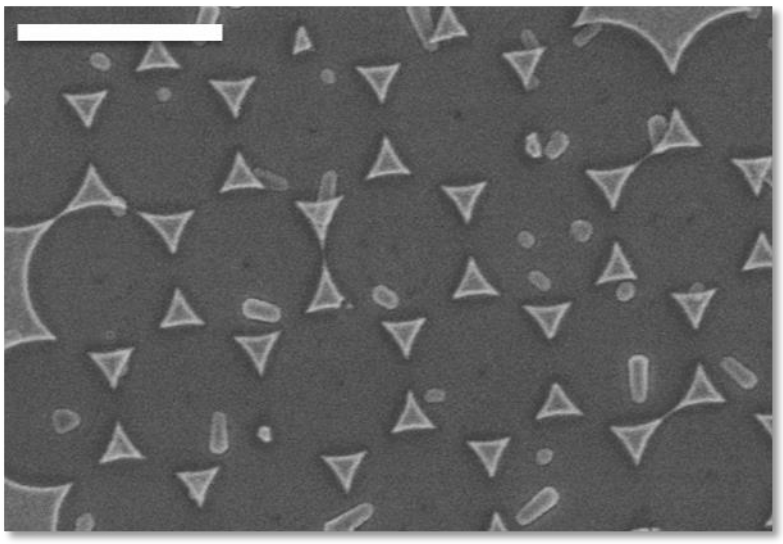

Figure 3-5. Scanning electron micrograph of gold NT array made by nanosphere lithography. A monolayer of polystyrene beads with diameters of 750 nm was used as a mask through which 5 nm of Ti and 50 nm of Au were evaporated. Beads were removed using clear office tape, leaving behind an array of nanoscale triangles. Each NT is approximately 150 nm on a side. Scale bar is 1 μm.

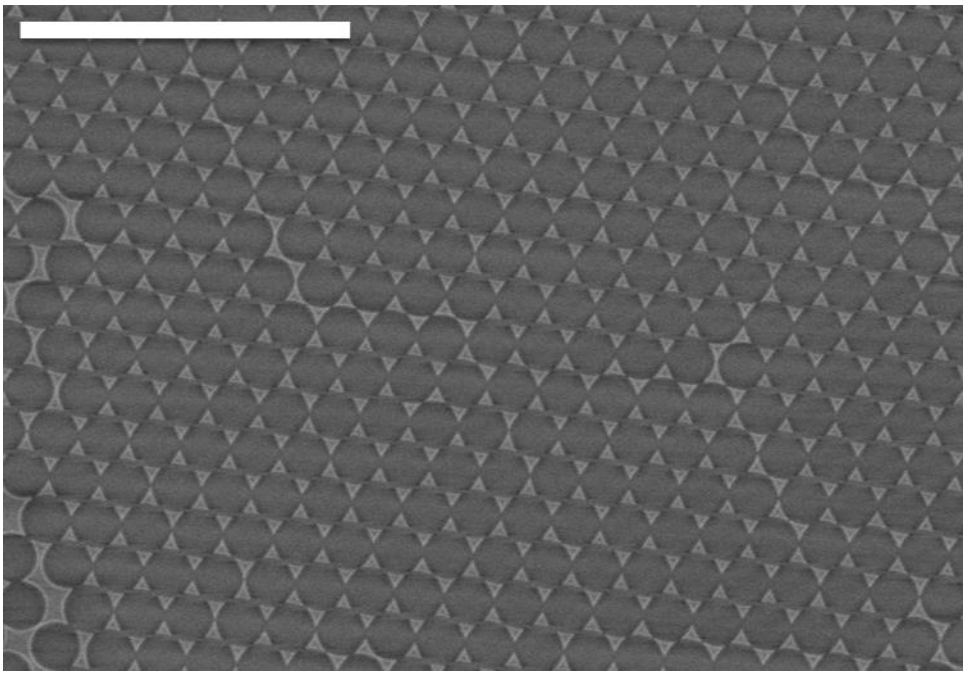

Figure 3-6. Large field-of-view scanning electron micrograph of gold nanotriangles. The pattern extends over large areas of the coverslip, allowing sufficient room for imaging live *V. cholerae* cells. Areas of bow-tie structures (two nanotriangles with touching tips) can also be seen in regions where defects in the perfect close-packed monolayer of polystyrene beads yielded an imperfect mask.[27] Scale bar is 5 μm.

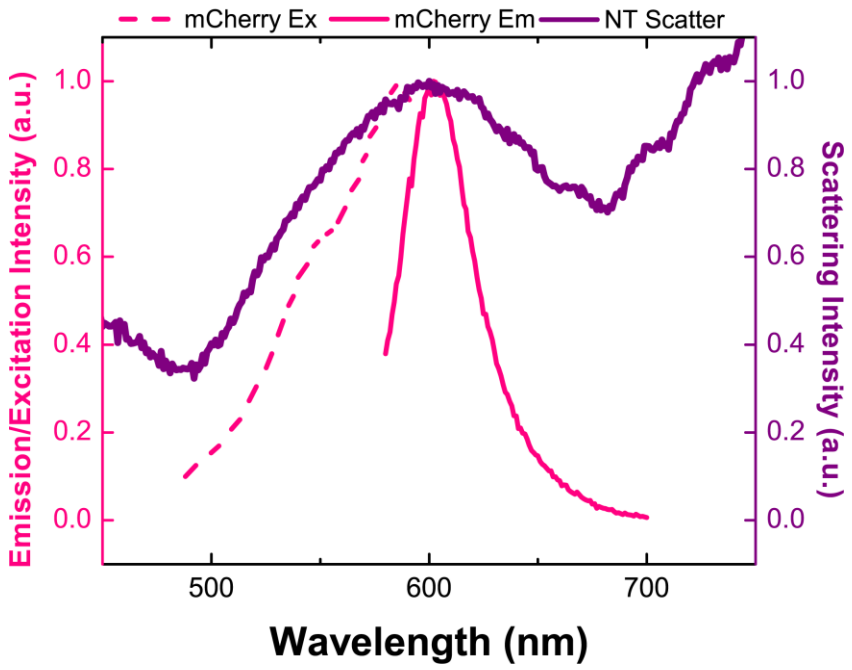

Figure 3-7. Dark-field scattering spectrum of gold nanotriangles overlayed on mCherry spectra. The dominant plasmon peak is observed near 600 nm and overlaps well with both the excitation and emission maxima for mCherry (which are representative of the PAmCherry spectra). Additional modes on the red-edge of the spectrum are likely due to interactions between nanotriangles due to defects in the nanosphere mask.

3.3.3 PAINT experiments on gold nanotriangle arrays

To benchmark the potential for plasmon-enhanced fluorescence, PAINT (Points Accumulation for Imaging in Nanoscale Topography)[28] experiments were done on the gold NT arrays using purified mCherry, in concentration and preparation similar to that described in Chapter 2. As described previously, in the PAINT super-resolution method, the stochastic adsorption events of single fluorescent molecules on a substrate surface over time are visualized on an EMCCD detector as discrete punctate spots, whereas fluorophores freely diffusing in solution (i.e., those molecules not adsorbed onto the substrate surface) are invisible because their motion is too fast to be resolved by the EMCCD (operated at a 25-Hz frame rate). For our PAINT experiments, the NT substrates

were immersed in 75 – 100 μL of 175 nM FP in PBS contained by a small rubber O-ring previously cleaned by sonication in acetone.

Figure 3-8 compares the photon detection rate of each adsorbing FP (in units of intensity/molecule/frame) for two populations: mCherry molecules adsorbed on glass (grey, subsequently referred to as "off-NT") and mCherry molecules adsorb on the gold NT array (red, subsequently referred to as "on-NT"). The average photon detection rate for the on-NT population is 41,362 counts/molecule/40 ms, while the average photon detection rate for the off-NT population is 38,547 counts/molecule/40ms. In contrast to the results in Chapter 2, we do not observe a large net fluorescence enhancement in these samples, likely due to the fact that, whereas the nanorods in Chapter 2 were enveloped into a 6-nm polymer, no insulating separation is present to prevent FPs from making direct contact to the gold NTs in this geometry. Indeed, the average photon detection rates in Figure 3-8, as well as the ensemble distributions, look very similar for the two populations, though the on-NT population shows a slight tail of higher photon detection rates indicating a small group of significantly enhanced emitters (Figure 3-8, inset).

However, when the apparent emission positions of all adsorbed fluorescent molecules are mapped out with sub-diffraction-limited resolution for the two populations (Figure 3-9), a very clear pattern emerges. In Figure 3-9, each observed adsorption event is plotted as a colored spot at the center position of the emission pattern. The dot color represents the intensity enhancement, which is determined by taking the emission intensity of the spot and dividing it by the average emission intensity of the off-NT population and is proportional to the photon detection rate for each molecule while it is adsorbed to the surface. Because of this equivalency, red spots (high intensity enhancement) represent

molecules with a high photon detection rate, while blue spots (low intensity enhancement) represent molecules with a low photon detection rate. In Figure 3-9a, the localizations of each adsorption event are plotted for the off-NT population, and a homogenous distribution of positions is observed, indicating spatial uniformity in the adsorption environment. In Figure 3-9b and 3-9c, the localizations of each adsorption event for the on-NT population are plotted. Heterogeneity in the adsorption positions is immediately apparent here. In Figure 3-9c, the adsorption positions are plotted on top of a diffraction-limited fluorescence image of the gold NT array in which white spots correspond to individual NTs. It is clear that the apparent emission positions are predominantly located along the NT edges and in the junctions between NTs. Interestingly, very few localizations are observed directly above the NTs, and those that are in fact observed at those positions are dim (blue).

Despite the fact that the adsorption environment is uniform (Figure 3-9a), the localizations of single mChery molecules map a heterogeneous emission pattern on the NT substrates. These trends would be obscured in an ensemble average and this pattern highlights the strength of single-molecule fluorescence (SMF) imaging for studying plasmonic coupling. By scanning the local environment with individual molecules, we achieved a high-resolution picture of plasmon-coupled emission. The emission pattern of the on-NT population is similar to what has been observed by others using NT arrays for confocal imaging.[29] As discussed previously, the dark-field scattering spectrum of the NT arrays (Figure 3-7) shows several plasmon resonances. Therefore, it is possible that the observed emission pattern is the result of a coupled system more complex than the isolated NRs studied in Chapter 2 or the nanoislands studied by Wertz et al.[14,30]

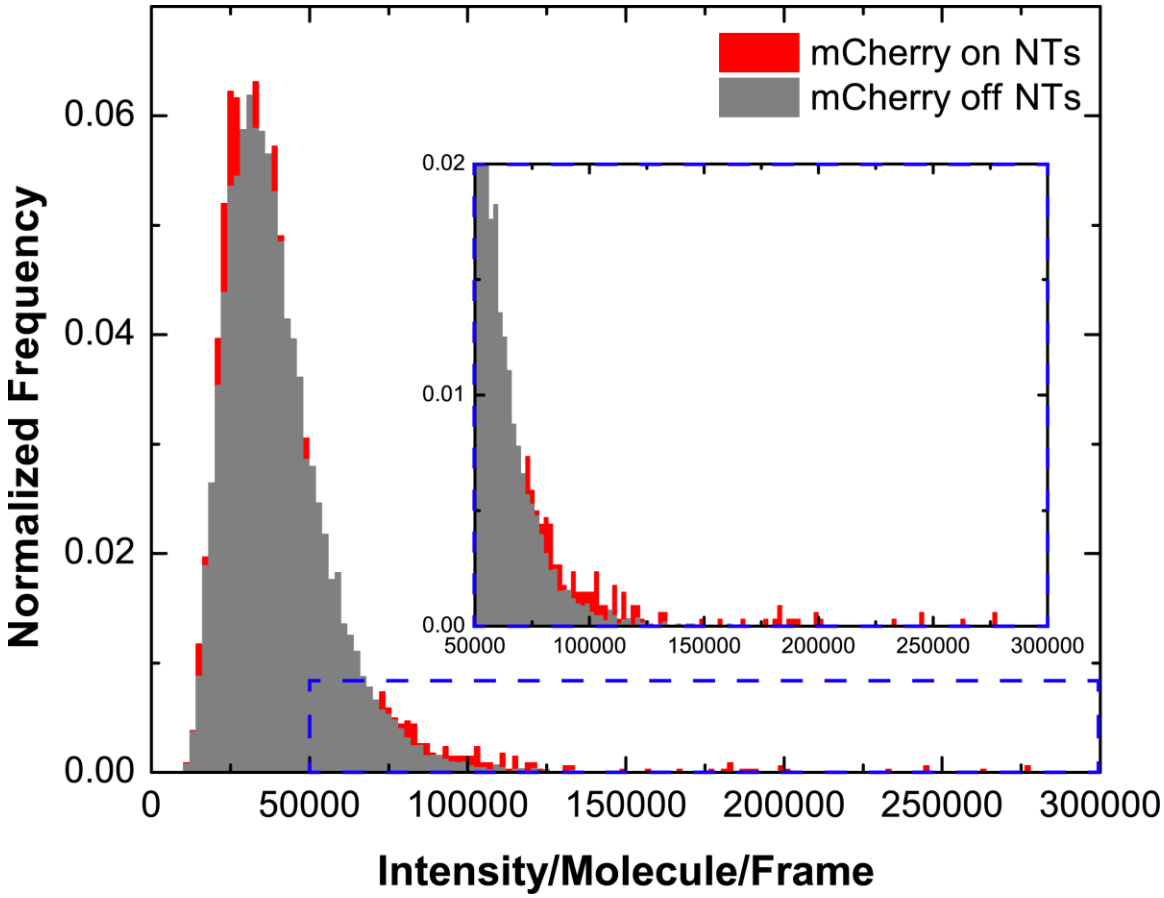

Figure 3-8. Histogram comparing the photon detection rates for mCherry molecules adsorbing on a Au nanotriangle array (on NT; red) and on a glass coverslip (off NT; grey). Average photon detection rates for the two populations are very similar (on NT = 41,362 counts/molecule/40 ms; off NT = 39, 547 counts/molecule/40 ms), though a slight tail at higher photon detection rates is seen for the on NT population (inset).

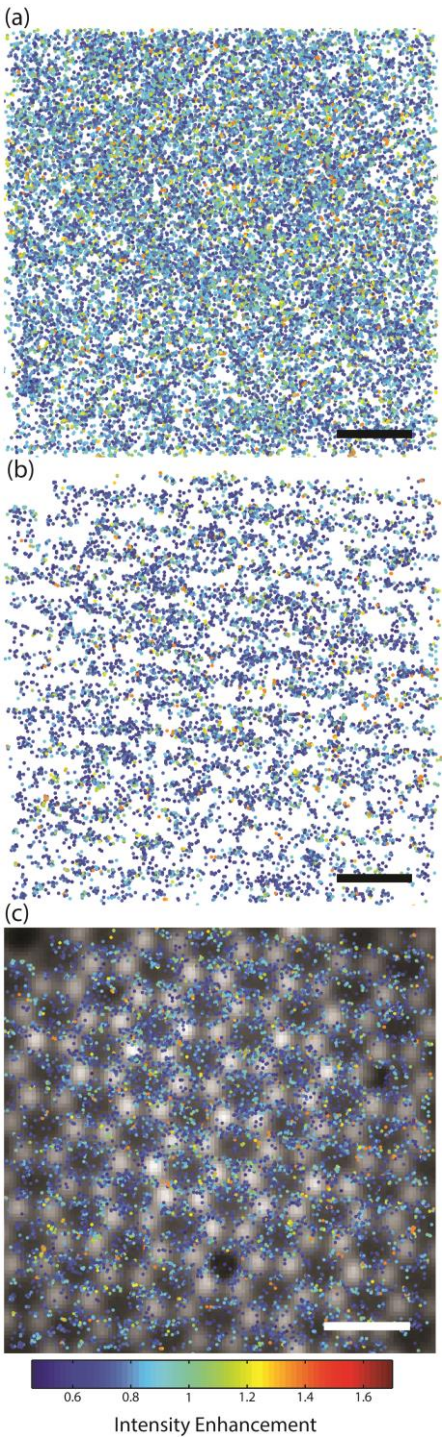

Figure 3-9. Super-resolution maps of apparent emission positions. Each dot shows the in-plane localization position of an mCherry adsorption event, and the color of the dot represents the intensity enhancement of each adsorption event. Because the intensity enhancement is proportional to the number of photons detected, red spots represent molecules with high photon detection rates, while blue spots represent molecules with low photon detection rates. (a) shows mCherry molecules off NT arrays, (b) and (c) show mCherry molecules on NT arrays. Scale bars are all 1 μm.

3.3.4 Plasmonic-enhancement of membrane-bound proteins in live *Vibrio cholerae*

Live *V. cholerae* cells were prepared on top of gold NT arrays for imaging, as described above. Figure 3-10a and 3-10b shows the phase-contrast image and fluorescence image, respectively, of the same two *V. cholerae* cells on a gold NT array. Single-molecule localizations are mapped on top of the fluorescence image in Figure 3-10b using the same color map described for the PAINT experiments (Figure 3-9). Figure 3-10c shows a zoomed-in view of the cell outlined by the red dashed box in Figures 3-10a and 3-10b. From Figure 3-10c, it is clear that the majority of the TcpP-PAmCherry localizations occur near the NT edges and that the brightest emission events (orange spots) appear to emanate from the junctions between the NTs, similar to what was observed *in vitro* with mCherry (Figure 3-9c). The similarities in the *in vitro* and *in vivo* localization patterns are particularly interesting because the *in vitro* experiments measured mCherry molecules adsorbing directly on the NT substrate while *in vivo*, the PAmCherry molecules diffuse inside the cell envelope in a plane above the NT arrays (Figure 3-1). Importantly, this similarity between the two experiments indicates that, though there is a finite (~20-nm) gap between the PAmCherry labels and the NT substrates, PAmCherry does still experience strong coupling to the plasmonic substrate. Additionally, localizations span the length of the cell, suggesting that a protein moving throughout the membrane has a high probability of diffusing through the enhanced field of a NT and as a result experiencing increased photon emission.

In Figure 3-11, the emission intensities coming from PAmCherry in cells on gold NT arrays are compared with the emission intensities from PAmCherry emanating from within cells on bare glass coverslip. A higher average photon detection rate is observed

for the population on gold NTs: 29,398 counts/molecule/40 ms compared to 21,945 counts/molecule/40 ms for the off-NT population. Importantly, this average enhancement is attributed to a second distribution in the histogram for the on-NT population: in addition to a distribution of emission intensities centered about 15,500 detected counts/molecule/40 ms (similar to the off-NT population), a second distribution of emission intensities around 50,000 counts/molecule/40 ms is present on-NT (Figure 3-11). This shoulder in the histogram represents a group of molecules that are optimally positioned within the NT enhanced field and are therefore maximally enhanced.

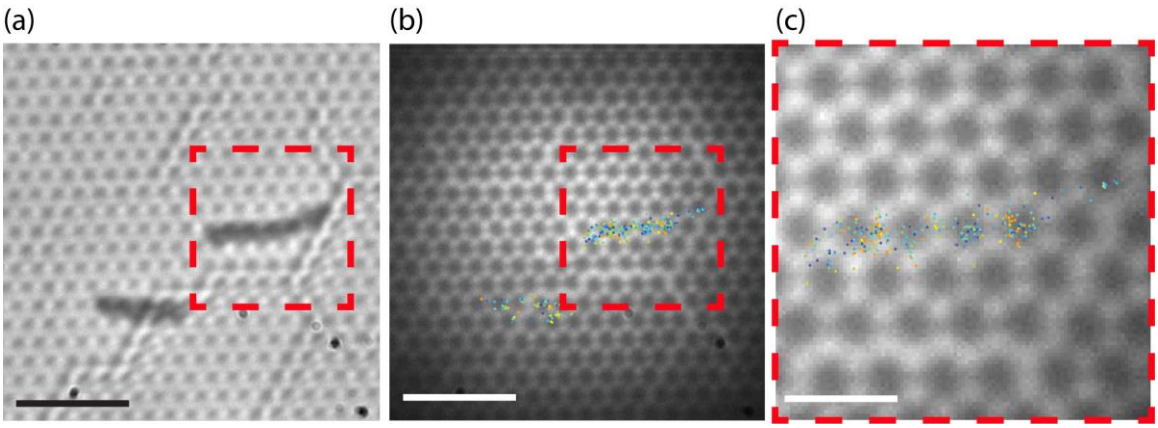

Figure 3-10.Images of live *Vibrio cholerae* on gold NT arrays. (a) Phase-contrast and (b) fluorescence images of the same two cells on NT arrays. The hexagonal NT array pattern can be seen in both images, and individual NTs are visible as bright punctate spots in (b). Cells appear as dark curved shapes in (a). Single-molecule localizations of TcpP-PAmCherry molecules are plotted as colored dots in (b). Color is correlated with photon detection rate: orange spots have high photon detection rates and blue spots have low photon detection rates. Scale bars are 4 μm. (c) shows a zoomed view of the fluorescence image with single-molecule localizations in cell outlined in red box in (a) and (b).

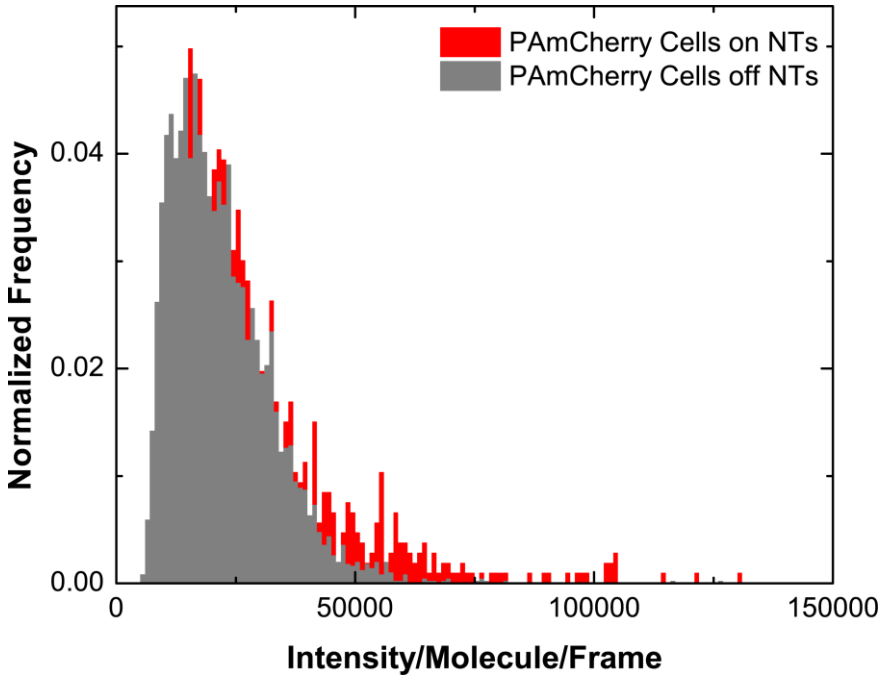

Figure 3-11. Histogram comparing the photon detection rates of membrane-bound TcpP-PAmCherry molecules inside live *Vibrio cholerae* cells on a gold nanotriangle array (red) and on a glass coverslip (grey). The cells on the gold nanotriangle array show a TcpP-PAmCherry photon detection rate that is 1.3× that of the off nanotriangle cells. A second distribution appears as a shoulder in the histogram, beginning around 50,000 counts/molecule/frame. This second distribution represents those TcpP-PAmCherry molecules that are optimally positioned within the nanotriangle near-field and show the upper-limit of achievable enhancement.

3.3.5 Plasmonic-enhancement of membrane-bound proteins in fixed *Vibrio cholerae*

Whereas the emission rate of PAmCherry was measured *in vivo* on a per-frame basis above, fixed *V. cholerae* cells containing TcpP-PAmCherry can provide a sample of stationary, photoactivatable fluorescent molecules inside cells for determining the *total* photons emitted by immobile membrane-proteins on gold NT substrates. Coupling to plasmonic substrates has been shown to increase the photostability of immobilized PAmCherry molecules *in vitro*,[14] and so, we aimed to measure a similar enhancement *in vivo*. Unfortunately, even after fixation, many fluorescent molecules appeared to diffuse

throughout the cells. The fixation protocol was changed, replacing methanol with formaldehyde due to suggestions found in literature,[31] but diffusion was still observed. The fixation protocol was further altered by increasing the time cultures were chilled in fixation solution from 30 min to 60 min. Qualitatively, the cells that were chilled for 60 min appeared to have more immobile spots, though some diffusive molecules were still observed. This fixation protocol needs to be further improved more before firm conclusions can be drawn from the data.

3.4 Conclusion and Future Directions

In this Chapter, we have developed a protocol for using patterned gold substrates to achieve plasmon-enhanced emission in live *V. cholerae* cells. We found that gold NT arrays, made using nanosphere lithography, are much better suited for SMF imaging than gold nanoisland substrates made through thermal evaporation and annealing, in particular due to a more consistent background scattering signal. We observed a 1.3× enhancement in the rate of emission for TcpP-PAmCherry molecules inside live *V. cholerae* cells on gold NTs. To date, there have only been a few examples of coupling biological sample to plasmonic substrates and these studies have mostly focused on model membranes or eukaryotic cells,[32-36] and have mainly relied on silver substrates, [33-35] which are toxic to bacterial cells. Importantly, this chapter describes the first observation of plasmon-enhanced fluorescence inside live bacterial cells and provides a foundational protocol for developing this technique for improved *in vivo* SMF imaging.

Further studies are needed to develop plasmon-enhanced fluorescence as a ubiquitous technique for improved SMF imaging. Additional experiments with live cells will allow us to further optimize imaging conditions such that maximum photon detection rates and

trajectory lengths are observed. Additional experiments with fixed cells are equally important, as these will allow us to quantify any observed photostability enhancements and to determine the maximum trajectory lengths attainable in tracking experiments. A systematic study of increased chill times for cultures in the fixation solution will be an important step in optimizing the fixation protocol and ensuring sufficient immobilization of molecules for photostability studies.

References

1. Shahani, K. M.; Chandan, R. C. Nutritional and Healthful Aspects of Cultured and Culture-Containing Dairy Foods. *J. Dairy Sci.* **1979**, *62*, 1685-1694.

2. Karunatilaka, K. S.; Cameron, E. A.; Martens, E. C.; Koropatkin, N. M.; Biteen, J. S. Super-Resolution Imaging of Live Anaerobic Bacteria: Assembly and Dynamics of a *Bacteroides* Starch Utilization System. *Submitted.* **2014**.

3. Shapiro, L.; McAdams, H. H.; Losick, R. Why and How Bacteria Localize Proteins. *Science* **2009**, *326*, 1225-1228.

4. Gahlmann, A.; Moerner, W. E. Exploring bacterial cell biology with single-molecule tracking and super-resolution imaging. *Nat. Rev. Micro.* **2014**, *12*, 9-22.

5. Wolf, D. E. Fundamentals of fluorescence and fluorescence microscopy. *Methods Cell Biol.* **2007**, *81*, 63-91.

6. Huang, B.; Babcock, H.; Zhuang, X. Breaking the diffraction barrier: super-resolution imaging of cells. *Cell* **2010**, *143*, 1047-1058.

7. Fernandez-Suarez, M.; Ting, A. Y. Fluorescent probes for super-resolution imaging in living cells. *Nat. Rev. Mol. Cell Biol.* **2008**, *9*, 929-943.

8. Biteen, J. S.; Moerner, W. E. Single-Molecule and Superresolution Imaging in Live Bacteria Cells. *Cold Spring Harb. Perspect. Biol.* **2010**, *2*, a000448.

9. Biteen, J. S. Extending the tools of single-molecule fluorescence imaging to problems in microbiology. *Mol. Microbiol.* **2012**, *85*, 1-4.

10. Yildiz, A.; Forkey, J. N.; McKinner, S. A.; Ha, T.; Goldman, Y. E.; Selvin, P. R. Myosin V walks hand-over-hand: Single fluorophore imaging with 1.5-nm localization. *Science* **2003**, *300*, 2061-2065.

11. Thompson, R. E.; Larson, D. R.; Webb, W. W. Precise nanometer localization analysis for individual fluorescent probes. *Biophys. J.* **2002**, *82*, 2775-2783.

12. Biteen, J. S.; Thompson, M. A.; Tselentis, N. K.; Bowman, G. R.; Shapiro, L.; Moerner, W. E. Super-resolution imaging in live*Caulobacter crescentus*cells using photoswitchable EYFP. *Nat. Methods* **2008**, *5*, 947-949.

13. Bates, M.; Huang, B.; Dempsey, G. T.; Zhuang, X. Multicolor super-resolution imaging with photo-switchable fluorescent probes. *Science* **2007**, *317*, 1749-1753.

14. Donehue, J. E.; Wertz, E.; Talicska, C. N.; Biteen, J. S. Plasmon-Enhanced Brightness and Photostability from Single Fluorescent Proteins Coupled to Gold Nanorods. *J. Phys. Chem. C* **2014**, *118*, 15027-15035.

15. Anger, P.; Bharadwaj, P.; Novotny, L. Enhancement and Quenching of Single-Molecule Fluorescence. *Phys. Rev. Lett.* **2006**, *96*, 113002.

16. Tchebotareva, A. L.; de Dood, M. J. A.; Biteen, J. S.; Atwater, H. A.; Polman, A. Quenching of Si Nanocrystal Photoluminescence by Doping with Gold or Phosphorus. *J Lumin* **2005**, *114*, 137-144.

17. Jose, J.; Jordan, L. R.; Johnson, T. W.; Lee, S. H.; Wittenberg, N. J.; Oh, S. Topographically Flat Substrates with Embedded Nanoplasmonic Devices for Biosensing. *Adv. Fun. Mater.* **2013**, *23*, 2812-2820.

18. Haas, B. L.; Mason J. S.; DiRita, V. J.; Biteen, J. S. Single-molecule tracking in live *Vibrio cholerae* reveals that ToxR recruits the membrane-bound virulence regulator TcpP to the *toxT* promoter. *Mol. Microbiol.* **2014**.

19. Gupta, R.; Dyer, M. J.; Weimer, W. A. Preparation and characterization of surface plasmon resonance tunable gold and silver films. *J. Appl. Phys.* **2002**, *92*, 5264.

20. Vogel, N.; Goerres, S.; Landfester, K.; Weiss, C. K. A Convenient Method to Produce Close- and Non-close-Packed Monolayers using Direct Assembly at the Air-Water Interface and Subsequent Plasma-Induced Size Reduction. *Macromol. Chem. Phys.* **2011**, *212*, 1719-1734.

21. Hulteen, J. C.; Van Duyne, R. P. Nanosphere lithography: A materials general fabrication process for periodic particle array surfaces. *J. Vac. Sci. Technol. A* **1995**, *13*, 1553-1558.

22. Graham, L. L.; Harris, R.; Villiger, W.; Beveridge, T. J. Freeze-substitution of gram-negative eubacteria: general cell morphology and envelope profiles. *J. Bacteriol.* **1991**, *173*, 1623-1633.

23. Beck, N. A.; Krukonis, E. S.; DiRita, V. J. TcpH Influences Virulence Gene Expression in *Vibrio cholerae* by Inhibiting Degradation of the Transcription Activator TcpP. *J. Bacteriol.* **2004**, *186*, 8309-8316.

24. Matson, J. S.; Withey, J. H.; DiRita, V. J. Regulatory networks controlling *Vibrio cholerae* virulence gene expression. *Infect. Immun.* **2007**, *75*, 5542-5549.

25. Warmack, R. J.; Humphrey, S. L. Observation of two surface-plasmon modes on gold particles. *Phys. Rev. B* **1986**, *34*, 2246-2252.

26. Subach, F. V.; Patterson, G. H.; Manley, S.; Gillette, J. M.; Lippincott-Schwartz, J.; Verkhusha, V. V. Photoactivatable mCherry for high-resolution two-color fluorescence microscopy. *Nat. Methods* **2009**, *6*, 153-159.

27. Geldhauser, T.; Ikegaya, S.; Kolloch, A.; Murazawa, N. Visualization of near-field enhancements of gold triangles by nonlinear photopolymerization. *Plasmonics* **2011, *6*,** 207-212.

28. Sharonov, A.; Hochstrasser, R. M. Wide-field subdiffraction imaging by accumulated binding of diffusing probes. *Proc. Natl. Acad. Sci. U. S. A.* **2006**, *103*, 18911-18916.

29. Fayyaz, S.; Tabatabaei, M.; Hou, R.; Lagugne-Labarthet, F. Surface-Enhanced Fluorescence: Mapping Individual Hot Spots in Silica-Protected 2D Gold Nanotriangle Arrays. *J. Phys. Chem. C* **2012**, *116*, 11665-11670.

30. Wertz, E.; Isaacoff, B.; Donehue, J.; Biteen, J. Single-molecule fluorescence unravels the coupling of light to a plasmonic nano-antenna. *Submitted* **2014**.

31. Tanaka, K. A. K.; Suzuki, K. G. N.; Shirai, Y. M.; Shibutani, S. T.; Miyahara, M. S. H.; Tsuboi, H.; Yahara, M.; Yoshimura, A.; Mayor, S.; Fujiwara, T. K.; Kusumi, A. Membrane molecules mobile even after chemical fixation. *Nat. Methods* **2010**, *7*, 865-866.

32. Levene, M. J.; Korlach, J.; Turner, S. W.; Foquet, M.; Craighead, H. G.; Webb, W. W. Zero-Mode Waveguides for Single-Molecule Analysis at High Concentrations. *Science* **2003**, *299*, 682-686.

33. Hao, Q.; Qiu, T.; Chu, P. K. Progress in Surface Science. *Prog Surf Sci* **2012**, *87*, 23-45.

34. He, R. Y.; Chang, G. L.; Wu, H. L.; Lin, C. H.; Chiu, K. C.; Su, Y. D.; Chen, S. J. Enhanced live cell membrane imaging using surface plasmon-enhanced total internal reflection microscopy. *Opt. Express* **2006**, *14*, 9307-9316.

35. Moal, E. L.; Fort, E.; Lévêque-Fort, S.; Cordelières, F. P.; Fontaine-Aupart, M. -.; Ricolleau, C. Enhanced Fluorescence Cell Imaging with Metal-Coated Slides. *Biophys. J.* **2007**, *92*, 2150-2161.

36. Lohmüller, T.; Triffo, S.; O'Donoghue, G. P.; Xu, Q.; Coyle, M. P.; Groves, J. T. Supported Membranes Embedded with Fixed Arrays of Gold Nanoparticles. *Nano Lett.* **2011**, *11*, 4912-4918.

Chapter 4 Studies of Polarization-Dependent Coupling Between Single Fluorescent Molecules and Gold Nanorods[ǂ]

ǂ *This work was done in collaboration with Ben Isaacoff, who calculated the electric field intensities for the gold NRs and helped design experiments described in future directions.*

4.1 Introduction

The beneficial properties of the localized surface plasmon resonances (LSPRs) of metal nanoparticles have been applied to the design of nanoscale devices, including imaging substrates, light emitting diodes, spectroscopy, bio-sensors, and solar cells.[1-7] Still, the tunability and performance of all these devices would benefit from an improved understanding of the polarization-dependent response of anisotropic nanoparticles (ANPs). The efficiency with which the LSPR of an ANP is excited depends on the polarization of the incident light source, and therefore, the photoluminescence collected from ANPs can reveal the particle orientation with respect to the excitation electric field. Previous work has taken advantage of this fact and used ANPs as nanoscale orientation sensors with very good photostability and localization precision[8,9] for both *in vitro*[10] and *in vivo* imaging applications.[11] The polarization-dependent response of ANPs has also been utilized for studying coupled ANP-fluorophore systems. In these systems, a fluorophore, or dipole emitter, is placed in the near field of a resonantly excited metallic nanoparticle where it can electromagnetically couple to the plasmon mode of the ANP.[8] The plasmon mode, or collective oscillation of free electrons, can modify the emission of

the fluorophore, and previous studies of coupled ANP-fluorophore systems have shown that the plasmon-coupled emission carries both the direction and polarization of the ANP.[8,12] Additionally, the excitation of a fluorophore can be enhanced by coupling to metallic ANPs, as the plasmon mode causes light to focus in the ANP near field and increases incident power felt by the fluorophore.[13]

Nanorods (NRs), one of the simplest ANPs, support two plasmon modes: the transverse mode, which is polarized along the rod short axis, and the longitudinal mode, which is polarized along the rod long axis. Exciting the nanorod with light polarized along one axis will selectively excite the corresponding LSPR mode. [8,14] This can be seen in Figure 4-1 where finite-difference time-domain (FDTD) electromagnetic calculations have been used to determine the local field enhancement near a NR with an aspect ratio (NR length divided by NR width) of 3:1 after excitation with wide-field broadband illumination at two orthogonal polarizations. Coupled emission from a NR-fluorophore system will consequently be polarized along whichever NR axis is selectively excited and can therefore provide nanoscale-sensing capabilities. These sensing capabilities could be used for studying *in vivo* cellular environments and dynamics[11] or nanoscale control of the emission properties, such as brightness and stability, of the coupled fluorophore.[8,15] Previous work has also shown that the fluorescence enhancement factor, or the ratio between fluorescence intensities corresponding to excitation polarizations parallel and perpendicular to the NR long axis, for coupled fluorophores can be manipulated and increased as the longitudinal plasmon mode of the NR is tuned to more closely match the laser excitation wavelength, and that the spectral shape of the fluorophore emission can

be influenced, such that coupled dyes preferentially emit at the NR longitudinal resonance wavelength.[12]

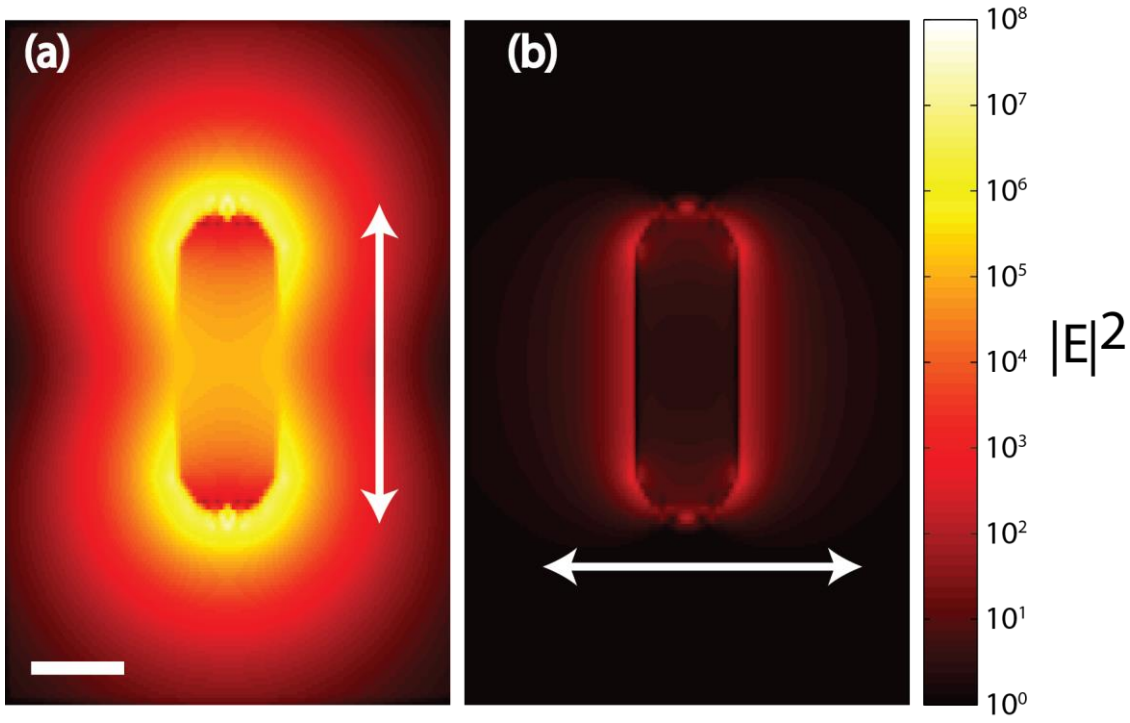

Figure 4-1. Finite-difference time-domain (FDTD) electromagnetic calculations of the local near field around a 3:1 aspect ratio Au NR excited by broadband light with two orthogonal polarizations (white arrows) and detected at 756 nm (a) and 516 nm (b). Colorbar is logarithmic, scale bar = 25 nm. Field map calculated by Ben Isaacoff with Lumerical software.

Though polarized emission in coupled ANP-fluorophore systems has been studied in ensemble measurements,[8,12,15] the phenomenon has only begun to be explored at the single-molecule level.[14,16] Previous polarization-resolved single-particle studies have informed on the local heterogeneity of a broad NP population,[14] while dark field scattering spectra[14] and photothermal imaging[9] have revealed the orientation of single NRs. There are many more avenues to explore at the level of single dye molecules coupling to individual ANPs, and developing a complete understanding of how

polarization affects coupling between fluorescent molecules and ANPs will increase tunability and control for applications in single-molecule sensing, catalysis, spectroscopy, and imaging.

In this Chapter, we use Au NRs, a specific case of ANPs, to study the emission from two dyes, mCherry (emission maximum at 610 nm) and Cy5.5 (emission maximum at 700 nm), whose emission overlap spectrally with the longitudinal plasmon resonance of 112 nm x 53 nm ("2:1") or 77 nm x 25 nm ("3:1") Au NRs, respectively. The longitudinal mode of the 2:1 NRs is centered at 620 nm, and the longitudinal mode of the 3:1 NRs is centered at 710 nm. To probe the polarization sensitivity of the plasmon-coupled fluorescence in these systems, we rotate the polarization angle of linearly polarized light resonant with the NR longitudinal plasmon mode and use single fluorescent molecules as reporters of this selective excitation through stochastic adsorption/desorption experiments.[17,18] We show polarization-dependent plasmon-enhanced emission of single Cy5.5 dyes. The maximum fluorescence enhancement, a 1.6-fold increase in the number of counts observed per coupled molecule per frame, is observed when the excitation polarization direction is aligned with the NR longitudinal axis. These results demonstrate our ability to selectively excite a single NR with specific orientation, and ultimately to control the amount of emission enhancement observed. The work in this Chapter on polarization-dependent excitation of coupled dye/NR systems develops the fundamental methods that will be needed to improve general SM detection schemes using polarization, and provides the foundation for future studies of the polarization-dependent *emission* of single-molecule/single-NR systems, an extension that is discussed at the end of this Chapter.

4.2 Experimental Methods

4.2.1 Cy5.5 and mCherry solutions

Solutions of Cy5.5 NHS ester (Lumiprobe) were prepared in DDI water to a concentration of 54 nM. Solutions of mCherry, made from reconstituted purified proteins (BioVision, Inc.), were prepared in pH 7.4 phosphate buffered saline (PBS, BioExpress Tablets, Biotechnology grade) to a concentration of 175 nM.

4.2.2 Gold nanorod substrates

Glass microscope coverslips were etched in an O_2-plasma (200 mTorr, 10 min; PE-50, Plasma Etch Inc.). Gold nanorods (NRs) with length 112 nm and radius 53 nm or length 77 nm and radius 25 nm (2:1 or 3:1 NRs, respectively) were purchased from Nanopartz Inc. (Loveland, CO) and used as received. As described previously,[18] gold NR substrates were prepared using a spin-assisted layer-by-layer technique:[19] films of positively charged poly(diallyldimethyl ammonium chloride) polyelectrolyte solution (PDADMAC, Sigma Aldrich) and negatively charged poly(sodium 4-styrene) polyelectrolyte solution (PSS, Sigma Aldrich) were used to immobilize 3:1 (for Cy 5.5 experiments) and 2:1 (for mCherry experiments) NRs to the surface of the glass coverslips. Polyelectrolyte solutions (20% by weight in water) were diluted in DDI water to 20 mM (calculated using monomeric weights). Dilute PDADMAC was spun onto the cleaned coverslips (300 μL, 15 s, 4000 rpm), then washed three times with DDI water. A mixture of NRs and dilute PSS was then spun onto the coated coverslip (150 μL NRs, 150 μL PSS, 15 s, 4000 rpm), and cleaned with three DDI water washes.

4.2.3 Dark-field scattering spectroscopy

NR substrates for dark-field experiments were prepared on O_2-plasma cleaned glass coverslips as described above. A broadband halogen light source (400 – 1000 nm) was used to excite the sample through a dark-field condenser, which was aligned using a 10x objective and a scratched glass coverslip, and scattered light was collected in an Olympus IX71 inverted microscope equipped with a dark-field oil-immersion objective (NA = 0.6). NR substrates were immersed in water and covered by a microscope slide. The diffraction-limited image of a single NR was aligned to the entrance slit of an imaging spectrograph (Acton SP-2300i, Princeton Instruments) and dispersed by a 150 g/mm grating. Spectral data was collected with an EMCCD (Andor iXon). Background spectra (collected from nearby positions with no NR image on the entrance slit) were subtracted from measured spectra, and all data were divided by the broadband spectrum of the halogen light source to correct for the system spectral efficiency.

4.2.4 Determining the orientation of isolated NRs

For each experiment, NR fluorescence in the absence of any added fluorophores was initially collected as the half-wave plate was rotated at a constant velocity of 20 deg/s (Figures 4-2a and 4-2b). The longitudinal mode of a single gold NR will be most efficiently excited when the excitation polarization is aligned along the NR long axis.[9,14] The fluorescence intensity response of a single NR will therefore have the form

$$I(\phi) = I_0 \cos^2(\phi - q) \tag{1}$$

where ϕ is the polarization angle and q is the NR orientation with respect to the laboratory frame.[9,14] An aggregate of multiple NRs, on the other hand, will not have two

orthogonal axes of symmetry, and thus will not have a fluorescence intensity response in the form of Equation (1). The characterization of diffraction-limited NR photoluminescence as a function of excitation polarization can therefore be used to identify isolated, single NRs despite the fact that single NRs and small NR aggregates are indistinguishable in standard light microscopy due to the diffraction limit of light. Khatua et al. used Lorentzian fits of the NR emission line shape to confirm that observed diffraction-limited spots arose from single NRs,[20] but this method requires a spectrometer whereas an intensity-based characterization is directly accessible in all imaging systems.

Thus, in this Chapter, we identify single NRs by their cosine-squared intensity response, and only such single NRs are used in all subsequent analysis. Figures 4-2a and 4-2b show the mean fluorescence intensity per frame (green line) as a function of frame number for two NRs (with 3:1 and 2:1 aspect ratio, respectively). For each NR identified as an isolated single NR based on a good fit (e.g., R^2=0.97780 in Figure 4-2a, R^2=0.9355 and in Figure 4-2b) to equation (1) above, this scattering intensity vs. polarization angle measurement is repeated with finer polarization angle spacing (10^o intervals between 0^o and -90^o for the 3:1 NR in Figure 4-3a and between 0^o and -180^o for the 2:1 NR in Figure 4-3b) to precisely determine the NR orientation. The NR in Figure 4-3a, for example, is aligned along the laboratory-frame axis of 17^o, and the NR in Figure 4-3b is aligned along the laboratory-frame axis of 13^o.

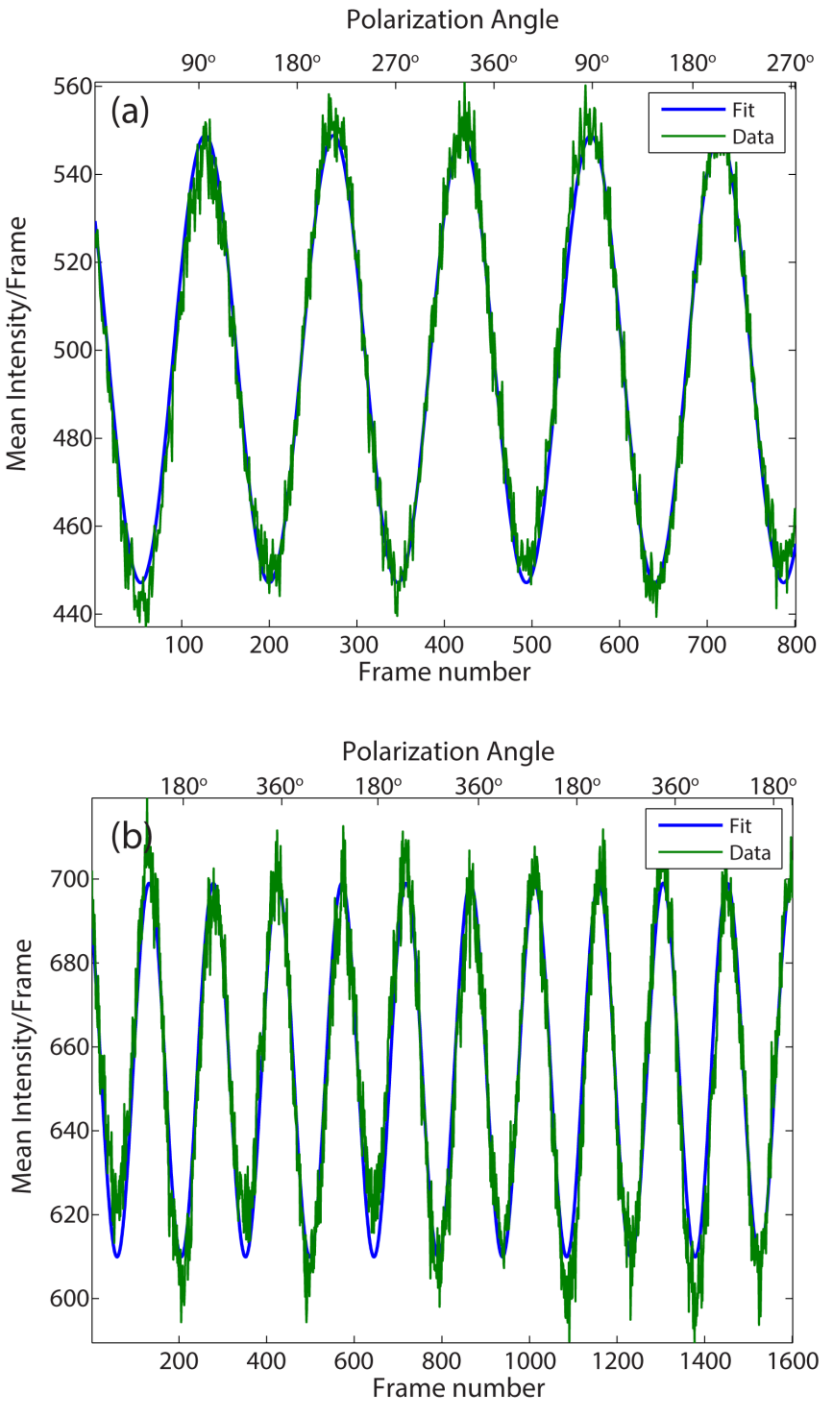

Figure 4-2. (a) Single 3:1 NR and (b) single 2:1 NR mean photoluminescence intensity per imaging frame (green lines) as a function of frame number (40 ms/frame). Data is fit (blue lines) to a cosine-squared function to prove that the fluorescence is truly originating from an isolated NR. Excitation wavelength = 640 nm in (a), excitation wavelength = 561 nm in (b).

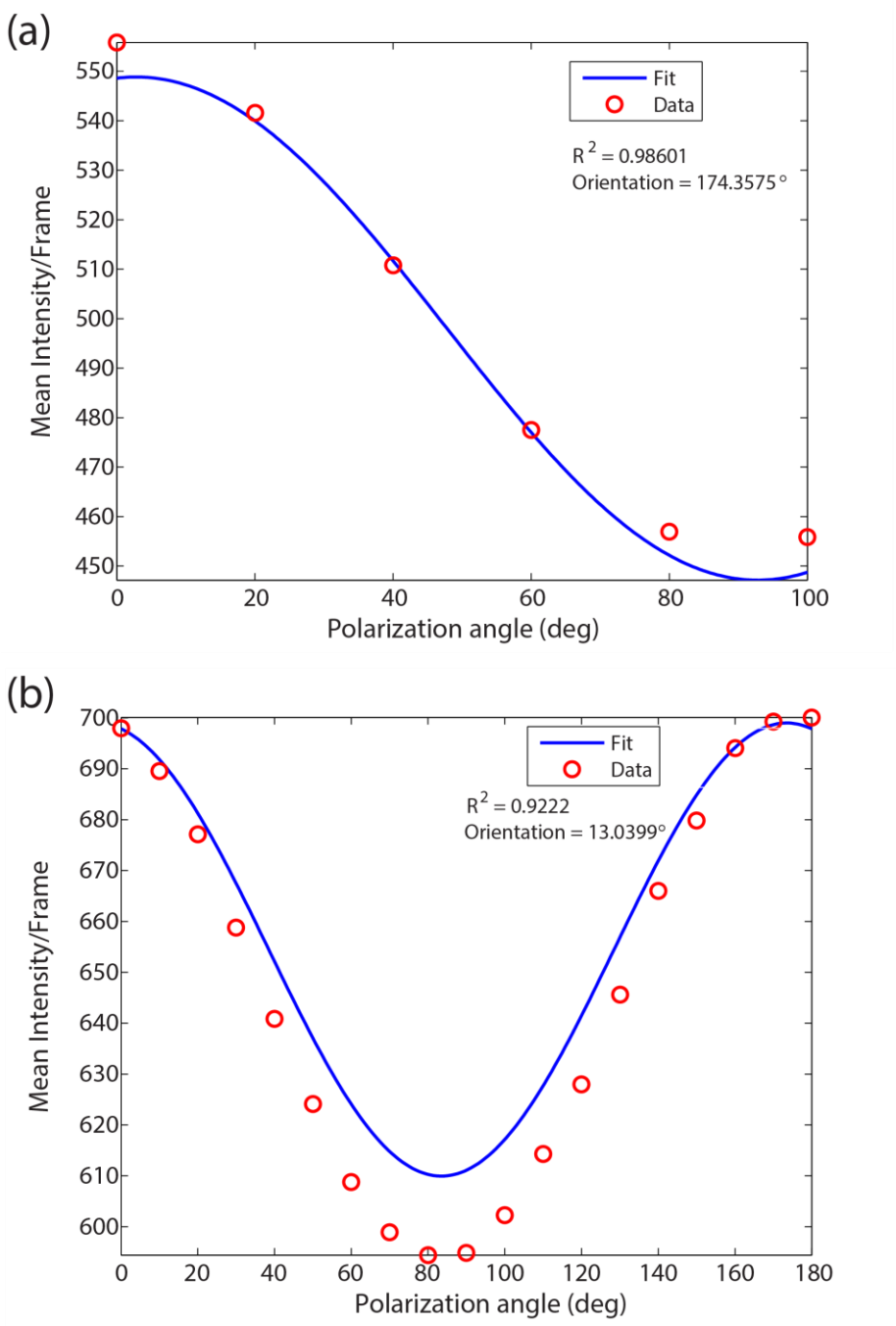

Figure 4-3. Mean fluorescence intensity per imaging frame (red circles) for the same single 3:1 (a) and single 2:1 (b) NR measured in Figure 2(a) and 2(b), respectively. Measurements are fit to Equation (1) (blue line) to determine precise NR orientation. Excitation wavelength = 640 nm in (a), excitation wavelength = 561 nm in (b).

4.2.5 PAINT Imaging of Cy5.5 and mCherry on nanorods

As described in Chapter 2, the PAINT super-resolution method (Points Accumulation for Imaging in Nanoscale Topography)[17] was used to study the coupling of the fluorophores and NRs. Briefly, in these PAINT experiments, the NR substrate was immersed in a fluorophore solution, from which fluorophore molecules can stochastically adsorb on and desorb from the surface over time. Fluorophores that adsorb to the substrate surface are visualized on the EMCCD detector as discrete punctate spots, whereas fluorophores freely diffusing in solution (i.e., those molecules not adsorbed onto the substrate surface) are invisible because their motion is too fast to be resolved by the EMCCD (operated at a 25-Hz frame rate). For our PAINT experiments, the NR substrates (isolated NRs immobilized on a glass coverslip in PSS) were immersed in 75 – 100 μL of 54 nM Cy5.5 in water or 175 nM FP in PBS contained by a small rubber O-ring previously cleaned by sonication in acetone.

Figure 4-4 shows a schematic of the experimental setup used for PAINT experiments. For linearly polarized excitation experiments, single Cy5.5 molecules were excited with linearly polarized 640-nm laser light (Coherent Cube 640-40C and Thorlabs 400 nm – 800 nm achromatic half-wave plate) and single mCherry molecules were excited with linearly polarized 561-nm laser light (Coherent Sapphire 561-50 and Thorlabs 400 nm – 800 nm achromatic half-wave plate). The linear polarization was rotated with an achromatic half-wave plate (Thorlabs AHWP10M 400 nm – 800 nm) mounted in a motorized precision rotation mount and controlled by a T-Cube DC servo motor controller (Thorlabs) (Figure 4-4a). In benchmarking experiments, single Cy5.5 molecules were excited with circularly polarized 640-nm laser light (Coherent Cube 640-

40C and Tower Optical 0.25-633 quarter-wave plate). In all of these single-molecule fluorescence experiments, fluorescent emission was detected in a wide-field epifluorescence microscope (Olympus IX71) equipped with a 1.40-NA 100× oil-immersion objective. Emission was filtered appropriately (Semrock Di01-R635/BLP01-535 or Di01-R561/BLP01-561R for Cy5.5 or mCherry, respectively) to maximize signal transmission and minimize scattered laser light, then imaged on a 512×512 pixel Andor iXon EMCCD at 25 Hz for 5 – 7 minutes (Figure 4-4b). The constant photoluminescence signal of the gold nanorods was subtracted using the average intensity of 50-frame segments prior to image processing. Emission intensities, molecular positions and counts detected per frame were extracted from the data by least-squares fitting of background-subtracted signal intensity to a 2D Gaussian function with the MATLAB routine *nlinfit*.

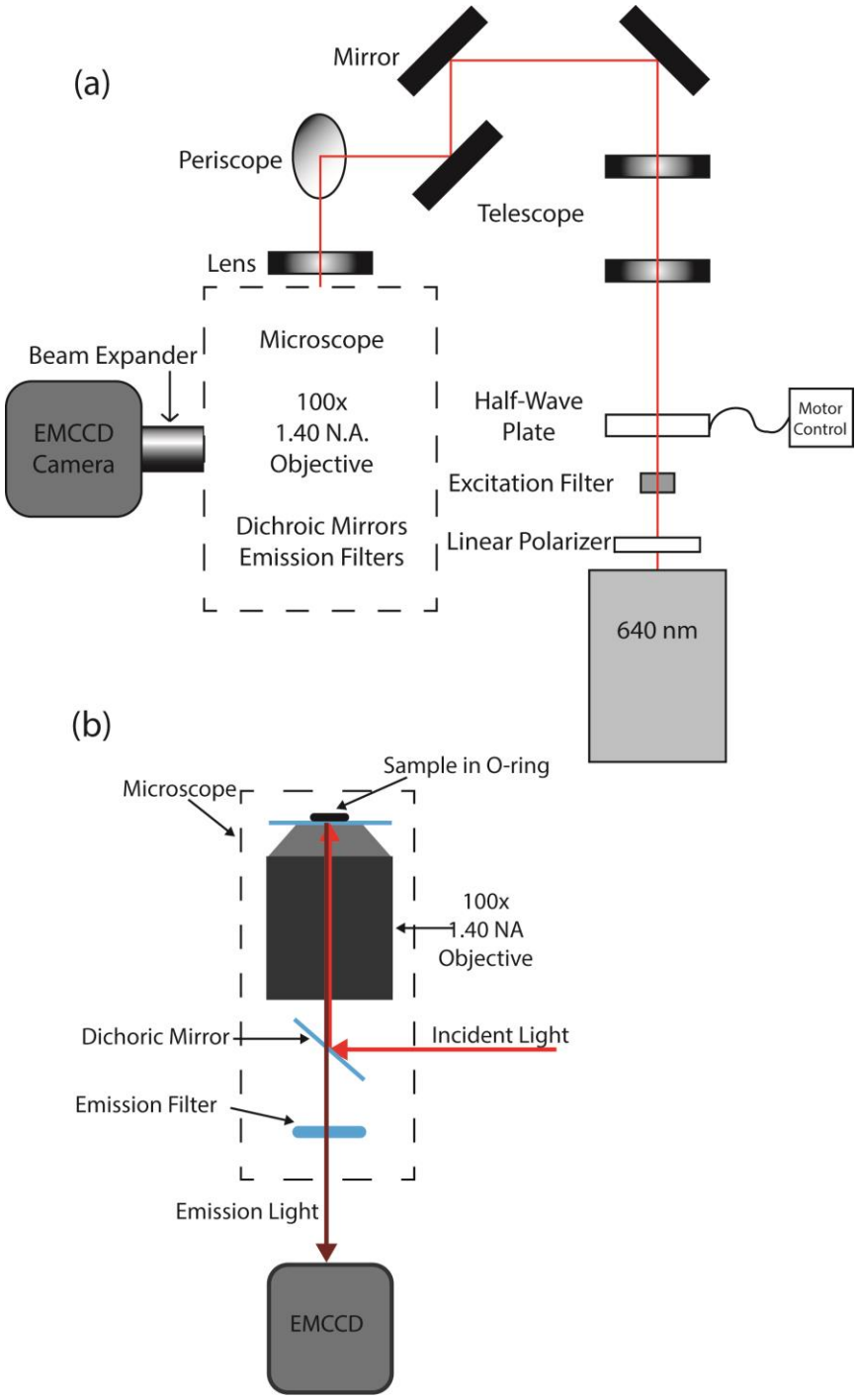

Figure 4-4. Schematic of linearly polarized excitation PAINT microscopy experiments. (a) A linear polarizer selects a single polarization from the circularly polarized laser output, and an excitation filter ensures a narrow excitation bandwidth. The laser light is passed through a half-wave plate, which rotates the linearly polarized light The diagonal arrow after the half-wave plate indicates the rotation of the linear polarization of the 640-nm laser excitation source. A telescope expands the beam to fill the objective back aperture. (b) Collimated incident light (light red) excites the sample, contained by a rubber O-ring, and emitted light (dark red) is collected by the same objective before being appropriately filtered and imaged on the EMCCD. Figure adapted from Beth Haas.

4.3 Results and Discussion

4.3.1 Spectral properties of fluorophores and gold nanorods

Gold NRs (Nanopartz Inc.) were used as received and immobilized (see Experimental Methods 4.2.2) in polyelectrolyte films on the surface of glass coverslips.[19] The NR scattering spectra were collected by dark-field spectroscopy; representative single-NR scattering spectra are shown in Figures 4-5 and 4-6 for the 3:1 NRs (navy blue curve) and the 2:1 NRs (royal blue curve), respectively. Both sizes of NR show two peaks in the scattering spectrum, reflecting the nanorod anisotropy. The bluer peak corresponds to the transverse LSPR mode, while the redder peak corresponds to the longitudinal LSPR mode.[21] The fluorescence excitation (dashed line) and emission (solid line) of the relevant fluorophore is shown alongside the NR scattering spectrum in each of these figures. In Figure 5, the emission of Cy5.5 (excitation wavelength: 640 nm) overlaps very well with the longitudinal plasmon mode peak of the 3:1 NR, centered at 713 nm, and there is no overlap of either the excitation or emission of Cy5.5 with the transverse mode, centered at 565 nm. Figure 4-6 shows that the mCherry emission (excitation wavelength: 561 nm) overlaps with the 2:1 NR longitudinal plasmon mode, centered at 620 nm. In both of these cases, the fluorophore emission is therefore expected to couple to the longitudinal mode of the respective NR

Interestingly, in contrast to Cy5.5, the excitation of mCherry also overlaps with the transverse mode of the 2:1 rod, centered at 546 nm. Because the plasmon modes of the 2:1 NRs are not well separated, the laser excitation wavelength at 561 nm excites the system on the red-edge of the transverse mode and the blue-edge of the longitudinal mode, making it unclear exactly which mode is most efficiently excited. Thus, in the case

of mCherry, separating the effects of plasmon-coupled excitation from the effects of plasmon-coupled emission is difficult.

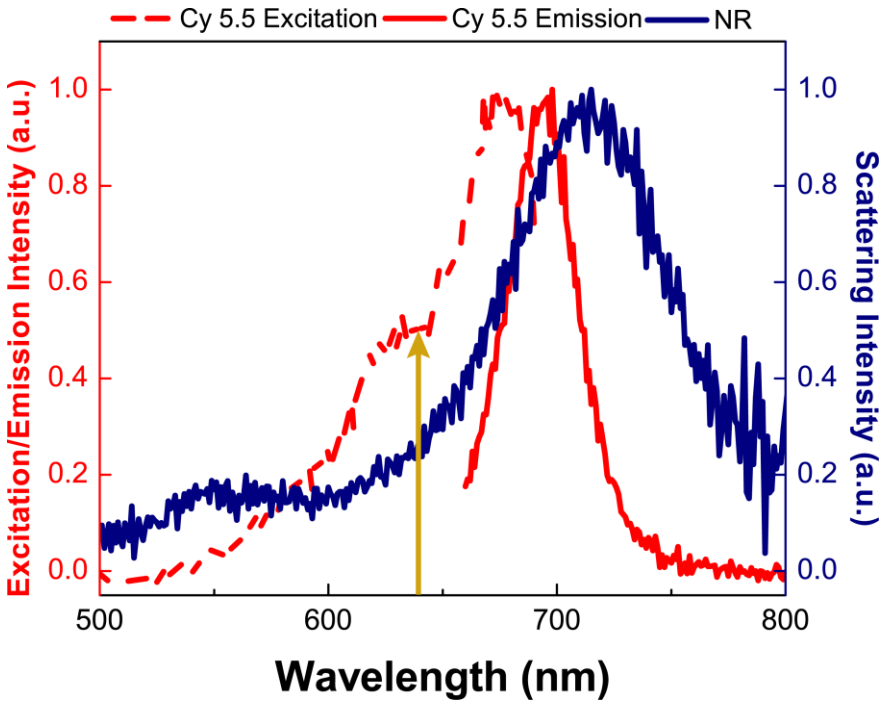

Figure 4-5. Dark-field scattering spectra of 77 nm x 25 nm gold NRs (navy) and fluorescence excitation (dashed red) and emission (solid red) spectra of Cy5.5. Fluorescence emission measured with 640-nm excitation (red arrow). All spectra collected in water.

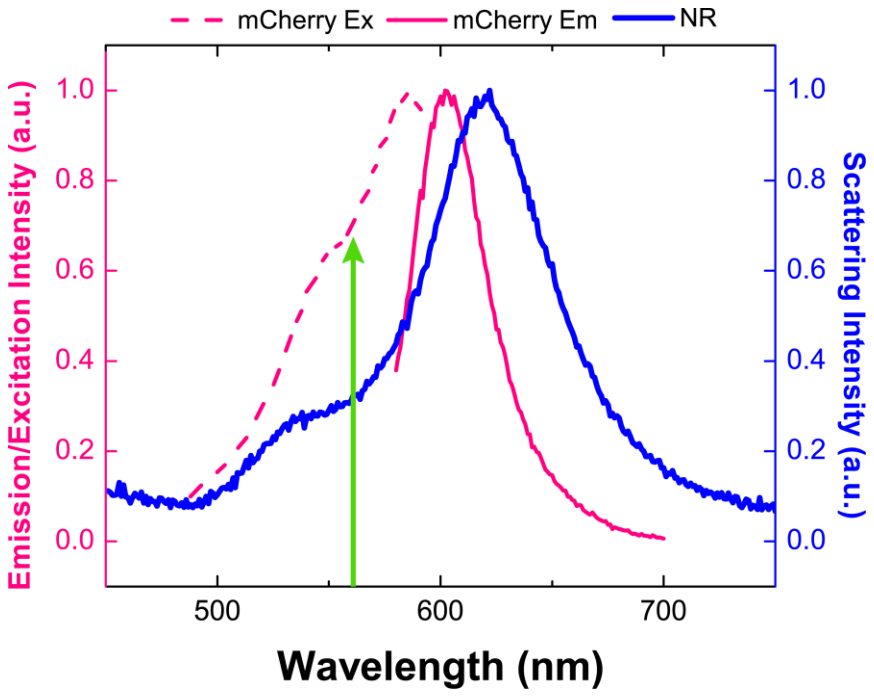

Figure 4-6. Dark-field scattering spectra of 112 nm x 53 nm gold NRs (blue) and fluorescence excitation (dashed pink) and emission (solid pink) spectra of mCherry. Fluorescence emission measured with 561-nm excitation (green arrow). NR spectrum collected in water, mCherry spectra collected in PBS buffer (pH = 7.4).

4.3.2 PAINT detection of fluorophore-nanorod coupling using circularly polarized excitation

Prior to studying the polarization-dependent response of fluorophore-NR systems, PAINT experiments using circularly polarized light were done to measure the enhancement due to coupling fluorophores to resonantly excited plasmonic nanoparticles when all fluorophores in the system are excited equally regardless of orientation.

PAINT experiments studying the coupling between mCherry and 2:1 NRs were discussed previously (Chapter 2); in those experiments an average enhancement of 2.1× was observed for coupled mCherry molecules.[18]

Here, we studied the coupling of Cy5.5 molecules and 3:1 NRs using the PAINT technique and circularly polarized excitation light. A Cy5.5 dye solution was added above the 3:1 NRs sample (see Methods, Section 4.2.5) and the fluorescence emission of adsorbing dye molecules was recorded. The rate of adsorption was minimized by maintaining a low concentration of fluorophores in solution (75 – 100 μM); this low probability of adsorption ensured spatially isolated single-molecule detection events. Each adsorbed molecule that was detected on the EMCCD as a punctate spot was fit using a super-resolution algorithm to determine the position and intensity of emission. A 5 × 5 pixel (245 nm × 245 nm) region of interest centered about the NR (identified from a fit to the diffraction-limited NR scattering image) was designated the "on-NR" region, which encompasses the NR near-field in which region fluorophores are strongly coupled to the resonantly enhanced local field (Figure 4-7a). By separating emission spots with a center position inside the 5x5 pixel "on-NR" region to emission events outside the region ("off-NR"), the emission of fluorophores adsorbing in this 5 x 5 pixel region was compared to the emission of fluorophores adsorbing elsewhere on the sample to determine the observed enhancement.

Figure 4-7b compares the fluorescence rates (intensity/molecule/frame) of Cy5.5 molecules "on NR" (red) to that of Cy5.5 molecules "off NR" (black). The "on NR" molecules have an average fluorescence rate of approximately 80,000 counts/molecule/frame, while "off NR" molecules have an average fluorescence rate of approximately 23,000 counts/molecule/frame. The molecules in the "on NR" region, which encompasses the NR near-field in which region fluorophores are strongly coupled to the resonantly enhanced local field coupled population, therefore shows an average

emission enhancement of 3.5× the rate of fluorescence when compared to the uncoupled population, demonstrating that coupling to the NRs results in brighter molecules.

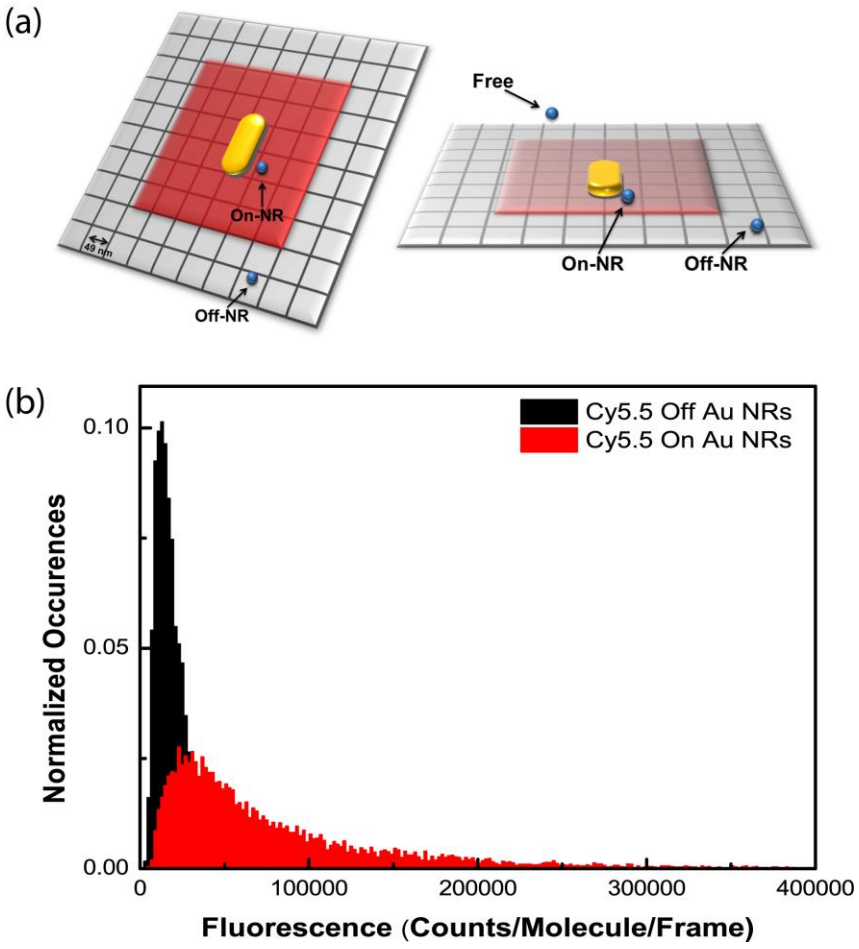

Figure 4-7. (a) Cartoon showing the "on-NR" and "off-NR" regions. (b) Comparison of single-molecule fluorescence for Cy5.5 molecules on a gold NR (red) and off a gold NR (black). The average rate of fluorescence for the on NR population is 79,893 counts/molecule/frame. The average rate of fluorescence for the off NR population is 22,965 counts/molecule/frame. 640-nm laser excitation.

4.3.3 PAINT detection of Cy5.5-3:1 NR coupling using linearly polarized excitation

After the precise orientation of each 3:1 NR was determined, a Cy5.5 dye solution was added above the sample and the fluorescence emission of adsorbing dye molecules was recorded in a PAINT experiment, as described above, with the excitation polarizations at 0^o, 90^o, 180^o, 270^o, and 360^o. To determine the fluorescence enhancement of single Cy5.5 molecules coupled to the gold NR, the average intensity per molecule per frame for all molecules localized in the on-NR region was divided by the average intensity per molecule per frame of the off-NR population. In Figure 4-8, we see the greatest enhancement at 0^o, 180^o, and 360^o. At these angles, the excitation polarization direction approximately coincides with the longitudinal NR axis (blue dashed line in Figure 4-8). Furthermore, we detect essentially no enhanced fluorescence (enhancement factor ≈ 1) at angles orthogonal to the NR longitudinal axis (i.e., 90^o and 270^o). Thus, we conclude that the emission from Cy5.5 molecules near gold NRs is maximally enhanced when the excitation source polarization is in the direction of the NR longitudinal axis, whose plasmon resonance is spectrally matched to the Cy5.5 emission spectrum. In these PAINT experiments, Cy 5.5 molecules are used as reporters of their environment and monitor the excitation efficiency of the plasmon mode: when the longitudinal mode is efficiently excited by the proper linear polarization, enhancement is maximized for coupled fluorescent molecules. These results show that we can efficiently and selectively excite the longitudinal mode of the gold NR, and in doing so, control the amount of plasmon-enhanced emission observed. These results have direct implications for work studying biological samples where the concentrations of biological analytes are often too

high for SM detection.[22] Utilizing the selectivity and control offered by polarization-dependent plasmon-enhanced emission could offer a way to control or reduce the number of molecules observed in an excitation volume to a level appropriate for SM detection.

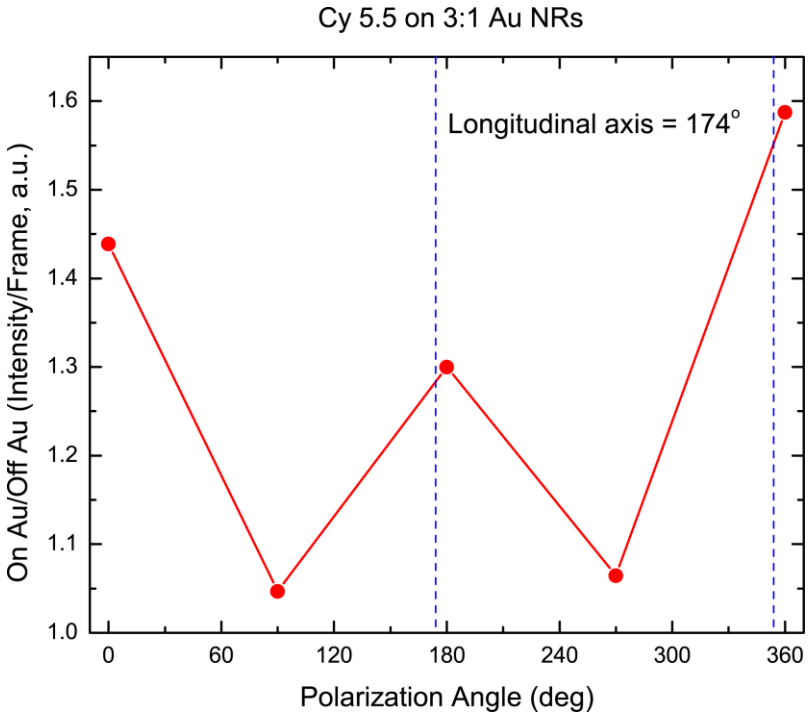

Figure 4-8. Fluorescence enhancement of Cy 5.5 molecules as a function of excitation polarization angle (red line). The longitudinal NR axis was determined in Figure 6 to be oriented at 174° (blue dashed line).

4.3.4 PAINT detection of mCherry-2:1 NR coupling using linearly polarized excitation

Similar PAINT experiments were done exciting the fluorescent protein mCherry near a 2:1 gold NR whose long axis lies along the laboratory-frame axis of 13^{o} with linearly polarized light at angles of 0^{o}, 90^{o}, 180^{o}, and 270^{o}. In contrast to the results in Figure 4-8 for Cy5.5, in Figure 4-9, we observe maximum emission enhancement at 90^{o} and 270^{o} and minimal emission enhancement at 0^{o} and 180^{o}. We can see from Figure 4-3b that the NR used for the experiment has a cosine-squared fluorescence intensity response, and so, is indeed an isolated NR. Figure 4-9, however, suggests there is maximum emission enhancement, and consequently maximum coupling, at angles orthogonal to the longitudinal axis of the NR. We believe at this time that the experiments are not optimized, and so, we make no strong claims in this Chapter about the results or the mechanism.

However, these results are surprising because as shown previously in Chapter 2, and in work by Fu et al.,[23] the emission rate of mCherry can be easily enhanced by coupling to 2:1 gold NRs when excited using circularly polarized light. If all angles from the linearly polarized excitation experiments are collapsed into two histograms, one for the on-NR population and one for the off-NR, we can see a small enhancement for the mCherry emission rate of the on-NR population (Figure 4-10, the on-NR population has an emission rate that is 1.3× that of the off-NR population), but it is different from the enhancement observed in Chapter 2. This result is interesting because it suggests there is something fundamentally different when the system is selectively excited using linearly polarization. One possible explanation is the longitudinal and transverse modes are highly

coupled and in experiments where circular polarization is used to excited the system we are observing enhancement due to coupling to both modes.

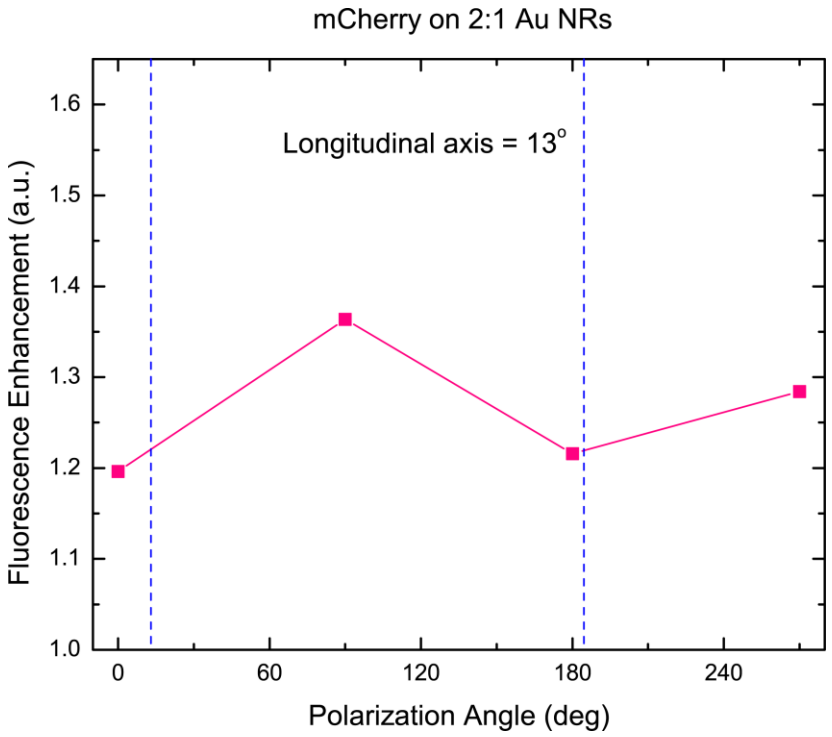

Figure 4-9. Fluorescence enhancement of mCherry molecules as a function of excitation polarization angle (pink line). The longitudinal axis of the rod is shown (blue dashed line), as determined in Figure 4-3b.

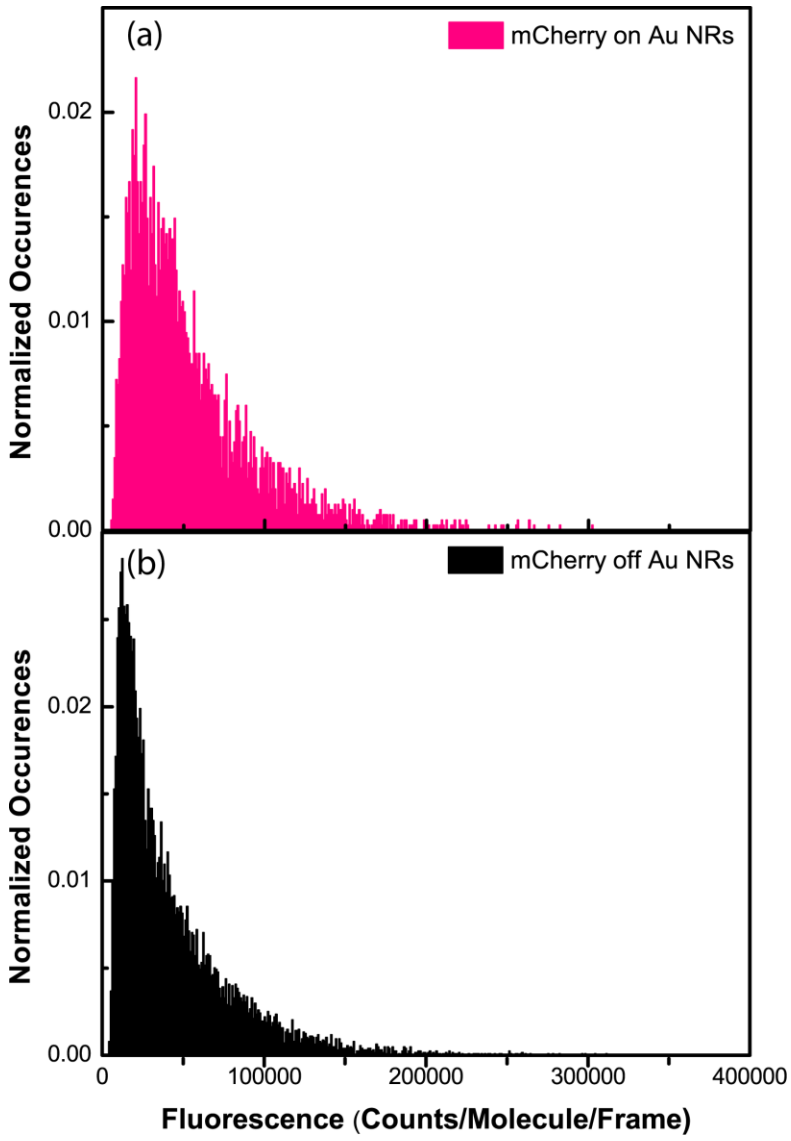

Figure 4-10. Histograms comparing the photon detection rates for all angles in linear excitation experiments. The (a) on-NR population has an average photon detection rate of 53,431 counts/molecule/frame while the (b) off-NR population has an average photon detection rate of 42,693 counts/molecule/frame.

4.4 Conclusions and Future Directions

In this Chapter, we have demonstrated the ability to selectively excite the longitudinal mode of gold NRs, and consequently we are able to control the amount of plasmon-enhanced emission observed from coupled Cy5.5 molecules. These results highlight our ability to control the emission properties of coupled molecules on the nanoscale and are an important first step in developing applications that utilize the polarization-dependent response of anisotropic nanoparticles.

As mentioned above, the mCherry-2:1 NR experiments must be optimized for future experiments in order to definitively assign a coupling mechanism and understand the anomalous results shown in this chapter. Additionally, future work on this project will be focused on designing and conducting experiments that monitor emission as a function of polarization. For these experiments, a linear polarizer will be placed after the microscope and before the EMCCD, allowing the polarization angle of emission detection to be rotated. By exciting fluorophore-NR systems with circularly polarized light (Figure 4-11) and monitoring the emission as a function of polarization, we will gain an understanding of the efficiency of coupling of the Cy5.5 molecules to the plasmon mode. If linearly polarized excitation is used (Figure 4-12), we will be able to understand the efficiency of energy transfer to the plasmon mode, as well as monitor the energy transfer between the two plasmon modes if the appropriate excitation wavelength and fluorophores are used. For example, exciting the Cy5.5/3:1 NR system at the transverse mode (which is near 565 nm, therefore excitation wavelength of 561 nm) and monitoring the polarization of any plasmon-enhanced emission from Cy5.5 past 650 nm (due to long-pass filters used in the microscope) would reveal any energy transfer between the transverse and longitudinal

modes of the NR. Collectively, these experiments will allow us to better understand polarization-dependent coupling in the fluorophore-NP systems and increase tunability and control for applications in single-molecule techniques.

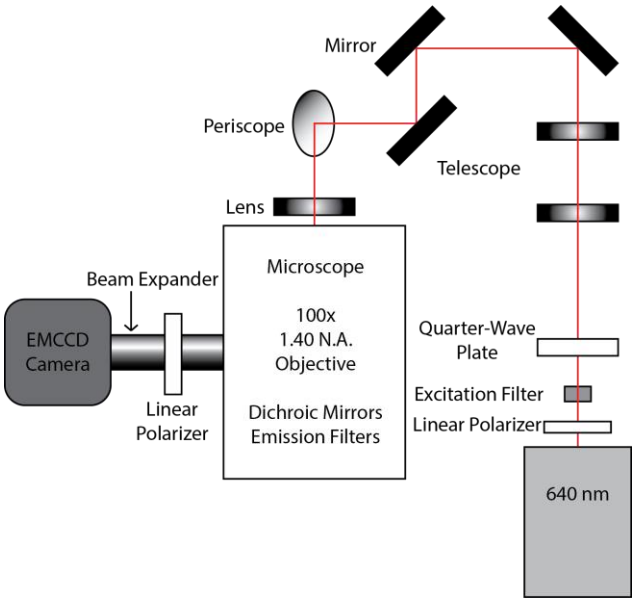

Figure 4-11. Schematic for experiments monitoring emission as a function of polarization using circular excitation. A quarter-wave plate will generate circularly polarized excitation light (640 nm) and a linear polarizer in the emission pathway will allow the emission of the coupled fluorophore-ANP system to be monitored as a function of polarization. Figure adapted from Beth Haas.

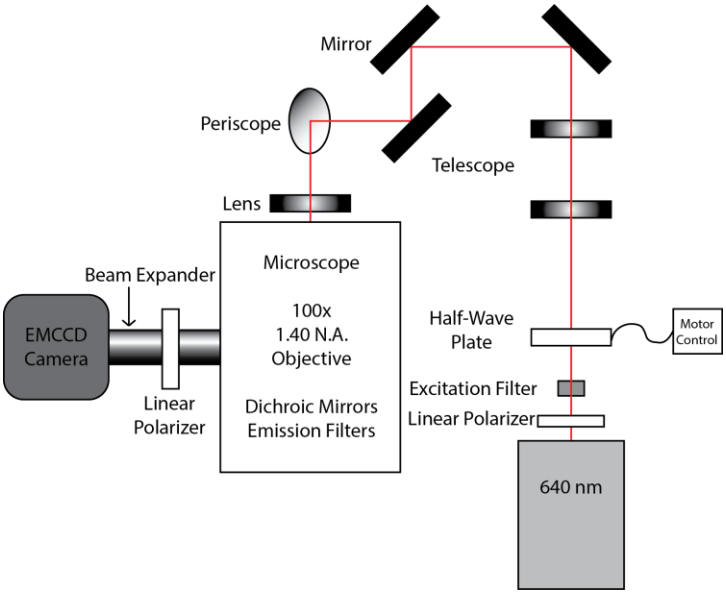

Figure 4-12. Schematic for experiments monitoring emission as a function of polarization using linearly exciation. A half-wave plate generates linearly polarized excitation light (640 nm), which can be rotated using a computer-controlled motor. Red diagonal arrow after the half-wave plate indicates the rotation of the linear polarization of excitation light. A linear polarizer in the emission pathway will allow the emission of the coupled fluorophore-ANP system to be monitored as a function of polarization. Figure adapted from Beth Haas.

References

1. Barnes, W. L.; Dereux, A.; Ebbesen, T. W. Surface plasmon subwavelength optics. *Nature* **2003**, *424*, 824-830.

2. Ozbay, E. Plasmonics: Merging Photonics and Electronics at Nanoscale Dimensions. *Science* **2006**, *311*, 189-193.

3. Lal, S.; Link, S.; Halas, N. J. Nano-optics from sensing to waveguiding. *Nature Photon.* **2007**, *1*, 641-648.

4. Willets, K. A.; Van Duyne, R. P. Localized surface plasmon resonance spectroscopy and sensing. *Annu. Rev. Phys. Chem.* **2007**, *58*, 267-297.

5. Anker, J. N.; Hall, W. P.; Lyandres, O.; Shah, N. C.; Zhao, J.; Van Duyne, R. P. Biosensing with plasmonic nanosensors. *Nature Mater.* **2008**, *7*, 442-453.

6. Atwater, H. A.; Polman, A. Plasmonics for Improved Photovoltaic Devices. *Nature Mater.* **2010**, *9*, 205.

7. Schuller, J. A.; Barnard, E. S.; Cai, W.; Jun, Y. C.; White, J. S.; Brongersma, M. L. Plasmonics for extreme light concentration and manipulation. *Nature* **2010**, *9*, 193-204.

8. Mertens, H.; Polman, A.; Biteen, J. S.; Atwater, H. A. Polarization-Selective Plasmon-Enhanced Silicon Quantum Dot Luminescence. *Nano Lett.* **2006**, *6*, 2622-2625.

9. Chang, W. S.; Ha, J. W.; Slaughter, L. S.; Link, S. Plasmonic nanorod absorbers as orientation sensors. *Proc. Nat. Acad. Sci.* **2010**, *107*, 2781-2786.

10. Sonnichsen, C.; Alivisatos, A. P. Gold Nanorods as Novel Nonbleaching Plasmon-Based Orientation Sensors for Polarized Single-Particle Microscopy. *Nano Lett.* **2005**, *5*, 301-304.

11. Xu, D.; He, Y.; Yeung, E. S. Direct Imaging of Transmembrane Dynamics of Single Nanoparticles with Darkfield Microscopy: Improved Orientation Tracking at Cell Sidewall. *Anal. Chem.* **2014**, *86*, 3397-3404.

12. Ming, T.; Zhao, L.; Yang, Z.; Chen, H.; Sun, L.; Wang, J.; Yan, C. Strong Polarization Dependence of Plasmon-Enhanced Fluorescence on Single Gold Nanorods. *Nano Lett.* **2009**, *9*, 3896-3903.

13. Anger, P.; Bharadwaj, P.; Novotny, L. Enhancement and Quenching of Single-Molecule Fluorescence. *Phys. Rev. Lett.* **2006**, *96*, 113002.

14. Koen, K. A.; Weber, M. L.; Mayer, K. M.; Fernandez, E.; Willets, K. A. Spectrally-Resolved Polarization Anisotropy of Single Plasmonic Nanoparticles Excited by Total Internal Reflection. *J. Phys. Chem. C* **2012**, *116*, 16198-16206.

15. Ming, T.; Zhao, L.; Chen, H.; Woo, K. C.; Wang, J.; Lin, H. Experimental Evidence of Plasmophores: Plasmon-Directed Polarized Emission from Gold Nanorod - Fluorophore Hybrid Nanostructures. *Nano Lett.* **2011**, *11*, 2296-2303.

16. Fu, Y.; Zhang, J.; Lakowicz, J. R. Plasmon-Enhanced Fluorescence from Single Fluorophores End-Linked to Gold Nanorods. *J. Am. Chem. Soc.* **2010**, *132*, 5540-5541.

17. Sharonov, A.; Hochstrasser, R. M. Wide-field subdiffraction imaging by accumulated binding of diffusing probes. *Proc. Natl. Acad. Sci. U. S. A.* **2006**, *103*, 18911-18916.

18. Donehue, J. E.; Wertz, E.; Talicska, C. N.; Biteen, J. S. Plasmon-Enhanced Brightness and Photostability from Single Fluorescent Proteins Coupled to Gold Nanorods. *J. Phys. Chem. C* **2014**, *118*, 15027-15035.

19. Chiarelli, P. A.; Johal, M. S.; Holmes, D. J.; Casson, J. L.; Robinson, J. M.; Wang, H. Polyelectrolyte Spin-Assembly. *Langmuir* **2002**, *18*, 168-173.

20. Khatua, S.; Paulo, P. M. R.; Yuan, H.; Gupta, A.; Zijlstra, P.; Orrit, M. Resonant Plasmonic Enhancement of Single-Molecule Fluorescence by Individual Gold Nanorods. *ACS Nano* **2014**, *8*, 4440-4449.

21. Alekseeva, A. V.; Bogatyrev, V. A.; Khlebtsov, B. N.; Mel'nikov, A. G.; Dykman, L. A.; Khlebtsov, N. G. Gold nanorods: Synthesis and optical properties. *Colloid J.* **2006**, *68*, 661-678.

22. Acuna, G.; Grohmann, D.; Tinnefeld, P. Enhancing single-molecule fluorescence with nanophotonics. *FEBS Lett.* **2014**, 1-6.

23. Fu, B.; Donehue, J.; Isaacoff, B.; Rowland, D.; Biteen, J. Distance-dependent Plasmonic Fluorescence Enhancement of Single Fluorophore on a Gold Nanorod. *In preparation* **2014**.

Chapter 5 Conclusions and Future Directions

5.1 Summary

In this Thesis, we have developed protocols for coupling fluorescent proteins (FPs) to plasmonic gold substrates and we have designed *in vitro* experiments to demonstrate enhanced emission, as well as increased photostability, from single FPs coupled to gold NRs. Additionally, we have shown that coupling an FP to a single NR leads to a shift in the apparent emission position toward the NR center; this is due to re-radiation through the NR plasmon mode. We have also shown that plasmon-enhanced emission from single FPs can increase the fluorescence signal for *in vivo* imaging of membrane-bound proteins inside live *Vibrio cholerae* bacteria cells. In these experiments, we resolved a re-radiation pattern that is localized near the edges of gold nanotriangles and not shifted to the nanoparticle center, like what was observed in experiments done with NRs. Finally, we demonstrated that selective polarization-dependent excitation of anisotropic gold NRs yields polarization-dependent emission from coupled Cy5.5 dye molecules, providing a new avenue of selectivity in single-molecule experiments. Through exploring plasmon-enhanced FP emission, applying this understanding to *in vivo* systems, and demonstrating increased selectivity for addressing nanostructures on the nanometer scale, we have developed a new approach for improving super-resolution microscopy in living cells.

5.2 Future Directions

This Thesis presents the first demonstration of plasmon enhancement of fluorescent protein emission and investigates this coupling at the single-molecule level, both *in vitro*

and *in vivo*. These studies are an important step in the expansion of single-molecule techniques for bio-imaging applications. However, and there is still much work that can be done to expand the foundational work described in this Thesis for widespread application in biological studies.

5.2.1 Expanding our understanding of plasmon-enhanced FP emission

Because plasmon-enhanced fluorescence is a highly distance-dependent effect, the logical first step to expand upon the *in vitro* work presented in Chapter 2 is to study the distance dependence of FP enhancement on the single-molecule level. The distance dependence of a single fluorescent dye coupled to a gold nanopshere on an AFM tip was previously studied and described in detail by Novotny *et al*.[1] They showed that fluorescence enhancement in this system reaches a maximum at distance about 5 nm away from a nanosphere surface and that distances closer than 5 nm will lead to fluorescence quenching due to non-radiative decay through energy transfer to the metal. However, the distances for maximum enhancement and quenching are very sensitive to details of the specific fluorophore-nanoparticle (NP) system, such as NP shape and size, the fluorophore quantum yield, and dipole orientation. FPs are made through cellular machinery and have emissive properties that are very sensitive to the environment, and the interactions of FPs with plasmonic particles have not been completely characterized. Thus, understanding the distance dependence of the specific FP-NR system being studied is of vital importance for optimizing fluorescence enhancement. The distance dependence of enhancement for FPs coupled to gold NRs is currently being studied on the single-molecule level by Bing Fu, a graduate student in the Biteen lab, in a project that is showing fantastic progress and very interesting results. Building on the initial

experiments described here in Chapter 2, Bing is using polyelectrolyte layers, as well as sputtered SiO_2, to control the separation between the FP and the NR in the axial direction.[2] Similar to our results in Chapter 2, Figure 2-6d, she has measured an approximately 2-fold enhancement in the brightness of the mCherry FP at a distance of 0 nm (no spacer layer), but interestingly, she observes a maximum enhancement of approximately 3.4× at a distance of about 6 nm (1 spacer layer). Importantly, Bing's work suggests that the enhancement observed in Chapter 2 is not an upper limit and that with optimization of the system, much higher enhancements could be observed.

The enhancement effect observed in Chapter 2 occurs in the near-field of the nanorod, but a molecule directly touching a metallic nanoparticle is expected to be quenched (no observable emission) due to nonradiative interactions. Therefore, another avenue that will be interesting to study *in vitro* is the shift of apparent emission position of coupled molecules. This shift has been shown experimentally and described theoretically in work led by Dr. Esther Wertz,[3] a postdoc in the Biteen lab, but in the future, it would be very interesting to characterize this shift experimentally using coupled dyes. In Chapter 2 Figure 2-8, we observed that the emission from FPs near an NR appeared to emanate from very near the NR center. This contradictory observation suggests that we cannot accurately localize the position of an emitting molecule when it is coupled to the nanorod based only on a simple model of finding the center of the emission pattern. Therefore, we hypothesize that linking red-emitting and blue-emitting dye molecules will allow us to determine the actual emitter position. We believe that the red molecule will couple to the NR longitudinal mode, and that the red emission will be observed at the NR position, while the blue molecule will not couple because the emission will be very far blue-shifted

from the NR transverse mode, and thus its emission will be observed at the actual emitter location. These experiments will allow us to correct for mis-localizations due to the shift in apparent emission position, as well as to determine the true distance dependence of enhancement without the need for spacer layers, and these developments are both important for applying this technique to bio-imaging experiments.

An important first step in such a project would be optimizing synthetic routes for coupling a red-emitting molecule to a blue-emitting molecule. Initially, we believed that Cy5.5 (the red-emitting molecule used in Chapter 4) could be coupled to Rhodamine123 (a blue-emitting molecule) by using a standard protocol for coupling NHS esters (Cy5.5) and amino groups (Rhodamine123) and then purifying the product using high-performance liquid chromatography.[4] However, after a few initial attempts to isolate a coupled product and further discussion of the planned synthesis with a trained organic chemist, we now believe that the amino group of Rhodamine123 is likely not reactive due to resonance in the structure, and therefore the planned synthesis will not result in a coupled product. Therefore, alternative synthesis protocols might be considered, like using peptides or DNA to link dyes together.[5] Some important considerations for determining the best model molecule and appropriate synthetic route are the distance between linked molecules, the flexibility of the linker, and the potential of Förster Resonance Energy Transfer (FRET) to occur between the dye molecules. The linker must be shorter than the measurement localization precision so that the location of the blue molecule reveals the true position of the red molecule; the linker must be rigid enough that the red-emitting molecule cannot bend toward the blue-emitting molecule and interact, such as in FRET; and removing the potential to undergo FRET will reduce any

additional energy transfer that could complicate the emission pattern. Once proper synthesis and purification protocols are established and a sufficient yield of coupled dye pairs is obtained, molecular adsorption (PAINT) experiments similar to those described in Chapter 2 but with coupled dye pairs rather than single-color emitters can determine the relationship between observed emission position and actual emitter position.

5.2.2 Enhancing the impact of plasmon-enhanced fluorescence for bio-imaging applications

In Chapter 3, we couple nanostructured gold substrates to *V. cholerae* cells to improve the emissivity of membrane-bound FPs. After exploring many different nanoparticle fabrication techniques, including evaporated gold nanoisland films, and drop-cast and surface-functionalization techniques for gold NR films, we settled on gold nanotriangles made using nanosphere lithography (NSL) with 750-nm-diameter polystyrene spheres. This substrate preparation technique resulted in the most uniform and reproducible nanoparticle films, and had a predictable background signal that could be completely subtracted. A next step in expanding this would be to explore a wider range of plasmonic substrates in such experiments. Khatua et al. observed that maximum dye emission enhancement is attained when the laser excitation wavelength and the nanoparticle plasmon resonance are slightly red-shifted from the emission wavelength of a dye.[6] Therefore, it might be interesting to tune the plasmon resonances of the substrates used for imaging FPs in *V. cholerae* cells to longer wavelengths than the FP emission. Studying a variety of substrates will reveal which parameters are important for optimizing enhancement for *in vivo* imaging and will therefore result in enhancements much higher than those measured in Chapter 3. These samples could be made using

electron beam lithography[3] to produce many substrates with different, carefully defined resonances, or this could be done using NSL with polystyrene beads of various sizes to make a series of NT substrates with diverse, but less defined and broader resonances.[7] Furthermore, NSL is very flexible and can be used to easily tune plasmonic substrates.[7-10] By slightly melting the nanospheres using a plasma etcher or even a hot plate, the mask through which gold is evaporated can be manipulated, changing the shape of the plasmonic particles left behind once the beads are removed and offering another avenue for tunability of substrate resonances. Ultimately, NSL might offer the easiest route for a systematic study of coupling between FPs and substrates.

Because plasmon-enhanced bio-imaging is still a new technique, it must be proven useful and reliable for widespread use among biologists. Studies that address the needs of the bio-imaging community, like increased imaging speeds and robust application for studying diffusion in biological systems, will make the technique more attractive for use in many lab settings. First, a systematic study of the increased imaging speeds and localization precisions and trajectory lengths attained by plasmon-enhanced emission would quantify the improvement in imaging capabilities due to coupling to plasmonic substrates. Next, a detailed study and description of how coupling—and the concommitent shifts in apparent emission position—does (or does not) affect the observed and calculated diffusion properties of the proteins being tracked would be an important advance to make the technique more appealing for biological studies since describing the known perturbations would enable them to be deconvolved from the data. In a strategy suggested by David Rowland, because Brownian motion is fractal, the nanoparticles on an imaging substrate could act as imaging pixels that accurately reflect

the system dynamics, despite a change in scale.[11] Additionally, three-dimensional single-molecule imaging based on a cylindrical lens in the emission pathway[12,13] is a technique that is currently being developed for widespread use in the Biteen lab and one which would offer an interesting view into the plasmon-coupled cellular environment. Combined with the strategies outlined above for understanding and deconvoluting mis-localizations, three-dimensional images could provide axial information about membrane-bound fluorescent labels and offer a more detailed molecule-by-molecule understanding of the local environment. Three-dimensional images would also allow us to address the issue of mis-localizations *in vivo*. Finally, the work in Chapter 3 describes the observed enhancement for inner membrane proteins in live cells and it would be very interesting to label an outer membrane protein and determine is similar, better, or worse enhancements could be observed.

5.2.3 Further increasing nanoscale selectivity based on polarization

Chapter 4 depicts experiments based on selectively enhancing the emission of dyes coupled to gold nanorods (NRs) based on linearly polarized *excitation*. As discussed at the end of Chapter 4, the next steps for this work are to develop and conduct experiments that study the polarization of the *emission* from a fluorophore-NR coupled system. Additionally, it would be very informative to put a red-emitting dye in solution above an immobilized 3:1 gold NR, and use 514-nm laser light to excited the transverse mode of the 3:1 NR. Here, the dye could not directly absorb the 514-nm excitation, and any emission from the red-emitting dye would suggest that the laser-excited transverse plasmon mode had transferred energy to the longitudinal plasmon mode, consequently exciting the latter mode and allowing enhanced emission to occur. Finally, because the

light detected in the far field from the coupled nanoparticle-dye systems can originate from many sources, spectrally resolving the emission from this coupled system would give further insight into the transverse-to-longitudinal plasmon mode energy transfer mechanism. Along with the polarization information, these spectra may allow us to discriminate light emitted directly from a dye molecule, light emitted from the NR, and light radiated from the coupled plasmon-mode of the NP-fluorophore system.

5.3 Conclusions and Outlook

Plasmon-enhanced emission is a well described and established phenomenon[14-23] that we have been exploring for a new application: single-molecule bio-imaging. It is our hope that the work in this thesis will serve as a foundation to build a field that expands the scope of plasmon-enhanced emission. We would like this technique to become readily available for biologists and biophysicists to use with single-molecule imaging and increase what can be learned from *in vivo* imaging. We have used nanostructured gold substrates to increase both the emission and the photostability of FP labels, and we believe that these results will be important for answering biophysical questions with greater confidence and precision. We further believe that, in the future, by developing the appropriate theory to coincide with this new application, plasmon-enhanced emission will find widespread acceptance and use within the bio-imaging community.

References

1. Anger, P.; Bharadwaj, P.; Novotny, L. Enhancement and Quenching of Single-Molecule Fluorescence. *Phys. Rev. Lett.* **2006**, *96*, 113002.

2. Fu, B.; Donehue, J.; Isaacoff, B.; Rowland, D.; Biteen, J. Distance-dependent Plasmonic Fluorescence Enhancement of Single Fluorophore on a Gold Nanorod. *In preparation* **2014**.

3. Wertz, E.; Isaacoff, B.; Donehue, J.; Biteen, J. Single-molecule fluorescence unravels the coupling of light to a plasmonic nano-antenna. *Submitted* **2014**.

4. Lumiprobe **NHS ester labeling of amino biomolecules**. *http://www.lumiprobe.com/protocols/nhs-ester-labeling* (accessed 09/19, 2014).

5. Maddler, S.; Bich, C.; Touboul, D.; Zenobi, R. Chemical cross-linking with NHS esters: a systematic study on amino acid reactivities. *J. Mass Spect.* **2009**, *44*, 694-706.

6. Khatua, S.; Paulo, P. M. R.; Yuan, H.; Gupta, A.; Zijlstra, P.; Orrit, M. Resonant Plasmonic Enhancement of Single-Molecule Fluorescence by Individual Gold Nanorods. *ACS Nano* **2014**, *8*, 4440-4449.

7. Fayyaz, S.; Tabatabaei, M.; Hou, R.; Lagugne-Labarthet, F. Surface-Enhanced Fluorescence: Mapping Individual Hot Spots in Silica-Protected 2D Gold Nanotriangle Arrays. *J. Phys. Chem. C* **2012**, *116*, 11665-11670.

8. Hulteen, J. C.; Van Duyne, R. P. Nanosphere lithography: A materials general fabrication process for periodic particle array surfaces. *J. Vac. Sci. Technol. A* **1995,** *13*, 1553-1558.

9. Chang, Y.; Wang, S.; Chung, H.; Tseng, C.; Chang, S. Large-Area Bowtie Nanoantenna Arrays Fabricated with Economic Oxygen Plasma-Assisted Nanosphere Lithography. *Plasmonics* **2011**, *6*, 599-604.

10. Haynes, C. L.; Van Duyne, R. P. Nanosphere Lithography: A Versatile Nanofabrication Tool for Studies of Size-Dependent Nanoparticle Optics. *J. Phys. Chem. B* **2001**, *105*, 5599-5611.

11. Zijlstra, P.; Chon, J. W. M.; Gu, M. Five-dimensional optical recording mediated by surface plasmons in gold nanorods. *Nature* **2009**, *459*, 410-413.

12. Biteen, J. S.; Goley, E. D.; Shapiro, L.; Moerner, W. E. Three-Dimensional Super-Resolution Imaging of the Midplane Protein FtsZ in Live *Caulobacter crescentus* Cells Using Astigmatism. *Chem. Phys. Chem.* **2012**, *13*, 1007-1012.

13. Huang, B.; Wang, W.; Bates, M.; Zhuang, X. Three-Dimensional Super-Resolution Imaging by Stochastic Optical Reconstruction Microscopy. *Science* **2008**, *319*, 810-813.

14. Aslan, K.; Gryczynski, I.; Malicka, J.; Matveeva, E.; Lakowicz, J. R.; Geddes, C. D. Metal-enhanced fluorescence: an emerging tool in biotechnology. *Curr. Opin. Biotechnol.* **2005**, *16*, 55-62.

15. Giannini, V.; Fernandez-Dominguez, A. I.; Heck, S. C.; Maier, S. A. Plasmonic Nanoantennas: Fundamentals and Their Use in Controlling the Radiative Properties of Nanoemitters. *Chem. Rev.* **2011**, *111*, 3888-3912.

16. Lakowicz, J. Radiative Decay Engineering: Biophysical and Biomedical Applications. *Anal. Biochem.* **2001**, *298*, 1-24.

17. Lakowicz, J. R.; Malicka, J.; Gryczynski, I.; Gryczynski, Z.; Geddes, C. D. Radiative decay engineering: the role of photonic mode density in biotechnology. *J. Phys. D* **2003**, *36*, R240-R249.

18. Lakowicz, J. R. Radiative decay engineering 5: metal-enhanced fluorescence and plasmon emission. *Anal. Biochem.* **2005**, *337*, 171-194.

19. Zhang, J.; Fu, Y.; Chowdhury, M. H.; Lakowicz, J. R. Metal-enhanced single-molecule fluorescence on silver particle monomer and dimer: Coupling effect between metal particles. *Nano Lett.* **2007**, *7*, 2101-2107.

20. Tam, F.; Goodrich, G. P.; Johnson, B. R.; Halas, N. J. Plasmonic Enhancement of Molecular Fluorescence. *Nano Lett.* **2007**, *7*, 496-501.

21. Fort, E.; Gresillon, S. Surface enhanced fluorescence. *J. Phys. D* **2007**, *41*, 013001.

22. Bardhan, R.; Grady, N. K.; Cole, J. R.; Joshi, A.; Halas, N. J. Fluorescence Enhancement by Au Nanostructures: Nanoshells and Nanorods. *ACS Nano* **2009**, *3*, 744-752.

23. Langguth, L.; Punj, D.; Wenger, J.; Koenderink, A. F. Plasmonic Band Structure Controls Single Molecule Fluorescence. *ACS Nano* **2013**.

Appendix

Probing Coherence in Synthetic Cyclic Light-Harvesting Pigments

The work presented in this appendix was published in the following paper:

J. E. Donehue, O. P. Varnavski, R. Cemborski, M. Iyoda, T. Goodson III, *"Probing Coherence in Synthetic Cyclic Light Harvesting Pigments,"* Journal of the American Chemical Society, *2011*, **133**, 4819-4828.

Abstract

A series of π-extended cyclic thiophene oligomers of 12, 18, 24, and 30 repeat units have been studied using methods of ultrafast time-resolved absorption, fluorescence up-conversion, and three-pulse photon echo. These measurements were conducted in order to examine the structure-function relationships that may affect the coherence between chromophores within the organic macrocycles. Our results indicate an initial delocalized state can be seen upon excitation of the cyclic thiophenes. Anisotropy measurements show this delocalized state decays on an ultrafast timescale and is followed by the presence of incoherent hopping. From the use of a phenomenological model, we conclude our ultrafast anisotropy decay measurements suggest the system does not reside in the Förster regime and coherence within the system must be considered. Three-pulse photon echo peak shift experiments reveal a clear dependence of initial peak shift with ring size, indicating a weaker coupling to the bath (and stronger intramolecular interactions) as the ring size is increased. Our results suggest that the initial delocalized state increases with ring size to distances (and number of chromophores) comparable to the natural light harvesting system.

Introduction

Recent discoveries have indicated that quantum coherence effects may play an important role in achieving remarkably high energy conversion efficiency in natural photosynthetic organisms.[1-6] By effectively linking the chromophores together, quantum coherence allows the molecules to exploit the energy of the sun with nearly 100% efficiency.[2,4,6,7] What remains unclear, however, is an understanding of how specific structural or environmental parameters can contribute to quantum coherence and how these parameters could be synthetically manipulated to increase efficiencies in future optical and electronic devices.

Many oligo- and polythiophene compounds have attracted recent interest for use in optical and electronic devices due to their reported fluorescence and conducting properties.[8-11] The properties of shorter oligomers are known to be greatly influenced by "end-effects".[10,12,13] Dendritic structures have also been studied to determine their potential for use in artificial light-harvesting systems.[14-17] These structures have the advantage of controlled synthesis that results in regular and well-defined architectures, and their photophysical processes are strongly affected by their geometrical confinement.[17-20] However, issues related to end effects and very high flexibility are known to limit the possibilities of these structures.[21] Cyclic molecular aggregates, however, are well known to play a crucial role in very efficient natural photosynthetic systems.[22,23] Previous studies have shown long conjugation associated with relatively rigid and ordered cyclic morphology in synthetic structures leads to strongly enhanced

nonlinear optical responses.[24-27] Recently developed thiophene-based macrocycles offer new materials that combine potentially endless π-conjugation paths with structurally well-defined oligomers.[28-31] The outstanding electrical properties of oligothiophene systems have already shown success in organic photovoltaic cells.[9,32] By combining these materials with a cyclic topology shown to be efficient in light-harvesting antenna[33], we are able to gain a novel perspective in the development of efficient light conversion devices that utilize quantum coherence.

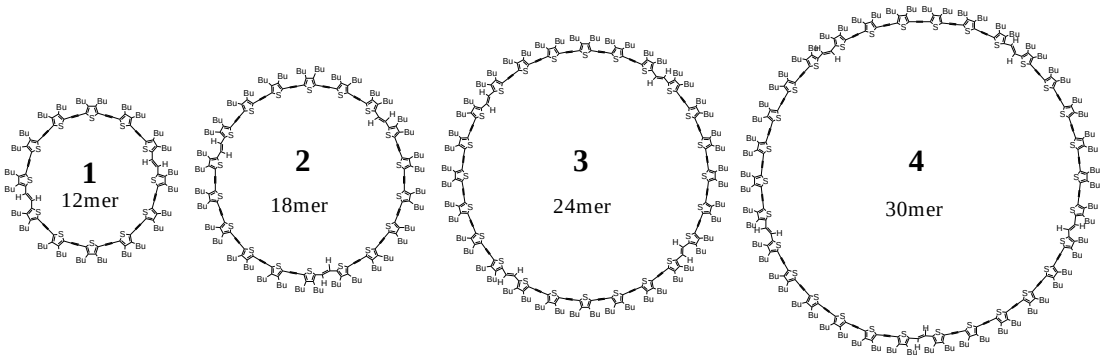

Figure 1. *Structures of giant thiophene macrocycles.*

In this contribution, we provide a systematic study of π-extended cyclic thiophene oligomers, which include 12, 18, 24, and 30 repeat units (Figure 1). These are π-conjugated systems with nanometer-sized cavities.[24,28,29] The ring diameters vary from ~21Å to ~60Å.[24,28,29] These materials experience no "end-effects" and are expected to be more rigid as compared to linear oligomers. To better understand the role of synthetic parameters, like ring size, in electronic coherences, we have preformed a detailed investigation of the structure of optical excitation in the artificial ring systems using ultrafast polarization- and time-resolved absorption, fluorescence, and three-pulse photon echo. The electronic delocalization length is an important measure of the balance

between the electronic intrachain coupling and the bath coupling (two fundamental interaction mechanisms which determine the efficiency of energy transfer in a light-harvesting system)[1-7,22,23,34-36] in a given oligomeric system[36,37], and therefore is a main focus in this work. Higher delocalization lengths indicate more sites are contributing to quantum coherence effects in the energy transfer process. States delocalized over a larger number of repeat units can possess larger transition moments, which facilitate greater absorption in a light-harvesting system and high energy transfer rates (hopping) between spectroscopic units. This can lead to a larger excitation migration distance, a parameter critical for efficient photovoltaics. With synthetic control of the ring size in the artificial structures, we will gain insight into the electronic delocalization length, as well as the role of planarity and the optimal number of building blocks in a ring, to maximize the optical response at lower cost. A more detailed understanding of these parameters is central to gaining deeper insight into quantum coherence-assisted energy transfer and how it can be incorporated into the design of artificial light-harvesting materials to direct energy flow with high efficiency.

Importantly, we have found the initial peak shift to increase as the size of the cyclic oligomer increases. As the initial peak shift reflects the inverse effective electronic transition-bath interaction[38-40], the peak shift rise indicates a decrease of the effective coupling of the electronic transition to the bath for larger rings. We assign this trend to the larger size of the electronic excitation coherent domain in larger rings. The delocalized excitation results in the eigenstate averaging over the fluctuations in local inhomogeneities of the sites[36,38-43] leading to the increased initial peak shift. Combined

with all ultrafast methods used in this study, these results indicate an initial delocalized state upon excitation of the cyclic oligomers.

Experimental Section

Synthesis and Structural Characterization: In this work, we have investigated π-extended cyclic thiophene oligomers of 12, 18, 24, and 30 repeat units (Figure 1, **1**-**4**). These materials were first synthesized by Iyoda and co-workers. [28,29] The synthesis of **1**-**4** was carried out by a McMurry coupling reaction with low-valent titanium.[24] All macrocycles presented possess key stability and oxidative characteristics[24] necessary for use in molecular electronics. They have fairly low oxidation potentials ($E^1_{1/2}$=0.31-0.33 V; $E^2_{1/2}$=0.50-0.52 V *vs* Fc/Fc^+).[24] All macrocycles are stable in crystalline form in air at room temperature. The X-ray structure has been measured for a single crystal of **1** obtained from chloroform-hexane solution.[24]

Steady State Measurements: Unless stated otherwise, all the experiments were performed in THF at ambient temperature. The absorption spectra of the molecules were recorded using an Agilent (Model # 8341) spectrophotometer. The emission spectra were acquired using a Shimadzu RF-1501 instrument. The quantum yields of the molecules were measured using a known procedure.[44] Coumarin 307 was used as the standard. The absorbance was limited to less than or equal to 0.03.

Transient Absorption Measurements: Time-resolved degenerate transient absorption studies have been carried out utilizing a cavity dumped Ti:sapphire laser system, which is spectrally centered at 830 nm with a repetition rate of 38 kHz and a pulse width of ~20 fs.[45,46] The fundamental beam was passed through a nonlinear BBO crystal generating

the second harmonic which was used as the excitation beam. This system possessed good noise characteristics, allowing the sensitivity for relative transient absorption in the 10^{-7} range at very low pump pulse energy <0.5 nJ/pulse. A probe beam of the same wavelength was passed through an optical delay line and a lens before being overlapped with the pump beam in the sample cell and detected by a photodiode. The modulated probe signal was measured with the use of a lock-in amplifier synchronized to an optical chopper in the pump beam path and was recorded as a function of delay line on a PC. Fitting the Gaussian peak of the instrument response function (IRF) gave a σ value of ~33fs (FWHM ~ 82 fs).[45,47] Polarization of the probe beam was controlled with a Berek compensator. For polarization measurements the setup was calibrated with the linear molecule β-Carotene.

Femtosecond Time-resolved Fluorescence Upconversion: Time-resolved polarized fluorescence of the thiophene macrocycles was studied using the femtosecond upconversion spectroscopy technique.[48] The upconversion system used in our experiments has been previously described.[26,45] Specifically, our upconversion system used frequency-doubled light from a mode-locked Ti-sapphire laser that produced pulses of 100 fs at a wavelength of 385-430 nm. Polarization of the excitation beam for the anisotropy measurements was controlled using a Berek compensator and the rotating sample cell was 1 mm thick. Horizontally polarized fluorescence emitted from the sample was up-converted in a nonlinear crystal of β-barium borate using a pump beam at about 800 nm which was first passed through a variable delay line. The instrument response function (IRF) was measured using Raman scattering from water. Fitting the Gaussian peak from the Raman scattering yields a σ value of a Gaussian IRF of ~106 fs,

giving a full width half maximum of ~243 fs. Spectral resolution was achieved by using a monochromator and photomultiplier tube. The excitation average power varied near 1 mW, corresponding to a pulse energy around a few tens of pJ per pulse.

Three-Pulse Photon Echo Measurements: Three-pulse photon echo experiments were carried out using a cavity-dumped Kerr lens mode-locked Ti-sapphire laser pumped by a frequency doubled YVO laser (Millennia, Spectra Physics).[45] The cavity-dumped laser pulse had a duration of ~20 fs. The pulse spectrum was centered at ~830nm. The cavity dumped beam was focused onto a 0.5mm BBO crystal to convert the fundamental beam into the second harmonic at ~415nm. Unless mentioned otherwise, the pulse repetition rate after cavity dumper was fixed at 38 kHz. In our setup, three beams of equal intensities (~0.5nJ per pulse in one beam at the sample) were generated with the aid of thin beam splitters (1mm-thick quartz substrate, CDP). One pulse (k_1) traveled a fixed delay, whereas the other two pulses (k_2 and k_3) traveled variable delays formed with retro-reflectors mounted on DC-motor driven delay stages (Newport ILS100CCHA) controlled via a Newport ESP7000 motion controller. The three beams were aligned after the delay stages to form an equilateral triangle beam geometry (8mm sides) and were focused into the 440μm-quartz sample cell using a thin singlet lens (f=18cm). The two third-order nonlinear signals in the k_1-k_2+k_3 and -k_1+k_2+k_3 phase matching directions were spatially filtered using irises and measured simultaneously onto two photomultipliers (Hamamatsu Photo Sensor Modules H6780). The electrical signals were measured by two lock-in amplifiers (Stanford Research, SR830) that were referenced to a chopper (SR540) inserted in the k_1-beam. Reproducibility of the signal was confirmed by repeated measurements, with special attention paid to the residual peak shift value at long

population periods T. The uncertainties of the peak shift value were estimated to be approximately ±0.5fs over the entire population period up to 100ps. The absorption spectra of the samples were checked before and after data collection, and lack of any observable changes suggests that little or no sample photodegradation or undesired chemical reactions occurred during the measurement. For our three-pulse photon echo peak shift (3PEPS) experiment, we simultaneously recorded two echo signals at the phase-matching conditions k_1-k_2+k_3 and -k_1+k_2+k_3. The time period τ between pulses 1 and 2 was scanned from negative τ to positive τ for a fixed population period T. The peak shift was defined at half the distance between the maximum intensity peaks of the two echo signals. The peak shift was recorded as a function of population period to give a peak shift decay. This measure is useful in that it closely follows the frequency fluctuation correlation function of the transition.[38-40]

Results and Discussion

Linear Spectroscopy: The normalized steady state absorption and emission spectra of the structures are shown in Figure 2. Steady state measurements were performed in dilute THF solutions (ca. 10^{-6}M). The position of the main peak in absorption shows a bathochromic shift with increasing size of the macrocycle. While the fluorescence spectra of the 12mer appears to have some small red shift with respect to the other ring systems, the fluorescence spectra of the 18mer, 24mer, and 30mer do not demonstrate any systematic shift. This small red shift in the 12mer fluorescence, as well as a blue shift in its absorption spectrum as compared to other rings, can be associated with the specific "ring flip" of the thiophenes adjacent to flexible double bonds. This is known to relieve strain in the 12mer.[24] The strain is less for larger spatial arrangements[28,49], which leads to

more regular structures.[24,28] This blue shift in the 12mer absorption could also be due to symmetry reasons and relatively large distances between excitonic states.[66] Clear vibronic structure can be observed in the fluorescence spectra (~1300cm^{-1}) and is similar to that reported for various sized linear oligo(thienylene-ethylene)s.[50,51] However, no vibronic structure is seen in the absorption spectra. This absence of mirror symmetry between absorption and emission spectra may indicate different absorption (Frank-Condon) and fluorescence (relaxed) configurations.[52,53] The similarity in fluorescence spectra for the rings of different sizes (18mer-30mer), as well as nearly the same fluorescence quantum yield (~10%) for all sizes, can be due to the localized character of the fluorescent (relaxed) state in these systems.

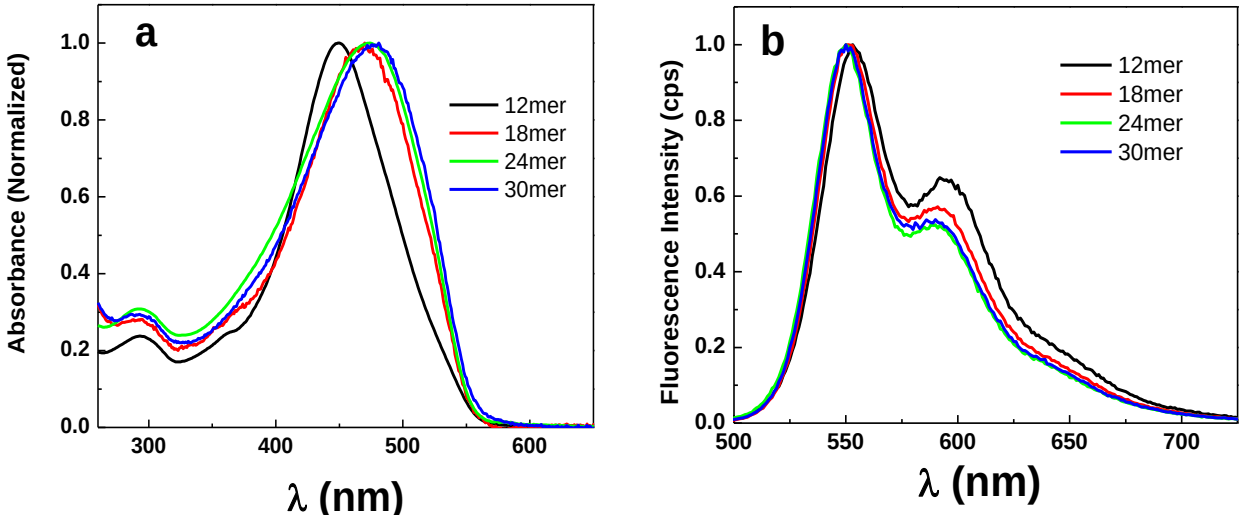

Figure 2. *Normalized absorption (a) and fluorescence (b) spectra of the macrocycles 12mer-30mer.*

Interestingly, the fluorescence peak for the macrocycles (560nm) is shifted to the red with respect to that for linear oligo(thienylene-ethynylene)s (512nm,[50] 513nm[28]). This red shift may indicate longer conjugation length in the rings as compared to the linear

building block.[50] It is also worth noting that the Stokes shifts for the 18mer (3285cm^{-1}), 24mer (3032cm^{-1}), and 30mer (2944cm^{-1}) are substantially smaller than those for the linear oligo(thienylene-ethynylene)s (3565cm^{-1} for 5αTE[50], 3617cm^{-1}for 9αTE39[50], and 3602cm^{-1} for oligo(2,5–thienylene-ethynylene) [28]). The corresponding smaller reorganization energies for the macrocycles, as compared to linear counterparts, could be an indication of less structural change for the macrocycles due to the absence of open ends and more rigid structure.

Ultra-fast Transient Absorption: We have investigated the polarized degenerate transient absorption dynamics at 415nm as a function of macrocycle size. In figure 3, multi-exponential anisotropy decays can be seen for both the 12mer and the 30mer. We have preformed a best fit of the data with multi-exponential decays after assuming the convolution of the IRF with the parallel and perpendicular absorption intensity profiles (see Supporting Information). The 12mer macrocycle was best modeled by a bi-exponential decay with an ultra-fast component and a long-lived residual component. The 18mer, 24mer, and 30mer macrocycles were best modeled by three exponential decays, which included an ultra-fast component, an additional picosecond component not seen in the 12mer decay, and a long-lived residual value.

The ultrafast decay component in each macrocycle was found to be in the range between 40 fs and 50fs. This ultrafast depolarization can be associated with strong interchromophore interaction and formation of a delocalized state (spectroscopic unit) over a substantial portion of the macrocycle.[17,25,34,45,46] The second decay component found in the larger (18mer, 24mer, and 30mer) macrocycles was near ~1ps. The appearance of an additional picosecond component in the anisotropy decay profile for the

larger rings indicates a hopping between spectroscopic units that are smaller than the full size of the ring.[23,45] In the case of the 12mer, the size of the spectroscopic unit is comparable to the size of the ring, thus making hopping not possible. This observation, as well as the ultrafast decay of the 12mer anisotropy to a residual value of ~0.1, supports the idea of a strong coupling regime with the excitation delocalized over the entire ring in the absorption configuration.[25,26]

The longest decay component was >100ps and contributed a near flat residual value on a short time scale (Figure 3). Considering the size of the macrocycles and the viscosity of THF (~0.46cP at 25°), this component can be associated with the rotational diffusion of the system. It is also important to note that the residual anisotropy before rotational diffusion occurs is 0.1 for both the 12mer and 30mer macrocycles (Figure 3). This is an indication of a planar arrangement of the transition moments in both molecules.[54] Though the 12mer displays a slightly bent chair-like structure in a single crystal[24], this can simply be the result of the packing force in the crystalline sample, which could not be present in solution. While in solution, however, the structure remains planar in terms of its transition dipoles' arrangement.

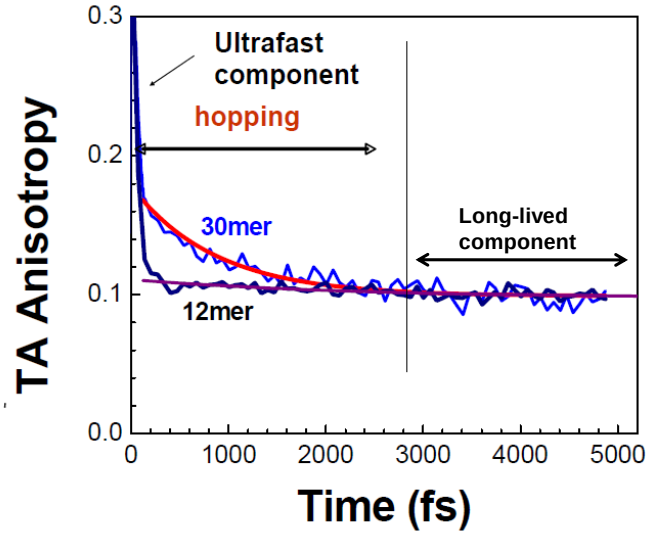

Figure 3. *Degenerate time-resolved transient absorption anisotropy for thiophene macrocycles 12mer and 30mer.*

In order to analyze the nature of optical excitations and the electronic coupling within the macrocycles, we utilized a simple phenomenological model developed by J. Leegwater for multichromophoric ring systems.[34] In this model, the discussion of the coherence of excitations is led by using an expression in which the limiting cases of Förster transfer (weak interaction) and completely delocalized excitonic states (strong interaction) are continuously connected to one another. The analysis uses the high temperature approximation for the extremely small phonon correlation time.[34] This model has been developed for the optical excitations in aggregates of chromophores where electron-hole pairs after excitation are localized on individual chromophores (Frenkel excitons). The thiophene macrocyclic systems investigated in this work have a substantial degree of conjugation that suggests strong electronic correlations over the oligomer. Though Leegwater's model is a simplified model for the thiophene macrocycles, it uses the exciton approach which is known to describe some basic features of the electronic structure of conjugated oligomers and polymers (such as energy

dependence) quite well.[55,56] For this reason, using Leegwater's model allows for a crude initial estimation of the intra-cycle coupling strength (transfer integral) and the excitation energy migration regime.[17] An interesting conclusion of this simple approach is that it is possible to relate the depolarization time to the ratio J/Γ of the interaction strength (J) and the homogeneous linewidth (Γ).[34] For the case of N- fold symmetry (planar) they are related by[34],

$$t_{dep} = \frac{1}{\Gamma(1-A)} \qquad (1)$$

$$\text{where} \quad A = \frac{1}{N}\sum_{k=1}^{N} \frac{\Gamma^2}{\Gamma^2 + 16J^2 \sin^2(2\pi/N)\sin^2(2\pi k/N)}$$

Here N is the number of chromophores contributing to the energy migration process. We have calculated the profile of Eq. 1 against realistic values of the homogeneous linewidth for the case of the 12mer (N=12) macrocycle. Shown in Figure 4 are the calculated curves for Eq. 1 vs. the interaction strength J. As we mention above, a depolarization time of approximately 40 fs was found. To estimate the interaction strength J and energy transfer regime, we need to know the homogeneous linewidth Γ. Using the full linewidth instead of the homogeneous linewidth would be an overestimation of Γ, so we tried several values to find the approximate value. A set of curves describing Eq. 1 for different values of homogeneous broadening Γ, taken to be similar to the full low-energy absorption peak linewidth, is shown in Figure 4. Several important inferences can be drawn from Figure 4 without exact knowledge of Γ. First, it is clearly seen that within the frame of this model it is impossible to have an anisotropy decay time of 40 fs and reside in the Förster regime (small interaction) for any homogeneous broadening smaller than

the full linewidth. This supports the idea that coherence must be taken into account. Extrapolation of the Γ=2000-3000 cm^{-1} curves to estimate the interaction strength results in a magnitude of J close to 1400 cm^{-1} (Fig. 4). This estimated intra-cycle electronic coupling strength is much higher than that for interchromophore coupling for the natural photosynthetic ring LH2 (~300cm^{-1})[35,57], which is not surprising taking into account π-conjugation in the 12mer.

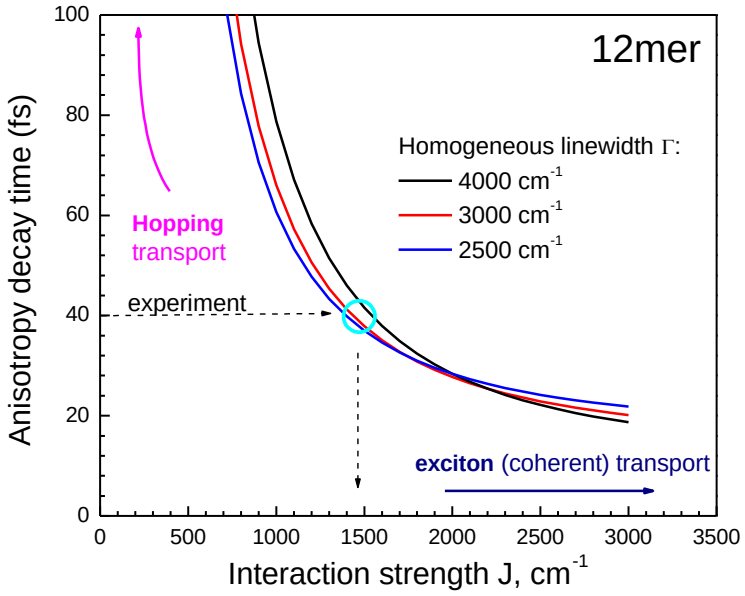

Figure 4. *Theoretical dependence[47] of the anisotropy decay time τ_r on the inter-chromophore interaction J for a macrocyclic 12-chromophore molecular system. The arrow shows the depolarization time obtained from experiment for the 12mer.*

Ultra-fast Time-resolved Fluorescence: An isotropic (magic angle) fluorescence decay profile for the 30mer at a detection wavelength of 570nm is shown in Figure 5. The bi-exponential decay fit shows a long decay component near 361±50ps. This is very close to the fluorescence decay times obtained for linear oligo(thienylene-ethynlene)s (300-330ps).[50] Similar to other oligo- and polythiophene systems, the fluorescence lifetime of the macrocycle is determined by the fluorescence quenching due to the intersystem crossing process.[11,26,50,58,59] Additionally, from our fluorescence decay measurements, the short decay component was found to be dependent on detection wavelength. For example, at 550nm, we saw an initial decay component of ~8ps, while at 570nm the initial component is closer to 14ps (not shown). This behavior is typically associated with the dynamic Stokes shift. This can be caused by excitation energy migration along the chain, torsional relaxtion[11,26,60-62], or solvation effects[63]. However, the transient absorption anisotropy measurement for the 12mer, as described above, indicates negligible energy migration along the thiophene ring chain on the picosecond time scale (Figure 3). Also, the hopping component for the 30mer has a time scale of ~1ps, which is substantially smaller than the short decay component of the fluorescence decay (Figure 3). It has also been shown that solvation effects are only a minor contributor to the dynamics of large conjugated oligomers and polymers.[52] For these reasons, we can conclude that the fast component in the isotropic decay (Figure 4) is most likely associated with a torsional relaxation in the excited state.[60-62] This process is caused by the difference in the torsional potential energy profile between the ground and excited states.[62,64]

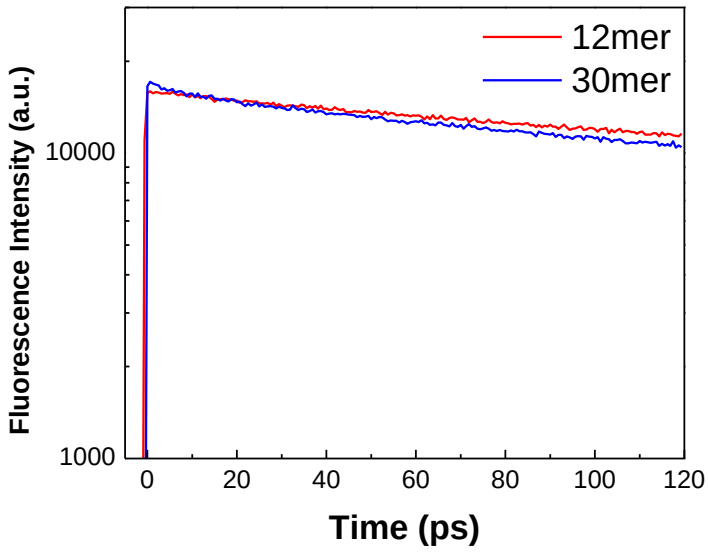

Figure 5. *Fluorescence decay profiles for 12mer and 30mer. Excitation wavelength is 400nm. Detection wavelengths are 570nm. Best fit to two-exponential decay function is shown by solid red line.*

Time-resolved fluorescence anisotropy measurements for the four macrocycles were also preformed. Figure 6 shows a comparison of the 12mer and 30mer anisotropy decay. Fast initial anisotropy decay within the instrument response profile, followed by a residual, relatively long lived anisotropy, can be seen. This is qualitatively similar to what is observed in the transient absorption signal (Figure 3). However, in the case of fluorescence, most of the initial anisotropy at time zero that is seen in the transient absorption profile is lost in the higher lying states before relaxation to the fluorescent state. The residual anisotropy value, prior to rotational diffusion, for fluorescence (~0.05) is lower than that for absorption (~0.1). This difference likely arises due to the final arrangement of transition dipoles, which can be different for a relaxed fluorescence state as compared to a Franck-Condon absorption configuration. The transient absorption

anisotropy measurement probes the excitation while it is delocalized across a large portion of the ring. In this delocalized configuration, the transition dipoles are arranged within the plane of the molecule, and the resulting long time anisotropy value is 0.1. In the time-resolved fluorescence anisotropy measurements, the lower value of 0.05 can be a signature of either an incline in the angle of the transition moment of the localized fluorescent state from the molecular plane[17,65] or a distortion of the molecule's shape in the relaxed fluorescent excited state from a planar configuration.

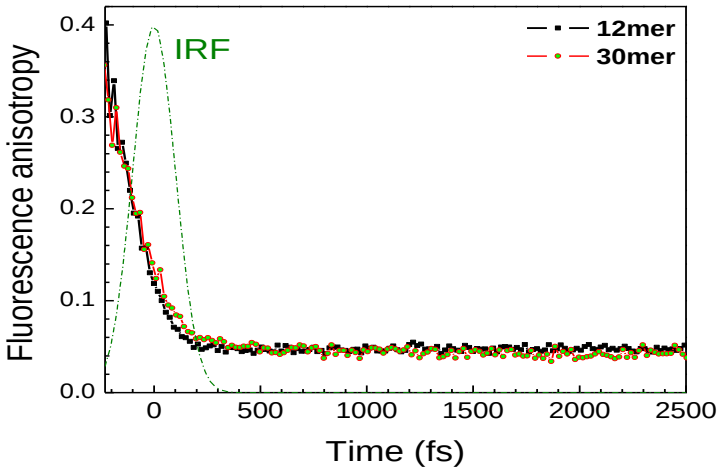

Figure 6. *Time-resolved fluorescence anisotropy for 12mer and 30mer. Instrument response function (IRF) is also shown by dash-dot line.*

When discussing the fluorescence of these materials, it is worth noting that the fluorescence decay time in linear oligomers is very close to that for the rings[50], while the fluorescence quantum yield for the rings was found to be almost three times smaller (~10% in the rings, while ~30% in the linear structures).[24,28,50] This suggests a smaller radiative decay rate for the rings as compared to their linear counterparts. In circular aggregates, the superradiance factor (the radiative rate enhancement factor with respect to

that for the monomer) behaves differently as a function of size and disorder than in linear oligomers due to specific cyclic geometry.[37,66] The lowest transition is forbidden by symmetry considerations in ideal cyclic aggregates.[37,66] This specifically leads to the reduction of the radiative decay rate in circular aggregates as compared to linear oligomers.[37]

As was mentioned above, the fast component of the isotropic decay is likely due to a torsional relaxation in the excited state that results from a difference in the torsional potential energy profile between the ground and excited states. For linear oligo- and polythiophenes, a thiophene rotational potential energy profile in the excited state is steep having its minimum at an interthiophene angle of 0°, while it is relatively shallow in the ground state with minima at ~30° and ~150° corresponding to *syn* (*s-cisoid*) and *anti*(*s-transoid*) configurations, respectively.[60-62] This leads to a planarization of the structure after optical excitation, which produces the dynamic Stokes shift.[60] This situation looks more complex in oligo(thienylene – ethynylene)s. Calculations and X-ray analysis showed that linear oligo(thienylene – ethynylene)s are near planar and mostly in *anti* configuration in the ground state.[50] In cyclic oligothiophene structures, geometrical and strain considerations predicted mostly *syn* configurations for smaller rings and *anti* configurations for larger (>14 thiophenes) rings.[49] In oligo(thienylene – ethynylene) cyclic systems containing 10 thiophenes, the X-ray analysis showed that all sulfur atoms in the thiophene rings were directed towards the cycle's center (*syn* – configuration).[28] For the 12mer, similar analysis revealed that two thiophene rings from the total 12 are in *s-transoid* form with the sulfur atom directed outside the macrocycle.[24] Both experiments indicated a near planar (not twisted) thiophene ring arrangement in the ground state for

the macrocycles. For the larger rings, the molecular structure has not been yet determined by X-ray analysis. All of the larger rings have HOMO-LUMO gaps (from the absorption maxima, Fig. 2) quite similar to each other, but smaller than that of the 12mer. This can indicate a different conformational (torsional) arrangement for the larger macrocycles (18mer, 24mer and 30mer) as compared to the 12mer. Calculations have shown that the difference in the HOMO-LUMO energy gap between *syn* and *anti* arrangements for large macrocyclic cyclo[n]thiophenes (n>20) is relatively small; however, in terms of total strain energy, the *anti* configuration is more stable.[49] For large macrocyclic cyclo[n]thiophenes, the planarization of the thiophene rings system in the LUMO state for the *anti* configuration, similar to that for linear oligothiophenes, has also been predicted.[49] Rotational barriers and energy difference between the *s-transoid* and *s-cisoid* conformers are relatively small[12,49] and a mixed *s-transoid* and *s-cisoid* structure can be suggested for larger macrocycles. Moreover, taking into account low rotation barriers, torsional relaxation between conformers can occur after the excitation and contribute to the dynamic Stokes shift.

Three-Pulse Photon Echo Peak Shift: A comparison of the normalized 3PEPS decays of the macrocycles of different sizes is shown in Figure 7. Results of the direct fit of these raw data sets, along with a sum of exponentials, were used as initial parameters in determining our model for the transition frequency correlation function *M(t)* given below. From Figure 7, it can be seen that the 3PEPS profile decays demonstrate clear ring size dependence.

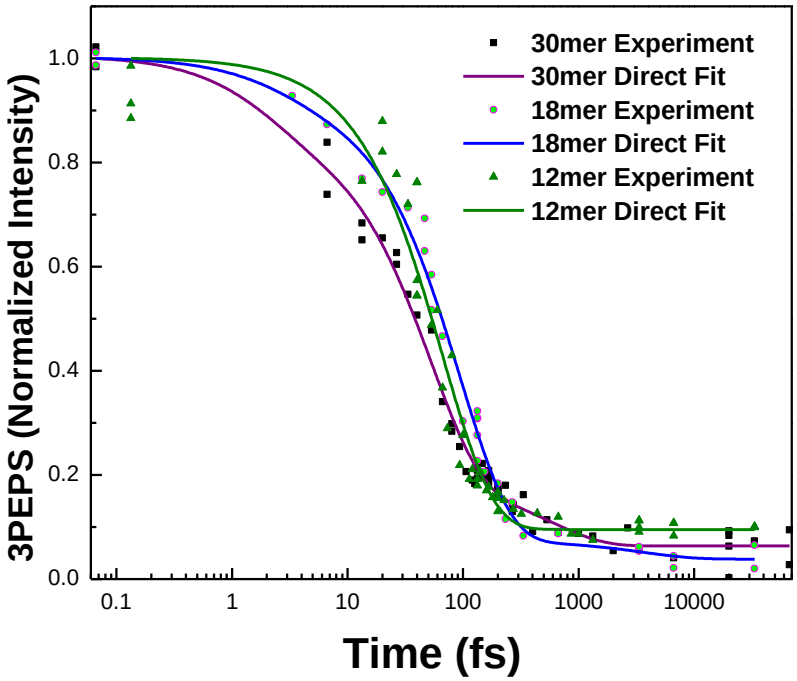

Figure 7. *Comparison of direct fits of 3PEPS decay for thiophene macrocycles.*

In order to better understand the dynamics of optical excitations, in regard to the nature of interaction between individual chromophores and between chromophores and solvent, we have preformed three-pulse photon echo peak shift (3PEPS) experiments[39,40] using an excitation wavelength of 415nm. It should be noted that using an excitation wavelength that lies on the blue side of the molecules maximum absorption will have an excess of excitation energy that can have effects on the peak shift.[67] Additional vibrational modes can be excited and increase the number of dynamic processes occurring, resulting in smaller initial peak shift and reduced time constants.[68] However, because the absorption maxima of our systems are all quite similar (excluding the 12mer), by exciting each system at 415nm, we are providing approximately the same

amount of excess energy for each system. Because our study is comparative in nature, we believe this excess of energy is not detrimental to our experiment or the context of our observed trends.

The 3PEPS method is capable of providing time scales and coupling strengths of dephasing processes that are coupled to electronic transitions by providing a line shape function and separating the static contribution to the line broadening.[39,40] A representative integrated three-pulse photon echo signal for the 30mer at T=0fs is shown in Figure 8. The 3PEPSs as functions of population period T for the 12mer and the 30mer are shown in Figure 9a and 9b, respectively (data points). Numerical modeling of the echo peak shift was also performed using a direct fit of the raw peak shift data as initial parameters. We started from a model for the transition frequency correlation function *M(t)* for a two level chromophore coupled to the environment and to its own fluctuating nuclei:

$$M(t) = \frac{<\delta\omega(0)\delta\omega(t)>}{<\delta\omega^2>}$$

where $\delta\omega(t)$ is the fluctuating part of the electronic transition frequency for each chromophore relative to its central frequency <ω>. Beyond the pulse overlap time interval, an initial guess of the energy gap correlation function *M(t)* can be obtained that closely follows the experimental 3PEPS-profile.[38-40] The quantity *M(t)* is important because it can be used for the description of the memory of the electronic transition frequency and system dynamics when the characteristic frequencies of the transition frequency fluctuations are small compared to kT.[43] This high-temperature approach can be applied to describe the coupling of the electronic transition to many intermolecular

(solvation) modes at room temperature. The main spectroscopic signals can be most conveniently derived from the complex line shape function *g(t)*:[43]

$$g(t) = P(t) + iQ(t) = <\Delta\omega^2> \int_0^t dt_1 \int_0^{t_1} dt_2 M(t_2) + i\lambda \int_0^t dt_1 M(t_1) \qquad (2)$$

In Eq. (2) *P(t)* and *Q(t)* are the real and imaginary parts of *g(t)*, $<\Delta\omega^2>$ is the coupling strength (fluctuation amplitude), and λ is the reorganization energy. The absorption spectrum of the system can be calculated by taking the real part of the Fourier transform of exp[-*g(t)*], while the third-order photon echo signal in the impulsive limit can be expressed by[38-40,45,46]:

$$S_{PE}(\tau, T) \propto \int_0^\infty dt \exp[-\sigma_{in}^2 (t-\tau)^2] \exp\{-2[P(\tau) - P(T) + P(t) + P(\tau + T) + P(T + t) - P(\tau + T + t)]\} \cos^2[Q(T) + Q(t) - Q(T + t)] \qquad (3)$$

where σ_{in} represents the width of the static inhomogeneous distribution.

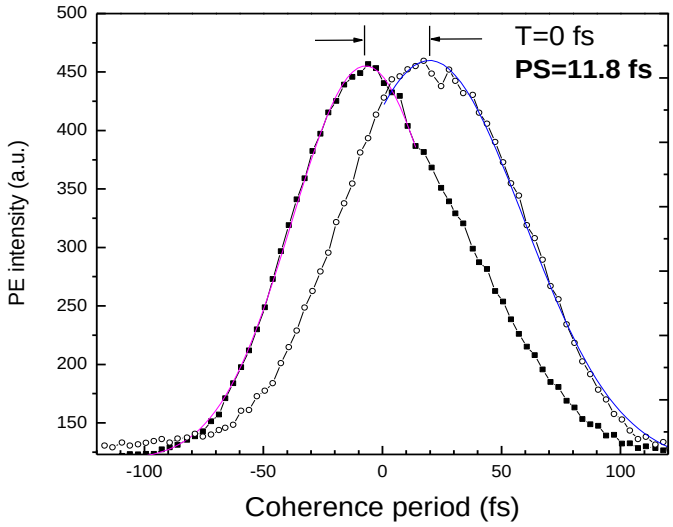

Figure 8. *Three-pulse photon echo signal for 30mer at zero population period T=0.*

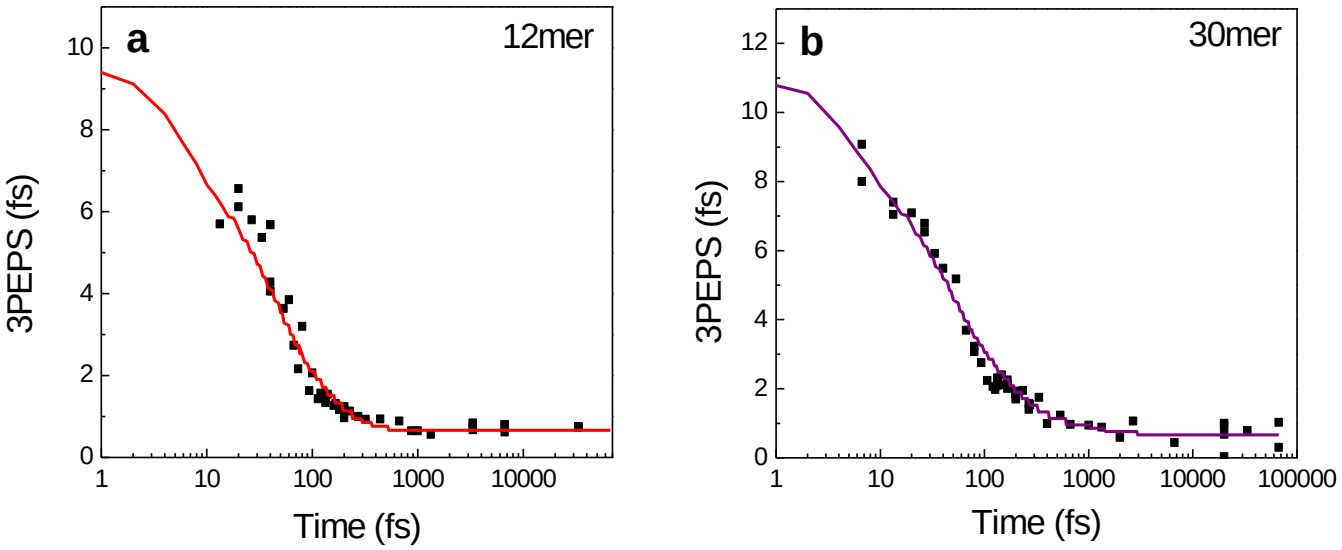

Figure 9. *Three-pulse photon echo peak shift profiles for 12mer and 30mer. Numerical modeling results are also shown (solid lines).*

Using the model described above, the peak shift values (position of the maximum, τ_p) were calculated from the photon echo signal $S_{PE}(\tau,T)$ for the 12mer and 30mer as a function of population period T and are shown in Figure 9 (solid lines). Most of the modeling was performed using the impulsive limit, but the effect of the finite pulse width was considered and estimated by convoluting the pulse electric field envelope (which was taken to be of Gaussian shape with σ=35fs) with the proper time ordered[38-40] response functions (for positive τ, the rephasing response functions contribute, while for negative τ, the nonrephasing response functions contribute) at several population periods (T-points). These response functions were then used to determine the third-order polarization, which was used to calculate the time-integrated photon echo signal with a finite pulse width.[39] These convoluted values where then compared to the 3PEPS values

obtained in the impulsive limit and the ratio $3PEPS_{conv}/3PEPS_{impuls}$ was found. This ratio was determined to be weakly dependent on the population period T and we corrected the impulsive limit results by this factor.[38,45,46,68] Using too many parameters in the model correlation function can result in different contributions cancelling one another out. To minimize such issues, we have attempted to limit the various contributions to *M(t)* to three exponentials and one constant (static disorder):

$$M(t) = \frac{\left[\sum_{i=1}^{3}\left\langle \Delta\omega_{ei}^{2}\right\rangle \exp\left(-\frac{t}{\tau_{ei}}\right) + \sigma_{inh}^{2}\right]}{\left[\sum_{i=1}^{3}\left\langle \Delta\omega_{ei}^{2}\right\rangle + \sigma_{inh}^{2}\right]} \qquad (4)$$

In some cases, a Brownian oscillator was added to the model. In effect, the Brownian oscillator contribution qualitatively represents a sum of several intramolecular vibrational modes that are not exactly known for these macrocycles.[69] From Figure 9, it is clear there is good agreement between the experimental data points and the modeled fit. The time constants and coupling strengths of the model *M(t)* are shown in the Table 1 below:

Table 1

Macrocycle	$\Delta\omega_1$, cm^{-1}	τ_1, *fs*	$\Delta\omega_2$, cm^{-1}	τ_2, *fs*	$\Delta\omega_3$, cm^{-1}	τ_3, *fs*	σ_{inh}, cm^{-1}
12mer	503	4	476	130	0	-	291
30mer	450	4.8	370	140	212	800	238

Once a set of parameters was obtained that reproduced a satisfactory peak shift, the absorption spectrum was calculated for the 30mer and compared with the experimental spectrum. It can be seen in Figure 10 that the calculated absorption spectrum is noticeably narrower than the full experimental absorption spectrum. In order to better understand the structure of the experimental absorption spectrum, we performed a simple decomposition of the spectra using three Gaussian components. By comparing the absorption spectrum calculated from the correlation function obtained from the 3PEPS experiments, we see some similarity in the calculated spectrum and the first Gaussian component, though a vibronic progression is not clearly seen.

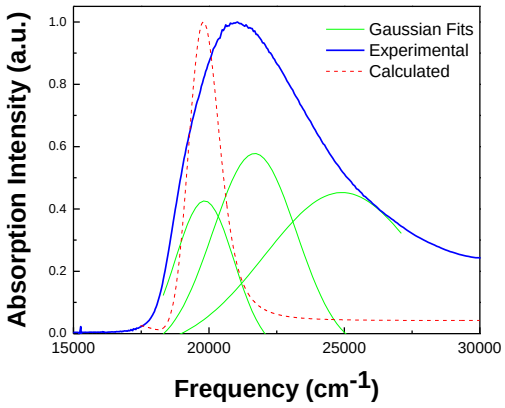

Figure 10. *Comparison of experimental and calculated absorption spectrum for the 30mer.*

Previous work[39,40] has shown that residual 3PEPS at very large population periods results from static inhomogeneous broadening. From Figure 9, it can be seen the residual 3PEPS is very small for all investigated macrocycles. This indicates minor inhomogeneous broadening (conformational diversity) for all studied systems.[38,39] It is also known that the initial peak shift reflects the inverse effective electronic transition-bath interaction.[38-40] Our results clearly show an increase in initial peak shift as ring size is increased (Figure 11). This rise in peak shift indicates a decrease of the effective electron-bath coupling for larger rings. This is a counterintuitive trend as complexity of the system is rising with increased ring size, leading one to expect increased disorder and increased coupling pathways to the bath. We propose this weaker coupling is the result of exchange narrowing effects which are caused by the eigenstate averaging over the fluctuations and local inhomogeneities of the sites by delocalized excitation.[36,41-43] Exchange narrowing occurs and the fluctuations of the system average out such that interaction with the bath decreases with an increase in ring size.[36,45,46] Also, the 3PEPS decays very quickly as a function of population period. The decay profile shows only minor contribution from the sub-picosecond and picosecond components. From this, it is clear that most of the dephasing in these large macrocycles can be associated with intramolecular processes rather than solvation, similar to what was reported for polymers[52], dendrimers[45], and J-aggregates[69].

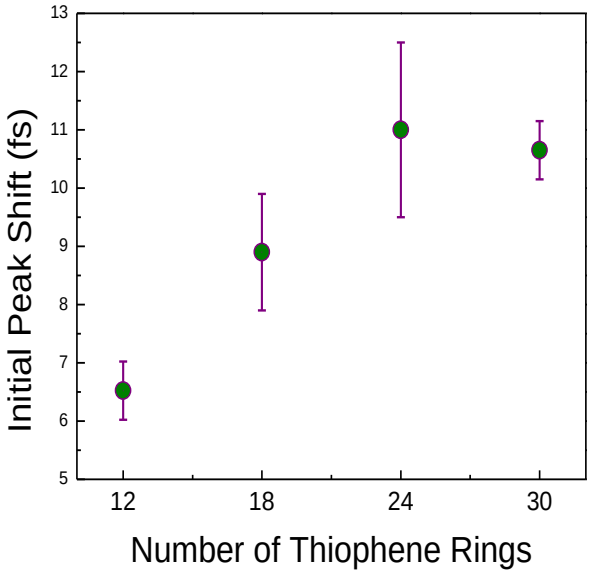

Figure 11. *Three-pulse photon echo initial peak shift as a function of the ring size.*

After considering what has been learned from the transient absorption and fluorescence upconversion experiments, we can use our 3PEPS experimental results and numerical modeling to gain a detailed perspective of the excited state dynamics occurring in the thiophene macrocycles. Three distinct time constants were seen in the numerical modeling of the 3PEPS signal. Though these time constants do not align exactly with those provided by our transient absorption and fluorescence upconversion experiments, we believe the first two exponential time components of our numerical model may be revealing some combination of high-frequency vibrational modes and self-trapping of excitation along the macrocycle. Previous results have shown self-trapping to occur in <45fs[52,70,71]. In our numerical model, we cannot clearly distinguish between the two processes, but it is likely the faster time constant is representative of a self-trapping

process. The 3PEPS numerical modeling also indicated the presence of a picosecond component in the correlation function for the larger macrocycles (18mer, 24mer, and 30mer), which is absent for the smaller 12mer macrocycle. This correlates well with the ultrafast fluorescence anisotropy data. These findings support the suggestion of an initially delocalized excitation over a major fraction of the ring, followed by incoherent hopping taking place on a picosecond time scale.

Comparison to natural light-harvesting system: When considering their potential for application in the future, it is beneficial to compare these systems with natural light-harvesting antenna, like LH2 of purple photosynthetic bacteria. In comparison to the natural system, our synthetic system has dramatically increased interaction strength between chromophores. As a result, our synthetic system demonstrates enhancement of several optical properties over the natural system. The excitation transfer time of our synthetic system is 40fs, as compared to 700fs[72] in the natural system. The TPA cross section of our synthetic system is two orders of magnitude higher than that of the natural system.[24,73] The excitation delocalization length for our synthetic system is 18 units, which is dramatically larger than that of the natural system.[37] Though these materials are still quite far from mimicking the high efficiency of a natural system, their optical properties, as seen in Table 2, clearly demonstrate they are a material of interest for future work:

Table 2	***Light-Harvesting Pigments***	
	LH2 of purple photosynthetic bacteria	***Synthetic 30mer***
Transfer Time*	700fs[72]	40fs
Initial Peak Shift	24fs[72]	12fs
Interaction Strength	320 cm^{-1} (intra), 255 cm^{-1} (inter)[35]	1500 cm^{-1}
TPA Cross Section	1,116 GM (calculated)[73]	107,800 GM[24]
Linewidth	~450 cm-1[72]	~2000 cm^{-1}
Excited State Lifetime	1ns[74]	~300ps
Delocalization Length	5-13 units[37]	18 units

**From depolarization measurements*

Conclusion

In this work, we have presented a detailed study of the excited state structure and dynamics in a series of large oligo(thienylene-ethynylene) macrocycles. We have brought toether a variety of recent synthetic and spectroscopic techniques, combined with theoretical modeling, to closely describe the delocalized excitations in a series of macrocyclic thiophene systems. The three-pulse photon echo peak shift experiments showed a clear dependence of the initial peak shift on ring size. The rise of the peak shift with the ring size suggests the tendency to decrease effective electron-bath coupling for larger delocalization lengths in large macrocycles. From depolarization experiments, we see a planar arrangement of the transition dipoles (in the absorption configuration) even in large rings. We also show from photon echo experiments that there is low inhomogeneous broadening for all systems. Combined, these results indicate relatively ordered structures. Collectively, our experimental results indicate a delocalized state can

be seen upon excitation of the cyclic thiophene rings, which we estimate has a length of about 18 (theienylene-ethynylene) units for the thiophene system. This conclusion is in accord with a strong cooperative enhancement of two-photon absorption cross-section in the 18mer reported previously.[24] Also, by comparing the optical properties of our synthetic pigment to a natural light-harvesting system, we have demonstrated the utility of these materials for future applications. It is our hope the results offered here will lend themselves to the future development of the next generation of solar conversion devices.

References:

1. Collini, E.; Wong, C. Y.; Wilk, K. E.; Curmi, P. M. G.; Brumer, P.; Scholes, G. D. *Nature* **2010**, *463*, 644.

2. Engel, G. S.; Calhoun, T. R.; Read, E. L.; Ahn, T. K.; Mancal, T.; Cheng, Y. C.; Blankenship, R. E.; Fleming, G. R. *Nature* **2007**, *446*, 782.

3. van Grondelle, R.; Novoderezhkin, V. I. *Nature* **2010**, *463*, 614.

4. Lee, H.; Cheng, Y. C.; Fleming, G. R. *Science* **2007**, *316*, 1462.

5. Cheng, Y. C.; Silbey, R. J. *Phys. Rev. Lett.* **2006**, *96*, 028103.

6. Ishizaki, A.; Fleming, G. R. *Proc. Natl. Acad. Sci.* **2009**, *106*, 17255.

7. Scholes, G. D. *J. Phys. Chem. Lett.* **2010**, *1*, 2.

8. Lightowler, S.; Hird, M. *Chem. Mater.* **2005**, *17*, 5538.

9. Mishra, A.; Ma, C. Q.; Bauerle, P. *Chem. Rev.* **2009**, *109*, 1141.

10. Ma, W. L.; Yang, C. Y.; Gong, X.; Lee, K.; Heeger, A. J. *Adv. Funct. Mater.* **2005**, *15*, 1617.

11. Ramakrishna, G.; Bhaskar, A.; Bauerle, P.; Goodson, T. *J. Phys. Chem. A* **2008**, *112*, 2018.

12. Mena-Osteritz, E. *Adv. Mater.* **2002**, *14*, 609.

13. Cho, S.; Seo, J. H.; Park, S. H.; Beaupre, S.; Leclerc, M.; Heeger, A. J. *Adv. Mater.* **2010**, *22*, 1253.

14. BarHaim, A.; Klafter, J.; Kopelman, R. *J. Am. Chem. Soc.* **1997**, *119*, 6197.

15. Devadoss, C.; Bharathi, P.; Moore, J. S. *J. Am. Chem. Soc.* **1996**, *118*, 9635.

16. Hagedorn, K. V.; Varnavski, O.; Hartwig, J.; Goodson, T. *J. Phys. Chem. C* **2008**, *112*, 2235.

17. Varnavski, O. P.; Ostrowski, J. C.; Sukhomlinova, L.; Twieg, R. J.; Bazan, G. C.; Goodson, T. *J. Am. Chem. Soc.* **2002**, *124*, 1736.

18. Poliakov, E. Y.; Chernyak, V.; Tretiak, S.; Mukamel, S. *J. Chem. Phys.* **1999**, *110*, 8161.

19. Minami, T.; Tretiak, S.; Chernyak, V.; Mukamel, S. *J. Lumin.* **2000**, *87-89*, 115.

20. Kirkwood, J. C.; Scheurer, C.; Chernyak, V.; Mukamel, S. *J. Chem. Phys.* **2001**, *114*, 2419.

21. Bosman, A. W.; Janssen, H. M.; Meijer, E. W. *Chem. Rev.* **1999**, *99*, 1665.

22. Sundstrom, V.; Pullerits, T.; van Grondelle, R. *J. Phys. Chem. B* **1999**, *103*, 2327.

23. Bradforth, S. E.; Jimenez, R.; Vanmourik, F.; Vangrondelle, R.; Fleming, G. R. *J. Phys. Chem.***1995**, *99*, 16179.

24. Williams-Harry, M.; Bhaskar, A.; Rarnakrishna, G.; Goodson, T.; Imamura, M.; Mawatari, A.; Nakao, K.; Enozawa, H.; Nishinaga, T.; Iyoda, M. *J. Am. Chem. Soc.* **2008**, *130*, 3252.

25. Varnavski, O.; Bauerle, P.; Goodson, T. *Opt. Lett.* **2007**, *32*, 3083.

26. Bhaskar, A.; Ramakrishna, G.; Hagedorn, K.; Varnavski, O.; Mena-Osteritz, E.; Bauerle, P.; Goodson, T. *J. Phys. Chem. B* **2007**, *111*, 946.

27. Raymond, J. E.; Bhaskar, A.; Goodson, T.; Makiuchi, N.; Ogawa, K.; Kobuke, Y. *J. Am. Chem. Soc.* **2008**, *130*, 17212.

28. Nakao, K.; Nishimura, M.; Tamachi, T.; Kuwatani, Y.; Miyasaka, H.; Nishinaga, T.; Iyoda, M. *J. Am. Chem. Soc.* **2006**, *128*, 16740.

29. Iyoda, M. *Heteroat. Chem*, **2007**, *18*, 460.

30. Zhang, F.; Gotz, G.; Winkler, H. D. F.; Schalley, C. A.; Bauerle, P. *Angew. Chem. Int. Ed.* **2009**, *48*, 6632.

31. Kromer, J.; Rios-Carreras, I.; Fuhrmann, G.; Musch, C.; Wunderlin, M.; Debaerdemaeker, T.; Mena-Osteritz, E.; Bauerle, P. *Angew. Chem. Int. Ed.* **2000**, *39*, 3481.

32. Wynands, D.; Mannig, B.; Riede, M.; Leo, K.; Brier, E.; Reinold, E.; Bauerle, P. *J. Appl. Phys.* **2009**, *106*.

33. Van Patten, P. G.; Shreve, A. P.; Lindsey, J. S.; Donohoe, R. J. *J. Phys. Chem. B* **1998**, *102*, 4209.

34. Leegwater, J. A. *J. Phys. Chem.***1996**, *100*, 14403.

35. Scholes, G. D.; Fleming, G. R. *J. Phys. Chem. B* **2000**, *104*, 1854.

36. Beljonne, D.; Curutchet, C.; Scholes, G. D.; Silbey, R. J. *J. Phys. Chem. B* **2009**, *113*, 6583.

37. Dahlbom, M.; Pullerits, T.; Mukamel, S.; Sandstrom, V *J. Phys. Chem.B* **2001**, *105*, 5515.

38. Cho, M. H.; Yu, J. Y.; Joo, T. H.; Nagasawa, Y.; Passino, S. A.; Fleming, G. R. *J. Phys. Chem.* **1996**, *100*, 11944.

39. Joo, T. H.; Jia, Y. W.; Yu, J. Y.; Lang, M. J.; Fleming, G. R. *J. Chem. Phys.* **1996**, *104*, 6089.

40. deBoeij, W. P.; Pshenichnikov, M. S.; Wiersma, D. A. *J. Phys. Chem.* **1996**, *100*, 11806.

41. Kubo, R. *Adv. Chem. Phys.* **1969**, *15*, 101.

42. Knapp, E. W. *Chem. Phys.* **1984**, *85*, 73.

43. Ohta, K.; Yang, M.; Fleming, G. R. *J. Chem. Phys.* **2001**, *115*, 7609.

44. Demas, J. N.; Crosby, G. A. *J. Phys. Chem.***1971**, *75*, 991.

45. Varnavski, O.; Yan, X. Z.; Mongin, O.; Blanchard-Desce, M.; Goodson, T. *J. Phys. Chem. C* **2007**, *111*, 149.

46. Varnavski, O.; Goodson, T.; Sukhomlinova, L.; Twieg, R. *J. Phys. Chem. B* **2004**, *108*, 10484.

47. Varnavski, O.; Goodson, T.; Bauerle, P. *Linear and Nonlinear Optics of Organic Materials Vii* **2007**, *6653*, 65317.

48. Shah, J. *Ieee J. Quant. Elec.* **1988**, *24*, 276.

49. Zade, S. S.; Bendikov, M. *J. Org. Chem.* **2006**, *71*, 2972.

50. Fujitsuka, M.; Makinoshima, T.; Ito, O.; Obara, Y.; Aso, Y.; Otsubo, T. *J. Phys. Chem. B* **2003**, *107*, 739.

51. Li, J.; Liao, L.; Pang, Y. *Tetrahedron Lett.* **2002**, *43*, 391.

52. Yang, X. J.; Dykstra, T. E.; Scholes, G. D. *Phys. Rev. B* **2005**, *71*.

53. Heimel, G.; Daghofer, M.; Gierschner, J.; List, E. J. W.; Grimsdale, A. C.; Mullen, K.; Beljonne, D.; Bredas, J. L.; Zojer, E. *J. Chem. Phys.* **2005**, *122*.

54. Hall, R. D.; Valeur, B.; Weber, G. *Chem. Phys. Lett.* **1985**, *116*, 202.

55. Chang, R.; Hsu, J. H.; Fann, W. S.; Liang, K. K.; Chiang, C. H.; Hayashi, M.; Yu, J.; Lin, S. H.; Chang, E. C.; Chuang, K. R.; Chen, S. A. *Chem. Phys. Lett.* **2000**, *317*, 142.

56. Beenken, W. J. D.; Pullerits, T. *J. Phys. Chem. B* **2004**, *108*, 6164.

57. Tretiak, S.; Middleton, C.; Chernyak, V.; Mukamel, S. *J. Phys. Chem. B* **2000**, *104*, 4519.

58. Becker, R. S.; deMelo, J. S.; Macanita, A. L.; Elisei, F. *J. Phys. Chem.* **1996**, *100*, 18683.

59. Magnani, L.; Rumbles, G.; Samuel, I. D. W.; Murray, K.; Moratti, S. C.; Holmes, A. B.; Friend, R. H. *Synth. Met.* **1997**, *84*, 899.

60. Westenhoff, S.; Beenken, W. J. D.; Friend, R. H.; Greenham, N. C.; Yartsev, A.; Sundstrom, V. *Phys. Rev. Lett.* **2006**, *97*, 166804.

61. Lanzani, G.; Nisoli, M.; DeSilvestri, S.; Tubino, R. *Chem. Phys. Lett.* **1996**, *251*, 339.

62. Grozema, F. C.; van Duijnen, P. T.; Berlin, Y. A.; Ratner, M. A.; Siebbeles, L. D. A. *J. Phys. Chem. B* **2002**, *106*, 7791.

63. Horng, M. L.; Gardecki, J. A.; Papazyan, A.; Maroncelli, M. *J. Phys. Chem.* **1995**, *99*, 17311.

64. Beenken, W. J. D.; Lischka, H. *J. Chem. Phys.* **2005**, *123*, 9.

65. Demidov, A. A.; Andrews, D. L. *Photochem. Photobiol.* **1996**, *63*, 39.

66. Bednarz, M.; Reineker, P.; Mena-Osteritz, E.; Bauerle, P. *J. Lumin.* **2004**, *110*, 225.

67. Larsen, D. S.; Ohta, K.; Xu, Q.-H.; Cyrier, M.; Fleming, G. R. *J. Chem. Phys.* **2001**, *114*, 8008.

68. Nagasawa, Y.; Passino, S. A.; Joo, T.; Fleming, G. R. *J. Chem. Phys.* **1997**, *106*, 4840.

69. Mukamel, S. *Principles of Nonlinear Optical Spectroscopy*; Oxford University Press, Inc.: New York, 1995.

70. Grage, M. M. L.; Zaushitsyn, Y.; Yartsev, A.; Chachisvilis, M.; Sundstrom, V.; Pullerits, T. *Phys. Rev. B* **2003**, *67*, 205207.

71. Sperling, J.; Nemeth, A.; Baum, P.; Sanda, F.; Riedle, E.; Kauffmann, H. F.; Mukamel, S.; Milota, F. *Chem. Phys.* **2008**, *349*, 244.

72. Jimenez, R.; vanMourik, F.; Yu, J. Y.; Fleming, G. R. *J. Phys. Chem. B* **1997**, *101*, 7350.

73. Abe, S. *Chem. Phys.* **2001**, *264*, 355.

74. Freiberg, A.; Jackson, J. A.; Lin, S.; Woodbury, N. W. *J. Phys. Chem. A* **1998**, *102*, 4372.